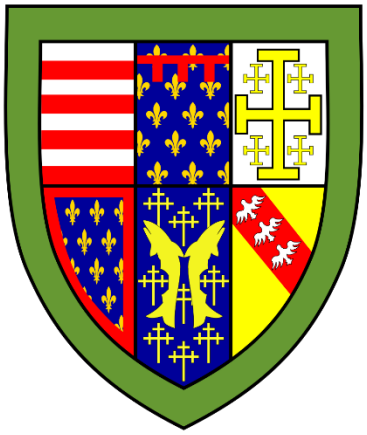
Modelling brain tumours with network neurosciences and deep learning





Yiran Wei

Department of Clinical Neurosciences,

University of Cambridge

Queens' College

Jan 2023

This thesis is submitted for the degree of Doctor of Philosophy

Supervisors:

Professor Stephen J Price

Dr Chao Li

Examiners:

Professor Li Su

Professor Yalin Zheng

Modelling brain tumours with network neurosciences and deep learning

Yiran Wei

Glioma is one of the most common and lethal brain tumours. The clinical diagnosis and prognosis of glioma are challenging due to its heterogeneous nature. In the past, glioma was considered a focal disease with local disruption to the brain. However, recent studies suggested that tumour cells would migrate into normal-appearing brain regions through white matter tracts, implying the widespread impact of gliomas.

Meanwhile, quantitative MRI technology, including functional MRI and diffusion MRI, assisted in developing an emerging field called network neurosciences. The network neurosciences model the brain as a network consisting of macro-scale regional connectivity of the brain instead of the micro-scale networks of neurons. The novel brain network approach has the potential to characterise the global impact of brain tumours. This thesis aims to invoke specialised network neuroscience approaches for characterising brain tumours and systematically analyse the global tumour disruption across the brain.

First, I provided extensive reviews of brain tumours and network neurosciences. Then I discussed the limitations and current research gaps in the cross-disciplinary field of brain networks of brain tumours. The main finding implied that although there was potential for studying brain networks in brain tumours, the tumour disruption could hinder the robust application of the traditional methodology on brain tumour patients.

In Chapter 2, I developed a novel approach for constructing structural brain networks with diffusion MRI. This approach tackled the challenge of constructing brain networks using traditional tractography and brain atlas. For evaluating the proposed method, functional networks were generated as the evaluation baseline of the method. Results showed that brain networks generated from the proposed method had a stronger correlation with the functional networks compared to traditional methods, suggesting the robustness of the new approach.

In Chapter 3, I extensively analysed the disruption of brain networks in glioblastoma patients based on the methodology of Chapter 2. To address the heterogeneous disruption of glioblastomas, I classified the regions of brain networks into different categories according to

their locations. In particular, the disruption in distantly connected regions was significantly associated with patient performance, cognition, and prognosis, which validated the clinical value of brain networks for glioblastomas and implied the early signs of tumour invasion into the normal-appearing brain.

In Chapter 4, to investigate the potential of early tumour invasion outside the tumour regions and tackle the unavailability of diffusion MRI, I developed a graph-based deep-learning model for estimating brain networks from anatomical MRI (e.g. T1, T2). Notably, the model was informed by the prior anatomical knowledge of white matter connectivity. The model successfully predicted IDH mutation status with higher performance than convolutional neural networks, which suggested the feasibility of estimating brain networks in retrospective datasets with only anatomical MRI.

In Chapter 5, I combined the prior knowledge of brain network disruption and the clinical significance of tumour geometrics to develop a multi-modal deep learning framework that learnt from brain networks, tumour image, and tumour geometrics simultaneously. The model was built on the hypothesis that multi-modal data respectively represented different views of the aggressiveness of the same tumour. Results showed that this model outperformed other state-of-the-art models in predicting the IDH genotype of glioma. Additionally, visual interpretation suggested the interrelation among multi-modal data.

In conclusion, this thesis presented feasible tools and experiments for applying network neurosciences for brain tumour patients, which revealed the potential of the quantified characterisation of tumour impact across the whole brain.

PERSONAL DECLARATION

This thesis is the result of my own work and includes nothing which is the outcome of work done in collaboration except as declared in the preface and specified in the text.

It is not substantially the same as any that I have submitted, or, is being concurrently submitted for a degree, diploma or other qualification at the University of Cambridge or any other University or similar institution except as declared in the Preface and specified in the text. I further state that no substantial part of my dissertation has already been submitted, or, is being concurrently submitted for any such degree, diploma or other qualification at the University of Cambridge or any other University of similar institution except as declared in the Preface and specified in the text.

It does not exceed the prescribed word limit of 60,000 for the Degree Committee of Clinical Medicine and Clinical Veterinary Medicine.

Chapters 2 through 5 describe research done in the collaboration that either has or will soon undergo peer review. Co-authors of those publications mainly contribute to the data collection and data pre-processing. Because of these contributions, work described in Chapters 2-5 are described using plural pronouns (e.g. “we”) while singular pronouns (e.g. “I”) are used in the Chapter 1 and Chapter 6. Please note that the above contributions do not affect the status of the thesis as being chiefly my work.

ETHICS:

Studies in this thesis were approved by the local institutional review board of Cambridge University Hospital. For MRI data collection, informed written consent was obtained from all patients.

ACKNOWLEDGMENTS

First, I am grateful for the financial support from my family (my parents, grandparents, uncles, and cousins), who have unconditionally supported me in my abroad study (both undergraduate and PhD) for the past eight years.

Additionally, I would like to thank my supervisors Prof. Stephen Price and Dr. Chao Li for offering me the opportunity to study in Cambridge. I appreciate the support and guidance I received from them during the PhD study.

I wish to especially thank my friend and partner, Wenqi Li, for the support over the past four years, especially during the hardest period during the Covid-19 pandemic.

Finally, I acknowledge the funding source for data collection in Chapter 2 and 3: the NIHR Brain Injury MedTech Co-operative.

Journals publications:

1. Wei, Y., Li, C., Cui, Z., Mayrand, R. C., Zou, J., Wong, A. L., ... & Price, S. J. (2022). Structural connectome quantifies tumour invasion and predicts survival in glioblastoma patients. In *Brain*, awac360, https://doi.org/10.1093/brain/awac360
2. Wei, Y., Chen, X., Zhu, L., Zhang, L., Schönlieb, C. B., Price, S., & Li, C. (2023). Multi-modal learning for predicting the genotype of glioma. *IEEE Transactions on Medical Imaging.*

Conference publications:

3. Wei, Y., Li, C., & Price, S. J. (2021, September). Quantifying structural connectivity in brain tumor patients. In *International Conference on Medical Image Computing and Computer-Assisted Intervention* (pp. 519-529). Springer, Cham.
4. Li, C*., Wei, Y*., Chen, X., & Schönlieb, C. B. (2021). BrainNetGAN: Data augmentation of brain connectivity using generative adversarial network for dementia classification. In Deep Generative Models, and Data Augmentation, Labelling, and Imperfections: First Workshop, DGM4MICCAI 2021, and First Workshop, DALI 2021, Held in Conjunction with MICCAI 2021, Strasbourg, France, October 1, 2021, Proceedings 1 (pp. 103-111). Springer International Publishing.
5. Wei, Y., Li, Y., Chen, X., Schönlieb, C. B., Li, C., & Price, S. J. (2022). Predicting isocitrate dehydrogenase mutation status in glioma using structural brain networks and graph neural networks. In *International MICCAI Brainlesion Workshop* (pp. 140-150). Springer, Cham.
6. Wei, Y., Li, C., Chen, X., Schöinlieb, C. B., & Price, S. J. (2022, March). Collaborative learning of images and geometrics for predicting isocitrate dehydrogenase status of glioma. In 2022 IEEE 19th International Symposium on Biomedical Imaging (ISBI) (pp. 1-4). IEEE.
7. Wei, Y., Price, S. J., Schönlieb, C. B., & Li, C. (2023, April). Predicting conversion of mild cognitive impairment to Alzheimer's diseases by modelling healthy ageing trajectories. In 2023 IEEE 20th International Symposium on Biomedical Imaging (ISBI). IEEE.

ABBREVIATIONS:

AAL: Automatic Anatomical Labelling

ACC: Accuracy

ADNI: Alzheimer's Disease Neuroimaging Initiative

ANTs: Advanced Normalization Tools

AUC: Area Under the Curve

BOLD: Blood Oxygen Level Dependent

CCRT: Concurrent ChemoRadioTherapy

CE: Contrast-Enhancing

CNN: Convolutional Neural Networks

dMRI: Diffusion-weighted MRI

DTI: Diffusion Tensor Imaging

DWI: Diffusion Weighted Imaging

EOR: Extent Of Resection

FA: Fractional Anisotropy

FACT: Fibre Assignment by Continuous Tracking

FLAIR: Fluid-Attenuated Inversion Recovery imaging

fMRI: Functional Magnetic Resonance Imaging

FSL: FMRIB Software Library

GNN: Graph Neural Network

HCP: Human Connectome Projects

HR: Hazard Ratio

IDH: Isocitrate DeHydrogenase

KPS: Karnofsky Performance Status

MD: Mean Diffusivity

MGMT: O6-Methylguanine-methyltransferase

MLP: Multi-layer perceptron

MMSE: Mini-Mental State Examination

MRI: Magnetic Resonance Imaging

NE: Non-Enhancing

OS: Overall Survival

PFS: Progression-free survival

rfMRI: resting-state functional MRI

ROC: Receiver Operating Characteristic

SEN: Sensitivity

SPE: Specificity

SVM: Support Vector Machine

T1C: T1 post-contrast

TBSS: Tract-Based Spatial Statistics

TMZ: Temozolomide

UKF: Unscented Kalman Filter

VASARI: Visually Accessible Rembrandt Images

WHO: World Health Organisation

WM: White Matter

Content

Modelling brain tumours with network neurosciences and deep learning 1
Chapter 1. Introduction 1
1.1 Brain tumour 1
1.2 Magnetic resonance imaging 5
1.3 Network neurosciences 16
1.4 Hypothesis and outlines of the thesis 24
Chapter 2. Quantifying structural connectivity in brain tumour patients 27
2.1 Abstract 27
2.2 Introduction 28
2.3 Methods 30
2.4 Results 37
2.5 Discussion 43
2.6 Conclusion 44
Chapter 3. Structural connectome quantifies tumour invasion and predicts survival in glioblastoma patients 45
3.1 Abstract 45
3.2 Introduction 47
3.3 Methods 48
3.4 Results 58
3.5 Discussion 83
3.6 Conclusion 85
Chapter 4. Predicting isocitrate dehydrogenase mutation status in glioma using structural brain networks and graph neural networks. 86
4.1 Abstract 86
4.2 Introduction 87
4.3 Methods 89
4.4 Results 95
4.5 Discussion 97
4.6 Conclusion 98
Chapter 5 Multi-modal learning for predicting the genotype of glioma 100
5.1 Abstract 100
5.2 Introduction 100
5.3 Methods 106
5.4 Results 125
5.5 Discussion 129
5.6 Conclusion 132
Chapter 6. General Discussion 133
6.1 Summary of main findings 133
6.2 Methodological Limitations 138
6.3 Future research directions 140
References 146

Chapter 1. Introduction

1.1 Brain tumour

1.1.1 Background

A brain tumour is a mass of abnormal cells growing in the brain. Brain tumours include benign (noncancerous) or malignant (cancerous) types (Louis et al., 2007; Louis et al., 2021). Among brain tumours, glioma is the most lethal and the second most common primary brain tumour after Meningiomas in adults (Louis et al., 2021). Common symptoms of glioma patients include headaches, seizures, and neurological deficits in visual, motor, language and cognitive functions, which may indicate the location with tumour-related functional disruptions (Lapointe et al., 2018).

Glioma is a type of brain tumour that arises from glial cells. Traditionally, gliomas can be classified according to the type of originating glial cell and the degree of tumour malignancy. Specifically, astrocytomas arise from astrocytes, star-shaped glial cells that provide support and protection for the brain's neurons. Oligodendrogliomas arise from oligodendrocytes, which produce the myelin sheath surrounding and protecting nerve fibres in the brain and spinal cord. Ependymomas arise from ependymal cells, which line the ventricles (cavities) and the spinal cord's central canal (Louis et al., 2021). Gliomas are graded based on the degree of malignancy, from grade 1 being the least aggressive to grade 4 being the most aggressive. Particularly, Grade 1 gliomas are slow-growing, non-invasive tumours with a low likelihood of turning malignant. They often have well-defined borders and can be surgically removed with a good prognosis. Grade 2 gliomas are still considered low-grade tumours, but they grow more rapidly and are more likely to invade surrounding tissue. Grade 3 gliomas are anaplastic or malignant gliomas that exhibit rapid growth and invasion into neighbouring tissues. Grade 4 gliomas are the most aggressive and malignant form of gliomas which grow very rapidly, extensively infiltrating surrounding brain tissue (Louis et al., 2021).

Glioblastoma is one of the most aggressive tumours in grade 4 (Louis et al., 2021). The

first-line treatments for glioblastoma include maximum safe resection, followed by the combination of temozolomide (TMZ), an alkylating cytostatic chemotherapy drug, and radiotherapy. Even after maximum treatments, most glioblastoma patients do not survive beyond a year, and about 5% survive beyond five years (Lapointe et al., 2018). Glioblastoma is characterised by high inter-tumoral and intra-tumoral heterogeneity. Heterogeneity includes variations in both tumour cells and histological observations, including necrosis, haemorrhage and micro-vascularisation (Louis et al., 2016). Inter-tumoral heterogeneity represents the tumour heterogeneity among patients, while intra-tumoral heterogeneity is the regional heterogeneity within an individual tumour (Xiong et al., 2020). The heterogeneity poses significant challenges to the accurate stratification and prognosis of glioblastoma patients.

1.1.2 Molecular biomarkers

The World Health Organisation (WHO) Classification of Tumours of the Central Nervous System is a system for classifying brain and spinal cord tumours. The most recent versions of the WHO classification were published in 2007, 2016 and 2021(Louis et al., 2007; Louis et al., 2016; Louis et al., 2021). Before 2016, the diagnosis of glioma was primarily determined by the histological features and microscopic morphology of the tumour tissue (Louis et al., 2007). Since 2016, molecular biomarkers have been introduced into the classification system for diagnosing gliomas.

Isocitrate dehydrogenase (IDH) gene mutations status is one of the first biomarkers introduced into the WHO classification system since 2016 (Louis et al., 2016) **(Table. 1.1)**. IDH is the enzyme that converts isocitrate to alpha-ketoglutarate (α-KG) while IDH mutations are genetic mutations occurring in the IDH1 or IDH2 genes. IDH mutations are found to be significant in the prognosis of glioblastoma (Louis et al., 2016). Specifically, glioma patients with IDH mutation generally have significantly better survival time than patients without IDH mutation (Khan et al., 2017; SongTao et al., 2012). There are several factors of IDH mutation contributing to better survival. First, IDH mutations lead to the production of the oncometabolite, 2-hydroxyglutarate (2-HG) instead of the typical product,

α-KG, which alters cellular metabolism and reduces the aggressiveness of the tumour (Dang et al., 2009). Second, The accumulation of 2-HG results in a hypermethylated state, creating a distinct molecular subtype of glioma that is generally less aggressive than IDH-wildtype gliomas (Turcan et al., 2012). Lastly, IDH-mutant gliomas exhibit decreased angiogenesis and invasion, slowing tumour growth and contributing to better patient survival (Kohanbash et al., 2017).

The prevalence of IDH mutations in gliomas varies depending on the grade and type of the gliomas. Studies discovered that lower-grade gliomas (Grade 2 and 3) have a higher prevalence of IDH mutations, with approximately 70-80% of these tumours having IDH mutations. Less than 5% of primary glioblastomas (Grade 4) have IDH1 mutations, whereas more than 85% of secondary glioblastoma patients have been identified to have IDH1 mutations (Huang, 2019). Based on those discoveries, the 2016 WHO classification classified glioblastoma into three subtypes: IDH-wildtype, IDH-mutant, and NOS (not otherwise specified). The diagnosis of NOS is reserved for circumstances where complete IDH evaluation cannot be performed. The most used approaches to determine IDH mutation status in clinical practice include immunohistochemistry and gene sequencing. These tests involve analysing a sample of tumour tissue (obtained through a biopsy or surgery) to detect the presence of the IDH mutation (Louis et al., 2016).

WHO grade	2007 WHO	2016 WHO
II	Diffuse astrocytoma	Diffuse astrocytoma, IDH-mutant
	Oligoastrocytoma	Oligodendroglioma, IDH-mutant and 1p/19q codeleted
	Oligodendroglioma	
III	Anaplastic astrocytoma	Anaplastic astrocytoma, IDH-mutant
	Anaplastic oligoastrocytoma	
	Anaplastic oligodendrogliomas	Anaplastic oligodendroglioma,IDH-mutant and1p/19q codeleted
IV	Glioblastoma	Glioblastoma,IDH-wildtype
		Glioblastoma,IDH-mutant

Table 1.1. Comparison table for the 2007 and 2016 WHO classification of gliomas. Reprinted from (Miller et al., 2019).

Histology	WHO 2016	Grade	WHO 2021	Grade
Oligodendroglioma	Oligodendroglioma, IDH-mutantand 1p/19q-codeleted	WHO grade II	Oligodendroglioma, IDH-mutant and1p/19q-codeleted	CNS WHO grade 2
Anaplastic oligodendroglioma	Anaplastic oligodendroglioma, IDH-mutant and 1p/19q-codeleted	WHO grade III	Oligodendroglioma, IDH-mutant and1p/19q-codeleted	CNS WHO grade 3
Diffuse astrocytoma	Diffuse astrocytoma, IDH-wildtype or IDH-mutant	WHO grade Il	Astrocytoma,IDH-mutant	CNS WHO grade 2
Anaplastic astrocytoma	Anaplastic astrocytoma, IDH-wildtype or IDH-mutant	WHO grade III	Astrocytoma, IDH-mutant	CNS WHO grade 3
Glioblastoma	Glioblastoma, IDH-wildtype or IDH-mutant	WHO grade IV	Glioblastoma, IDH-wildtype	CNS WHO grade 4
Astrocytoma			Astrocytoma, IDH-mutant and CDKN2A/B homozygous deletion	CNS WHO grade 4
Astrocytoma			Glioblastoma, IDH-wildtype & TERTpromoter mutation, EGFR amplificationor gain/loss of chromosome 7/10	CNS WHO grade 4

Table. 1.2. Comparison table between the 2016 and 2021 WHO classifications of gliomas. Reprinted from (Huang, 2022).

1p/19q codeletion is another molecular biomarker introduced by the WHO classification in 2016. Specifically, 1p/19q codeletion is defined as the genetic events representing the complete deletion of the short arm of chromosome 1 and the long arm of chromosome 19. Patients with 1p/19q codeletion have significantly better overall survival than patients without 1p/19q codeletion (Boots-Sprenger et al., 2013).

In 2021, the WHO classification was updated with arising clinical evidence that molecular markers have more important roles in diagnosis and prognosis, introducing more biomarkers (e.g., CDKN2A/B homozygous deletion, TERT promoter mutation, EGFR amplification) **(Table. 1.2)** (Louis et al., 2021). More subtypes are classified based on the biomarkers, indicating better characterisation of the heterogeneous gliomas. In summary, these recommendations reflect the increasing importance of molecular testing in diagnosing and managing brain tumours. It is worth mentioning that although the category of glioblastoma IDH-mutant of WHO 2016 dropped out in WHO 2021, this thesis still followed the definition in WHO 2016 and included the glioblastoma IDH-mutant because the Covid-19 pandemics impeded the immediate deployment of the new standard in nationwide hospitals.

1.2 Magnetic resonance imaging

Magnetic Resonance Imaging (MRI) is a medical imaging technique that combines a magnetic field, radiofrequency pulses, and a computer to produce detailed images of the internal structure and function of the body.

The principle of MRI is based on the interaction between the magnetic field and the hydrogen protons in the body's water molecules (Lauterbur, 1973). When a patient lies inside the MRI machine, the magnetic field causes the hydrogen protons to align with the field. A radiofrequency pulse is then applied, which flips the protons out of alignment. Once the pulse is turned off, the protons begin to relax back to their original position, releasing energy in the form of radiowaves. These radio waves are detected by the MRI scanner and processed by a computer to create detailed images of the body's tissues and organs (Mansfield & Maudsley, 1977).

MRI is crucial for diagnosing and managing brain tumours (Lapointe et al., 2018). One

of the advantages of MRI is its non-invasiveness (free of radiation) or minimal invasiveness (with contrasting-agent), which enables the acquisitions during the disease development so that clinicians can monitor the progression of tumours for better management. Additionally, MRI has better tissue contrast compared to other medical imaging techniques such as CT and Ultrasound. Consequently, MRI is commonly used in surgical planning to estimate the extent of resection to remove as much tumour as possible without damaging normal brain tissue or causing functional deficits. After the surgery, MRI is usually referred to for planning radiotherapy and monitoring treatment response.

In clinical research, MRI is also applied for predicting molecular biomarkers in brain tumour patients. The clinical detection of biomarkers usually requires obtaining tissue samples from the surgical resection or biopsy, which could be inaccessible for some patients. To tackle this limitation, some studies tested the feasibility of predicting molecular biomarkers using features extracted from non-invasive MRI. This approach, also known as imaging genetics, correlates imaging features and gene expression in cancers, which could help better characterise the patient and improve prognosis (Ahmad et al., 2019; Kim et al., 2019).

1.2.1 Anatomical MRI

The routinely collected MRI sequences for brain tumour diagnosis are anatomical sequences, including T1 weighted, T1 contrast-enhancing (T1C or T1Gd), T2-weighted, and T2 fluid-attenuated inversion recovery (FLAIR) imaging (Menze et al., 2014):

T1 refers to the longitudinal relaxation time, which is the time it takes for the protons to realign with the magnetic field. In T1-weighted images, tissues with a short T1 relaxation time appear bright, while those with a long T1 relaxation time appear dark. T1-weighted images are particularly useful for visualizing anatomical structures and detecting fat-containing lesions (Hashemi et al., 2012). T1-weighted images are less sensitive to the presence of a tumour than other sequences but can still help detect fat-containing tumours or those with hemorrhagic components. Generally, brain tumours appear hypointense (darker) compared to the surrounding normal brain tissue on T1-weighted images (Osborn et al.,

2015).

Gadolinium is a contrast agent that shortens the T1 relaxation time of tissues it interacts with, making them appear brighter on T1-weighted images (Essig, 2005). For example, T1C could enhance the visualization of brain tumours by making them appear brighter on T1-weighted images. Particularly, gadolinium increases the signal of areas with disrupted blood-brain barrier and increased vascularity, which are often seen in brain tumours. This sequence is crucial for identifying tumour margins, determining the extent of tumour infiltration, and differentiating between the tumour and surrounding oedema (Lapointe et al., 2018).

T2 refers to the transverse relaxation time, which is the time it takes for the protons to lose phase coherence. In T2-weighted images, tissues with a long T2 relaxation time appear bright, while those with a short T2 relaxation time appear dark (Lawn et al., 2003). T2-weighted images are more sensitive in detecting brain tumours than T1-weighted images. Brain tumours generally appear hyperintense (brighter) compared to the surrounding brain tissue on T2-weighted images due to their increased water content. This sequence is also useful for visualizing peritumoral oedema, which appears as a hyperintense region around the tumour (Castillo, 2006).

FLAIR is a special type of T2-weighted imaging that suppresses the signal from free water, such as cerebrospinal fluid (CSF). FLAIR is particularly useful in detecting brain tumours located near fluid-filled spaces, such as the ventricles. FLAIR suppresses the cerebrospinal fluid (CSF) signal, making the tumour and peritumoral oedema more visible (Okuda et al., 1999). FLAIR can reveal infiltrative tumour margins that might be missed on T1- and T2-weighted images.

In summary, the combination of T1, T2, T1GD, and FLAIR MRI sequences provides complementary anatomical information about brain tumours, including their location, size, margins, vascularity, and the presence of peritumoral oedema. This information is crucial for accurate diagnosis, treatment planning, and monitoring of brain tumours.

The different presentations of gliomas on the above imaging modalities suggest heterogeneity. To address the heterogeneity of different MRI sequences in brain tumours, The multimodal brain tumour image segmentation (BraTS) benchmark (Menze et al., 2014) defined four separate brain tumour regions: contrast-enhancing tumour crore, non-enhancing

tumour, necrosis, and oedema **(Fig. 1.3)**. Additionally, the corresponding Multimodal Brain Tumor Segmentation (BRATS) Challenge boosts the development of deep learning for automatic brain tumour segmentation.

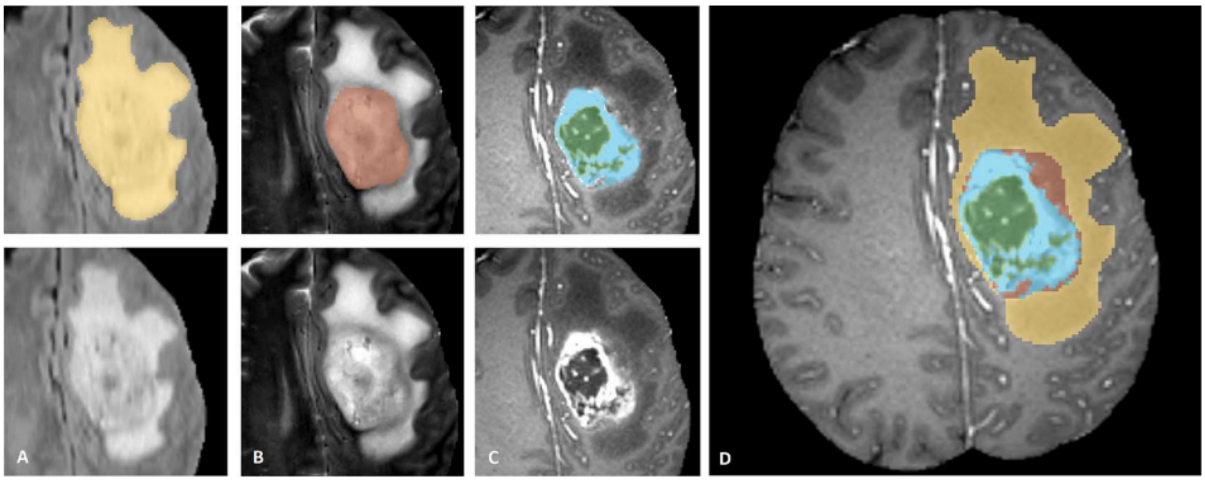


Fig. 1.1. Brain tumour segmentation benchmark (A), a visible large lesion including both the tumour core and oedema in T2 (B), the enhancing tumour structures visible in T1c (blue), surrounding the cystic/necrotic components of the core (green) (C). Segmentations are combined to generate the final labels of the tumour structures (D): oedema (yellow), non-enhancing solid core (red), necrotic/cystic core (green), and enhancing core (blue). Image reprinted from (Menze et al., 2014).

1.2.2 Functional MRI

Functional MRI (fMRI) uses Blood Oxygen Level Dependent (BOLD) contrast (Fleisher et al., 2009). Blood transports oxygen to brain cells. When the brain cells are active, the flow and oxygen levels of the blood increase. The fMRI monitors the change in hemodynamic (e.g. increase or decrease of blood flow) response to estimate brain activities related to oxygen consumption in specific brain regions. Separate brain areas activated simultaneously in fMRI during specific tasks (task-based fMRI) are considered functionally connected and associated with those tasks.

Although specific functional networks initially had to be identified with corresponding task-based fMRI, in recent decades, a task-negative fMRI protocol called resting-state functional MRI (rfMRI) became popular (**Fig. 1.1**) (Greicius et al., 2003). The research

discovered that under the resting state, the major functional networks could still be identified (Yeo et al., 2011). This technique allows the damage to functional connectivity to be identified in patients with severe functional deficits without the need for patients to perform long and complex tasks in the MRI scanner. For example, Kocher et al. reported a significant correlation between the connectivity of regions in default mode networks (e.g. a major functional brain network) and cognitive performance in healthy controls. However, this correlation disappeared in glioma patients, suggesting the potential functional deficit in the patient group (Kocher et al., 2020).

Nonetheless, the current application of fMRI is still limited by its longer scanning time (fMRI: 1 hour vs anatomical MRI 30 minutes) and lower resolution (fMRI: 3-4mm vs anatomical MRI 1mm) compared to other MRI modalities. Hence it is not routinely collected for patient diagnosis and follow-up.

1.2.3 Diffusion MRI

Diffusion-weighted imaging (DWI) or diffusion-weighted MRI (dMRI) measures the movement of water molecules in tissues (Hagmann et al., 2006). DWI can provide important information about the microstructure of the brain. DWI works by applying a strong magnetic field to the brain and then measuring the movement of water molecules in different brain areas. Water molecules conform to Brownian movements, if without any structural restriction. However, in the brain, the motion of water molecules is restricted by the anatomical microstructures. By measuring the overall diffusivity of water molecules, the microstructure of the brain can be inferred from the signals of DWI (Hagmann et al., 2006).

Gliomas tend to have a different pattern of water molecule movement than normal brain tissue. For example, the water diffusivity inside the tissues is inversely proportional to the cellularity concentration. Hence, vasogenic oedema of gliomas results in higher diffusivity, with increased extracellular water content, whereas cell swelling caused by gliomas produces low diffusivity (Aquino et al., 2017). Moreover, DWI can differentiate between the tumour and surrounding brain tissue (Schmainda, 2012) and could be applied to monitor the response of glioma to treatment experimentally. For example, after surgery or other treatment, follow-

up DWI scans can be used to assess the extent of the tumour and determine whether it is responding to treatment or is recurring (Hein et al., 2004).

While the initially developed DWI techniques can only measure the overall diffusivity of water molecules, the novel diffusion MRI could measure additional parameters of water molecule movement, such as the direction of movement and the degree of anisotropy, by introducing additional diffusion-weighted gradients in different directions during the acquisition. Several reconstruction models can be used to interpret and analyse the directional data obtained from the novel diffusion MRI (e.g., tensor model, ball-and-stick model) (Mori & Zhang, 2006).

1.2.3.1 Diffusion tensor imaging

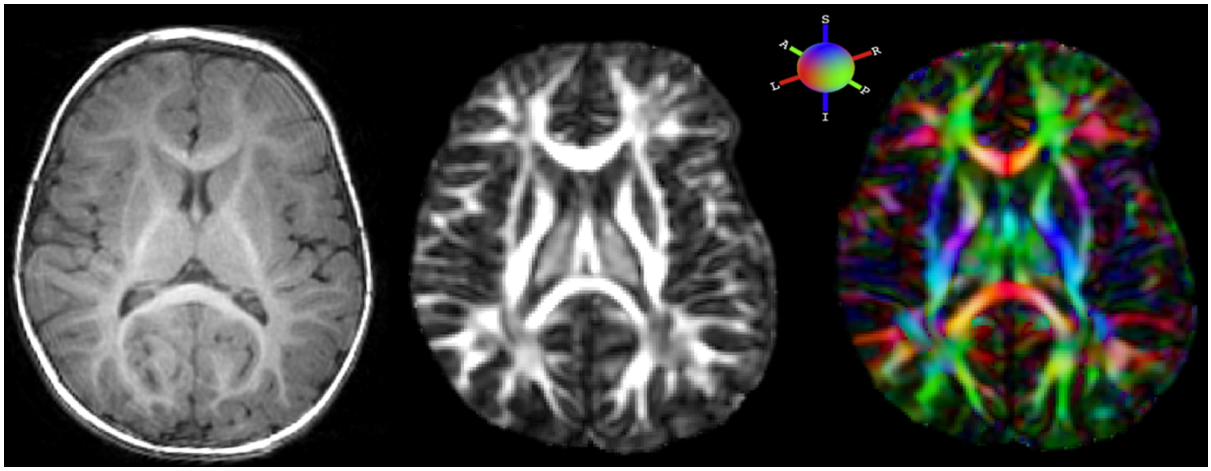


Fig. 1.2. Examples of a T1 MRI (left), fractional anisotropy (middle), and red-green-blue (RGB) coded orientation map (right).

Diffusion tensor imaging (DTI) is a mathematical model commonly used to interpret directional diffusion MRI data **(Fig. 1.2)**. It is worth mentioning that the term DTI was initially proposed for representing the new DWI acquisition technique with direction components. However, recent algorithms could model DWI data with more complex models than tensors (e.g. ball-and-stick). Hence in this thesis, DTI is only referred to as a modelling

technique instead of an imaging acquisition technique to avoid confusion.

DTI assumes that the movement of water molecules is restricted in specific directions and can be described by a 3D tensor. The tensor model of DTI consists of two parameters: eigenvectors and their corresponding eigenvalues. In each voxel, the corresponding eigenvector of the largest eigenvalue is called the principal diffusion direction. If three eigenvalues are close to each other, the diffusion is isotropic, and if they are distinct, the diffusion is anisotropic. Anisotropy is defined as the degree to which the movement of water molecules is restricted in specific directions (Mori & Zhang, 2006). Previous studies showed that in the normal brain, water molecules move faster in a parallel direction to white matter tracts than perpendicularly (Mori & Zhang, 2006). With this principle, the orientation of the white matter tracts can be estimated by the tensor model. At the same time, meaningful information about the microstructure of the brain and tumours can be extracted **(Fig. 1.3)**.

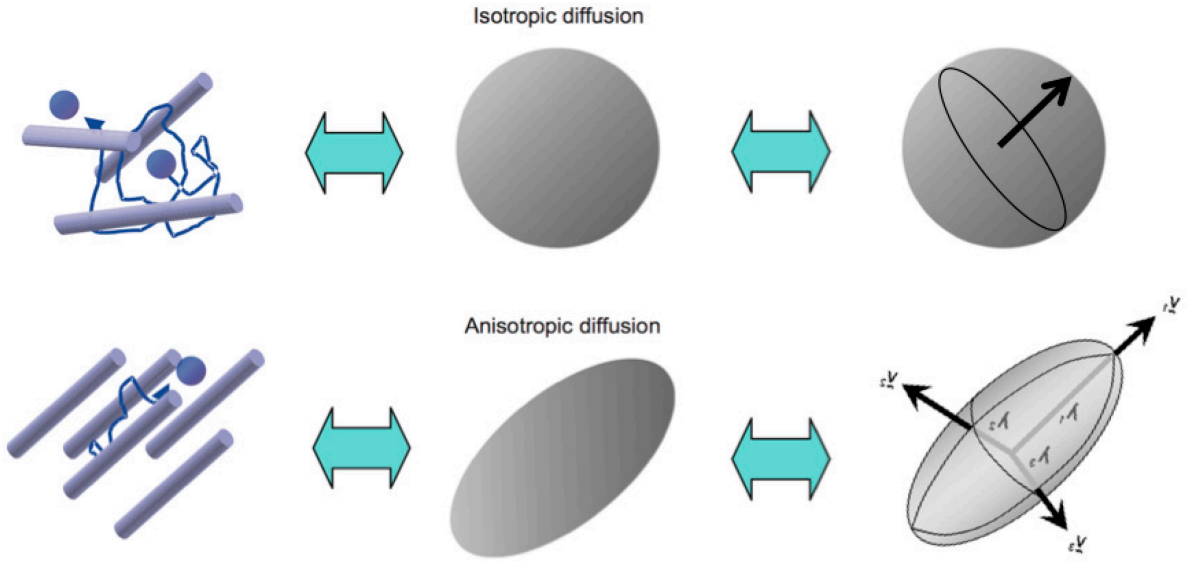


Fig. 1.3. Concept map of water molecules' isotropic and anisotropic movement. Reprinted from (Alghamdi, 2023)

1.2.3.2 Quantitative scalar maps

One way to analyse diffusion MRI is to calculate the scalar map from the tensor model. Commonly used scalar quantification includes Mean diffusivity (MD) and Fractional

Anisotropy (FA). MD can be calculated by averaging three eigenvalues, while FA quantifies the ratio of the anisotropic components to the isotropic components in each voxel (Vorona & Berman, 2015) following the Equation 1.1 below:

$$\mathrm{FA} = \sqrt{\frac{(\lambda_1 - \mathrm{MD})^2 + (\lambda_2 - \mathrm{MD})^2 + (\lambda_3 - \mathrm{MD})^2}{2({\lambda_1}^2 + {\lambda_2}^2 + {\lambda_3}^2)}} \qquad (1.1)$$

where FA is fractional anisotropy; MD is mean diffusivity; λ represents three eigenvalues of the tensor model respectively.

Quantitative scalar maps derived from diffusion MRI are widely applied to characterise brain tumours for patient stratification and prognosis with voxel-based methods such as Radiomics (Chaddad et al., 2019; Han et al., 2018) and Tract-Based Spatial Statistics (TBSS) (Sinha et al., 2020; Smith et al., 2006).

Radiomics are widely applied to multi-modal MRI, including anatomical MRI (e.g. T1, T2) and quantitative physiological MRI (e.g. the scalar map of diffusion MRI) for extracting information about the appearance, shape, size, and texture of brain tumours. Once extracted, these features can be input into machine learning models for characterising brain tumours and predicting patients' genotypes or prognoses. Han et al. applied multi-modal MRI, including T2-FLAIR and DWI, with a radiomics approach to predict the 1p/19q co-deletion in low-grade glioma patients (Han et al., 2018). Results showed that the model with radiomics signatures achieved a higher area under the curve (AUC) of prediction than the model using only clinical variables.

TBSS is usually applied for analysing the microstructural organisation of white matter tracts in the brain, which involves the creation of a standard white matter skeleton presenting the major white matter pathways in the brain (Smith et al., 2006). This skeleton is created by thresholding the fractional anisotropy maps of all the subjects in the study. The resulting skeleton represents the regions of the brain where the FA values are above a certain threshold, which corresponds to the central locations of the major white matter tracts. TBSS is commonly used for identifying the group differences in white matter microstructure. Sinha et al. applied TBSS to glioblastoma patients to identify the association between the surgery-related deficit and white matter tracts. A significant association was found between the

increase in emotion recognition deficits and the fractional anisotropy in several fasciculus tracts (Sinha et al., 2020).

In general, the radiomics studies focused on extracting personalised hand-crafted features from local tumour regions of the quantitative scalar map. In contrast, TBSS studies focused on group differences in the global white matter integrity caused by brain tumours. Although both methods delivered significant clinical discoveries, they are limited by the voxel-based nature of the methodology and could not comprehensively analyse the global disruption of brain tumours. In contrast, studies suggested the widespread tumour invasion beyond the tumour core commonly defined by the T1 contrast images (Li et al., 2019). For example, a recent study reported that the relative invasiveness coefficient calculated from regions of interest in anatomical MRI and diffusion MRI is significantly associated with patient survival, which revealed the peritumoral invasion beyond lesions defined by anatomical MRI (Li et al., 2019). Another study indicated that different diffusion patterns of peritumoral regions are associated with different patient outcomes, which suggested the heterogeneous invasion patterns of gliomas. Those studies indicate the early invasion in the normal-appearing regions defined by the anatomical MRI and suggest the necessity of studying the whole brain disruptions of brain tumours (Li et al., 2019).

1.2.3.3 Tractography

Another way to analyse diffusion MRI is to perform tractography, which reconstructs white matter tracts with three-dimensional models to study the microstructure of the brain. Mainly, tractography can be classified into deterministic and probabilistic tractography **(Fig. 1.4)**.

The most popular widely used deterministic tractography is the Fibre Assignment by Continuous Tracking (FACT) algorithm, which starts tracking with seed points in the white matter and continuously follows the principal directions of each voxel in a step-wise approach (Mori & Van Zijl, 2002) to reconstruct whole brain tractography with diffusion tensor models. Although the deterministic algorithm is fast and straightforward, it is challenged by the crossing fibre problem, which is defined as the difficulty in reconstructing

the trajectories of white matter fibres in the brain from diffusion MRI data when those fibres cross each other within the same voxel (Tournier et al., 2012).

Probabilistic tractography algorithms are developed to tackle the crossing fibre problem. For example, Behrens et al. developed a probabilistic tractography based on the ball-and-stick model: first, the ball-and-stick model was applied to estimate the distribution of diffusion parameters for each voxel (Behrens et al., 2007; Behrens et al., 2003). Next, the probabilistic tracking algorithm repetitively samples from the distribution of voxel-wise principal diffusion directions and produces streamlines through these local samples. In this way, a probabilistic streamline can be generated from the distribution of the location of the true streamline. (Behrens et al., 2007; Behrens et al., 2003).

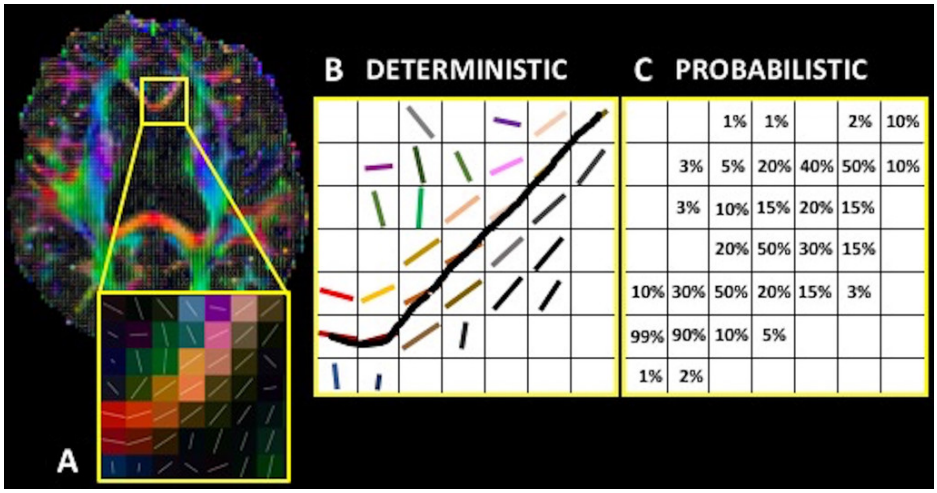
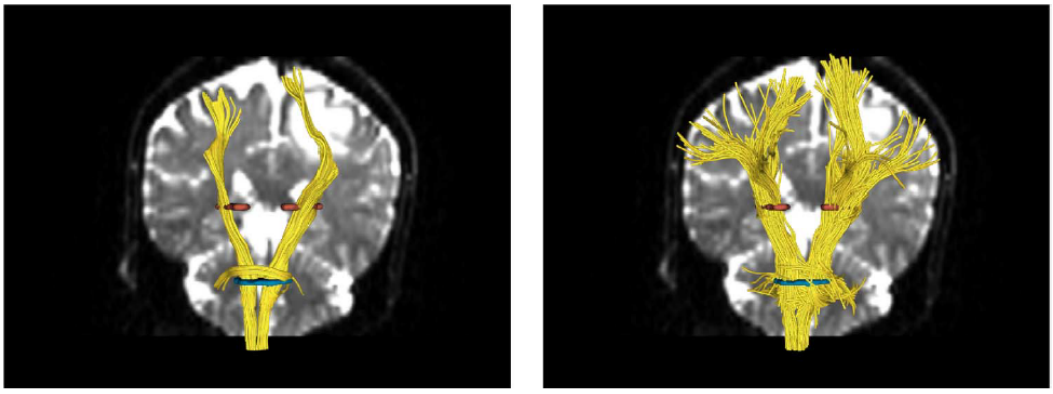


Fig. 1.4. (A): Degree of anisotropy. (B): Deterministic fiber tracking; the fiber path across voxels is inferred based on a single diffusion orientation per each voxel. (C): Probabilistic fiber tracking; tractography generated based on a probability distribution of diffusion orientations within each voxel. Reprinted from (Muller et al., 2018)

The most typical clinical application of tractography in neuro-oncology is surgical planning for tumour resections (Rossi et al., 2018). For example, tractography can be performed before surgery to visualise the white matter bundles/pathways surrounding the tumour to avoid damage to functionally meaningful white matter connections during the resection for fewer deficits. However, there are limitations when applying tractography in tumour-bearing diffusion MRI. For example, traditional algorithms of tractography are

unable to track inside peritumoral oedema, which disrupts the diffusion environment of water molecules **(Fig. 1.5)**. Similar impact also causes unrealistic tracking results, such as belt-like fibres surrounding the tumour (Schult et al., 2019) **(Fig. 1.6)**. Specifically, Deterministic tractography shows a belt of circular fibres surrounding the cavernous region (arrows in **Fig 1.6**), which is not consistent with other clinical findings in T1 and T2 images, as well as anisotropy features in diffusion MRI.



(a) single-tensor UKF tractography (b) two-tensor UKF tractography

Fig. 1.5 Two-tensor UKF (Unscented Kalman filter) tractography (a) has better tracking inside oedema performance than single-tensor UKF tractography (b). Reprinted from (Liao et al., 2017)

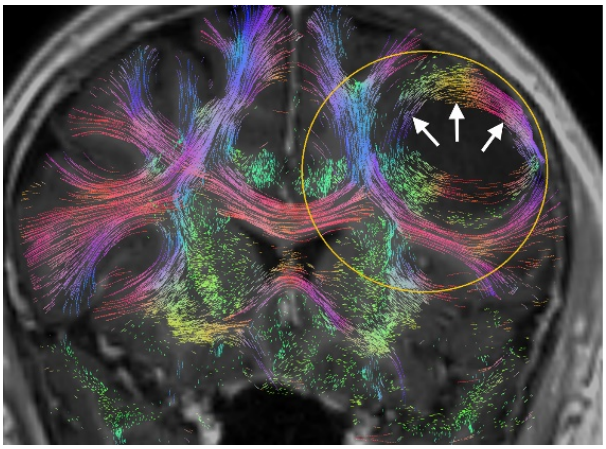


Fig. 1.6 An unrealistic belt of fibres surrounding the core of the lesion. Reprinted from (Schult et al., 2019).

Although novel algorithms such as two-tensor Unscented Kalman filter (UKF) tractography managed to tackle the challenges of tracking in complex brain environments

with brain tumours (Liao et al., 2017) **(Fig. 1.5)**. The results are not quantitatively comparable with healthy controls since the algorithm usually needs to be tuned with much higher sensitivity, which produces high false positive tracts. Hence, although the algorithms could be powerful in qualitative visualisation, it would be challenging to generate statistical results.

Due to the above considerations, instead of directly performing tractography in patients, some studies applied tractography in healthy subjects to identify commonly existing major white matter tracts inside functional circuits (Allan et al., 2019). Doctors then identify essential functional circuits surrounding the tumour for surgical planning to maximise the functional preservation of patients. However, this approach is also limited by its qualitative nature. Overall, there is a pressing need for an approach that could systematically analyse the global white matter connectivity in brain tumour patients.

1.3 Network neurosciences

1.3.1 Brain networks

The brain is known as a natural network that consists of around 100 billion neurons connected by around 100 trillion synapses. However, the massive size of the neuron network poses significant challenges to statistical analysis. A novel field of neurosciences called network neurosciences emerged to model the connectivity of the brain as brain networks (Bassett & Sporns, 2017) by considering the macro-scale of brain regions instead of micro-scale neurons as the elements. This macro-scale brain network, also known as ***connectomics*** or ***connectome***, is a mathematical model called a graph consisting of the structural and functional connections (defined as edges) between different brain regions (defined as nodes). Particularly, cortical and sub-cortical regions are primarily defined as brain nodes as they are usually responsible for executing brain functions. In contrast, the functional correlation or structural white matter connections between cortical regions are mainly defined as brain edges representing the functional or structural pathway of information communication. By constructing macro-scale brain networks with fewer elements of nodes and edges, it becomes

more feasible to use conventional graph-based statistical models (e.g., graph theory) to analyse the organisation of brains.

Network neuroscience involves the use of various MRI techniques, such as resting-state functional MRI and diffusion MRI, to respectively measure the functional and structural connectivity between different brain regions (Bassett & Sporns, 2017).

The functional brain network is constructed by analysing the connectivity patterns (e.g. correlation) between the Blood Oxygen Level Dependent (BOLD) signals of different brain regions (Park & Friston, 2013). Remarkably, functional brain networks can be studied to determine whether there are any changes in how different brain regions communicate with each other after the occurrence of brain tumours in patients, as the changes in communication or connectivity might reflect the changes in brain functions. For example, Kocher et al. discovered that reduced connectivity of the left parietal and temporal nodes of functional brain networks in glioma patients is related to their cognitive outcome (Kocher et al., 2020)

The structural brain network was first introduced by Olaf Sporn and Patric Hagmann independently in 2005 (Hagmann et al., 2006; Sporns et al., 2005). It was defined as a network that describes all possible white matter connections derived from tractography among the different brain regions. Gliomas were found to disrupt the white matter tracts of the brain (Wang et al., 2022), leading to changes in the organisation of the structural brain networks (Yu et al., 2016). Hence, studies of structural brain networks in brain tumour patients can potentially help identify any structural changes associated with the tumour or treatments. These can be further used to guide the development of targeted therapies and interventions to help improve the prognosis of brain tumour patients.

1.3.2 Graph theory

Graph theory is a branch of discrete mathematics that studies graphs, which are mathematical structures used to model pairwise relations between objects (Trudeau, 2013). A graph consists of vertices (also called nodes) and edges (also called links or connections) that connect pairs of vertices. The objects represented by vertices can be anything from people and cities to websites and molecules, while the edges represent relationships or connections

between these objects. Graph theory provides a general framework for studying complex systems by modelling their components and relationships as graphs, which can then be analyzed using various graph algorithms and theorems.

Graph theory is widely applied to analyse the topological patterns of the brain network, reflecting how different brain regions interact. Hence, this thesis also refers to graph theory features as topological features.

A critical measure in graph theory is the path, defined as a sequence of nodes connected by edges. The length of a path is defined as the number of edges it contains. According to graph theory, the length of a path measures the topological distance between brain regions in brain networks, reflecting the ease with which information can flow. As such, the inverse of the path is called efficiency. Commonly-used quantitative features of the path and the efficiency of brain networks include characteristic path length and global efficiency. The characteristic path length is defined as the average shortest path length in the network, while global efficiency is the average inverse shortest path length in the network (Rubinov & Sporns, 2010).

Another vital measure in graph theory is the degree of a node, which is the number of edges connected to it (West, 2001). In a brain network, the degree of a node reflects the number of connections a particular brain region has with other regions. High-degree nodes, also known as hubs, are often considered more central within the network. Hubs are highly connected and may be vital in transmitting information throughout the network (Rubinov & Sporns, 2010).

Finally, clustering features are also essential measures for brain networks (Rubinov & Sporns, 2010). Clustering features quantify the degree to which nodes in a graph tend to form clusters or communities. For example, the clustering coefficient measures the degree to which a node's neighbours are also connected. High clustering coefficients for brain regions might suggest that these regions are specialised in specific cognitive processes (Bassett & Bullmore, 2009). Another important clustering feature is modularity which measures the degree to which the graph nodes can be divided into distinct, non-overlapping communities. High modularity might indicate the presence of different functional systems or subsystems within the brain (Sporns & Betzel, 2016).

1.3.2.1 Main Findings on brain networks

Most research on brain networks focuses on human brain mapping or neurodegenerative diseases, such as Alzheimer's diseases. Several large open-access databases, including human connectome projects (HCP) (https://www.humanconnectome.org/) and Alzheimer's Disease Neuroimaging Initiative (ADNI) (http://adni.loni.usc.edu/), were published to boost the development of this area. Early brain mapping studies have found that the human brain has similar features as other complex networks like social networks. For example, brain networks and social networks both show a similar property called the small-world. In small-world networks, most nodes can be reached from every other node in a few steps, even though most nodes are not directly interconnected. Particularly, small-world networks have low characteristic path length and high clustering. This type of network was found to have high efficiency in transferring information while maintaining a small number of connections (Rubinov & Sporns, 2010).

In neurodegenerative disease, studies showed that neurological deficits could lead to trivial disruption in brain network features. For example, decreased efficiency of several nodes and altered small-world properties was found to be related to Alzheimer's disease and behaviour deficit (Lo et al., 2010). A significant decrease in global and local efficiency was also reported in patients with multiple sclerosis (Shu et al., 2011). Methodology in those areas established the fundamental pipeline of brain network research: 1) parcellate/separate brain regions with node atlas by co-registration, 2) estimate the connectivity between pairwise nodes (e.g., fibre tracking from DTI, the correlation for fMRI), 3) calculate graph theory features, 4) identify if there is significant alternation in graph theory features or significant association between clinical variable and graph theory features (Bassett & Sporns, 2017).

1.3.2.2 Findings on brain networks with brain tumours

Due to limited data, there are fewer brain network studies on brain lesions, e.g., strokes, traumatic brain injuries and brain tumours, than neurodegenerative diseases. However, the organisation of brain networks during brain lesions' development could help us understand

brain function and disease pathologies.

Alternations of connectivity and graph theory features were widely identified in the brain networks of brain tumour patients. Particularly for structural brain networks, higher connectivity between the hub and non-hub regions was discovered in glioma patients than in healthy controls (Douw et al., 2019). Moreover, decreased global efficiency was found in glioma patients (Amoah & Crimi, 2016) and adult survivors of paediatric brain tumours (Na et al., 2018), which may reflect the disruption in the connectome integrity. Local efficiency, clustering coefficient and characteristic path length were reported to be higher in glioma patients than in controls (Amoah & Crimi, 2016). Significant alternation was also widely identified in functional brain networks. For example, lower connectivity between hub and non-hub regions was identified in glioma patients, opposed to the discovery in structural brain networks (Derks et al., 2017). Global efficiency was lower in glioma patients than in controls, indicating that long-distance information transmission was reduced in patients (Huang et al., 2014; Xu et al., 2013). In summary, those findings indicate the global disruption of brain networks in patients, which could be potentially caused by the widespread tumour invasion beyond focal lesions

Furthermore, some of the alternations in graph theory features are found with clinical significance. Hub-non-hub connectivity of structural brain networks was found to be significantly associated with patient cognition, whereas hub-hub connectivity was found to be related to IDH mutation status (Douw et al., 2019). Additionally, global efficiency and clustering coefficient were reported to be significantly associated with cognitive flexibility (Na et al., 2018). Similarly, the z-score of abnormal connectivity in functional brain networks was reported to be significantly associated with cognitive function and tumour biology (Stoecklein et al., 2020). Glioma patients' shortest path length and global efficiency correlate with cognitive performance. (Huang et al., 2014; Xu et al., 2013). The above findings suggest that the integrity of brain networks is vital for maintaining cognitive functions and may reflect tumour aggressiveness. In general, functional and structural brain network studies implied that the brain tumour should no longer be considered a focal disease as it generates widespread impact across the whole brain structure and function.

Although significant results were reported from brain networks of brain tumours, those

results would need to be interpreted with caution as several studies also reported contradictory results for structural brain networks. For example, Amoah et al. reported significantly higher clustering coefficients in low-grade patients (Amoah & Crimi, 2016). In contrast, Ling et al. 2017 reported no significant differences between patients and controls (Ling et al., 2017). Similarly, Liu et al. reported lower local efficiency in glioma patients (Liu et al., 2020), whereas Ling et al. reported no significant difference in local efficiency between glioma patients and controls (Ling et al., 2017). Those contradictions might be caused by the current limitation of constructing structural brain networks. Notably, apart from the challenges of performing tractography in brain tumours (described in Section 1.2.3.3), the registration errors caused by the mass effect of tumours could also introduce bias to the brain networks. Hence the reproducibility and reliability of the structural brain network study with the conventional network-constructing approach for brain tumour patients could be prone to false positive results. Overall, there is a need for the development and evaluation of robust methodology to construct structural brain networks.

Additionally, the current brain network analysis only measures changes in nodal or global graph features that focus on the connectivity of grey matter regions, ignoring that many brain tumours occur on white matter tracts. Consequently, the nodal graph theory analysis could underestimate the global white matter damage. These limitations of existing graph theory analysis reveal a research gap in analysing tumour impact from the perspective of white matter tracts or brain network edges.

1.3.3 Machine learning for brain networks

1.3.3.1 Graph Theory and Machine Learning

Conventional graph theory analysis is limited in different aspects. First, traditional statistical analyses are mainly hypothesis-driven and only focus on limited individual graph theory features. Analysis with a large number of features with multiple comparisons would reduce the statistical power. Second, the statistical analysis primarily measures group differences and group associations between graph theory features and clinical variables,

whereas heterogeneous personalised characterisation is difficult. Finally, statistical analysis usually delivers linear association between graph theory features and clinical variables, which might ignore the patterns of complex associations.

Machine learning could potentially address those limitations of traditional statistics. Machine learning is a method of training models to learn from data without explicitly programming them. Once trained, the model can be applied to new, unseen data to perform prediction tasks. Firstly, the machine learning approach is data-driven and does not require manual feature selection, which could reduce the risk of manually dropping potentially important graph theory features. Second, a trained machine-learning model could make predictions for individual patients, enabling personalised characterisation. Finally, machine learning utilises algorithms capable of learning complex data patterns.

Machine learning approaches have been proven powerful in analysing graph theory features for predicting tasks. Fagerholm et al. proposed a method to predict the presence of traumatic axonal injury and associated cognitive impairment (Fagerholm et al., 2015), which comprehensively included 23 graph theory features. Those graph theory features were applied to train support vector machines, which achieved a performance of 93.4% in classifying the patients with a history of traumatic brain injuries. Moreover, graph theory features were found to be significantly associated with cognitive performance. Through feature selection, betweenness and eigenvector centrality were essential for the correct prediction. Similarly, Liu et al. applied a machine learning approach by applying the support vector machine to graph theory features from functional and structural brain networks to predict the survival outcome of high-grade glioma patients, achieving 75% accuracy (Liu et al., 2016). The top three crucial graph theory features extracted from functional and structural brain networks are the clustering coefficient, shortest path length, and global efficiency.

Although machine learning approaches achieved high prediction accuracy, the results must be carefully interpreted since the model could be overfitted to the training data due to the small size of training samples in both studies. Additionally, such methods rely on the robustness of brain networks and the reliability of graph theory features, which could be particularly challenging for tumour patients.

1.3.3.2 Deep Learning and Brain Networks

Deep learning is a special machine learning technique that learns from input data patterns with deep neural networks. Deep learning offers distinct benefits that set it apart from machine learning. For example, most deep learning models are trained in an end-to-end approach, which does not require feature extraction and selection. Generally, deep learning models are found with higher performance than machine learning models and achieve state-of-the-art performance for medical images in a wide range of prediction tasks (Shen et al., 2017).

Deep learning models usually require a large sample size for model training. Hence, it was generally applied in the clinical field where large samples are available (Çallı et al., 2021). An increasing number of brain tumour studies published their data in recent years, which boosted the development of deep learning in brain tumour research, such as tumour segmentation and outcome prediction (Clark et al., 2013). However, those tasks only focus on the local heterogeneity in MRI of brain tumours and entirely ignore the normal-appearing regions, whereas studies showed the widespread potential for tumour invasions outside the so-called tumour-ground-truth regions defined by anatomical MRI(Li, Wang, Yan, Torheim, et al., 2019).

Notably, deep learning models for brain networks are still in the early developing stage. Brain network models have mainly been developed for healthy subjects or neurological diseases such as Alzheimer's diseases, thanks to the publication of the large open cohort (e.g., ADNI and HCP in **Section 1.3.2.1**). BrainNetCNN was the first specialised deep learning model based on convolutional neural networks (CNN), which was designed for predicting clinical neurodevelopment outcomes from brain networks. This model achieved state-of-art (SOTA) performance in identifying an infant's postmenstrual age (Kawahara et al., 2017). BrainGNN is another SOTA deep learning model that utilises the specialised neural network for graphs called graph neural networks (GNN) (Li et al., 2021), providing the highest prediction accuracy comparing with BrainNetCNN and machine learning methods and results with visual interpretation. Specifically, GNNs are a class of deep-learning models designed to handle graph-structured data. They have gained significant attention in recent years due to

their ability to capture complex patterns in graph data, which is often not possible with traditional machine-learning methods (Bronstein et al., 2017). The fundamental principle behind GNNs is the notion of message passing or information propagation among neighbouring nodes in a graph. GNNs operate by iteratively updating the node features based on the features of their neighbouring nodes and the edges connecting them (Gilmer et al., 2017). The core idea is to capture both local and global information in the graph structure by encoding it into the node features.

Although BrainNetCNN and BrainGNN are both SOTA for different brain diseases, they are not specially designed for tumour-bearing brain networks, which require additional tailor according to the properties of the tumour (e.g., widespread invasion from tumour core to remaining brain networks).

In summary, there is a research gap in deep learning for brain networks of brain tumours. It would be promising to use deep learning of brain networks in brain tumour patients to investigate tumour invasion and structural integrity and increase model explainability. Nonetheless, additional consideration would be required to apply graph-learning models on tumour-bearing structural brain networks.

1.4 Hypothesis

1.4.1 General hypothesis

The **General Hypothesis** of this thesis is as follows: The tumour disruptions of brain organisations could be characterised by a network neuroscience approach called brain networks that regard brain regions as nodes and white matter connectivity as edges. On the one hand, the brain network itself can characterise tumours to improve patient prognosis with traditional statistics. On the other hand, the brain networks can serve as an additional data modality to characterise tumour aggressiveness from the view of global disruption and collaborate with other data modalities to deliver better prediction for deep learning models (e.g., image, geometrics).

1.4.2 Hypothesis tested

1. One research gap identified in Chapter 1 is that existing approaches for constructing brain networks are not robust enough for brain tumour patients. As discussed in Section 1.3.2.2, mass effect and oedema of brain tumours might cause errors when constructing brain networks. I hypothesised that a novel approach developed from a tractography template and white matter skeleton could produce more robust brain networks with higher clinical and functional relevance than traditional approaches for brain tumour patients. The hypothesis is tested in **Chapter 2** and evaluated by comparing the proposed approach with traditional methods for several functional metrics and graph theory features of brain networks

2. Another main finding in Chapter 1 is that tumour cells might invade through white matter tracts. Hence, I hypothesise that structural brain networks representing white matter connectivity have the potential to characterise the early invasion of glioblastomas. I also hypothesise that the disruptions of brain networks are associated with patients' cognition, performance, and survival time. While brain networks are constructed with the methodology developed in Chapter 2, the hypotheses are tested with correlation tests, mediation models, linear regression, t-tests and cox proportional hazard models to evaluate the association between brain networks and clinical variables in **Chapter 3**.

3. Inspired by the result in Chapter 3, which suggests the importance of tumour-disrupted brain networks beyond focal lesions, I hypothesise that it is also feasible to construct brain networks from anatomical MRI with the assistance of anatomical priors and deep learning-based feature extraction. Furthermore, I hypothesise that models that learn from brain networks could better predict genotypes of gliomas than models that only learn from tumour images. The hypotheses are tested by performing a task of predicting IDH mutation status in glioma patients in **Chapter 4**.

4. Motivated by the clinical significance of brain networks in brain tumour patients in Chapter 3 and the success of radiomics in gliomas discussed in Section 1.2.3.2. I hypothesise that multi-modal data might reflect the different views of the same tumour's invasiveness. Notably, brain networks reflect the heterogeneity of the global glioma invasion, whereas tumour geometrics and images reflect the tumour invasion's local aggressiveness. Hence I

hypothesise that multi-modal learning could better characterise tumours to predict the genotypes. The hypothesis is tested in **Chapter 5** by building a multi-modal learning framework for predicting the IDH mutation status from multi-modal data of brain networks, tumour images, and tumour geometrics.

1.5 Clinical Implications

The motivation for this thesis lies in the need for a better understanding of brain tumours using an interdisciplinary approach that combines network neurosciences and deep learning models. By addressing the identified research gaps and testing specific hypotheses, this thesis aims to improve patient prognosis and provide new insights into the characterisation of tumour aggressiveness. The clinical implications for the thesis are as follows:

First, the development of a novel approach for constructing brain networks in brain tumour patients could lead to more robust and clinically relevant networks, providing significant and interpretable information for diagnosis (Chapter 2). Additionally, investigating the association between brain networks and clinical variables could reveal important links between early tumour invasion and patient survival (Chapter 3). Furthermore, the application of deep learning models for constructing brain networks and predicting glioma genotypes could revolutionize the way brain tumours are studied and treated (Chapter 4). Finally, the thesis aims to develop a comprehensive understanding of tumour invasiveness using multimodal learning, potentially leading to more interpretable analysis and personalized treatment strategies (Chapter 5).

Overall, this thesis seeks to make a significant contribution to the clinical field of brain tumour research, providing valuable insights and innovative methodologies that could ultimately improve patient outcomes and advance our understanding of this complex and devastating disease.

Chapter 2. Quantifying structural connectivity in brain tumour patients

This chapter is based on the following conference publication:

Wei, Yiran, et al., "Quantifying structural connectivity in brain tumour patients." *International Conference on Medical Image Computing and Computer-Assisted Intervention*. Springer, Cham, 2021.

2.1 Abstract

Brain tumours are characterised by infiltration along the white matter tracts, posing significant challenges to precise treatment. Mounting evidence shows that an infiltrative tumour can interfere with the brain network diffusely. Therefore, quantifying structural connectivity has the potential to identify tumour invasion and stratify patients more accurately. The tract-based spatial statistics (TBSS) is widely used to measure the white matter integrity. This voxel-wise method, however, cannot directly quantify the connectivity of brain regions. Tractography is a fibre-tracking approach widely used to quantify brain connectivity. However, the performance of tractography on the brain with tumours is biased by the tumour mass effect and water disruption of oedema. A robust method of quantifying the structural connectivity in brain tumour patients is still lacking.

Here we propose a method that could robustly estimate tract strength for brain tumour patients. Specifically, we first construct an unbiased tract template in healthy subjects using tractography. The voxel projection procedure of TBSS is employed to quantify the tract connectivity in patients based on the location of each tract fibre from the template. To further improve the standard TBSS, we propose an approach of iterative projection of tract voxels under the guidance of tract orientation measured by voxel-wise eigenvectors. Compared to the conventional tractography methods, our approach is more sensitive in reflecting functional relevance. Further, the different extent of network disruption revealed by our approach corresponds to the prior clinical knowledge of tumour histology. The proposed method could provide a robust estimation of the structural connectivity of brain tumour

patients.

2.2 Introduction

This chapter is designed to test the first hypothesis proposed in **Chapter 1.4.2** that a novel approach developed from a tractography template and white matter skeleton could produce more robust brain networks than traditional approaches for brain tumour patients.

2.2.1 Brain tumours and white matter tracts

As I introduced in **Chapter 1**, the global impact of brain tumours, especially gliomas, could be potentially characterised by the disruption of global white matter networks or structural brain networks. Particularly, tumour cells are identified to infiltrate and interfere with the white matter tracts (Wang et al., 2019). As a result, the tumour infiltration along white matter tracts may lead to structural disturbance of the brain (Liu et al., 2020). Additionally, brain tumour patients frequently demonstrate neurological deficits that are not directly explained by the focal lesion (Incekara et al., 2018). It is increasingly accepted that brain tumours may cause broader impacts on the global brain beyond the focal site through the white matter tracts (Aerts et al., 2016). Therefore, accurately measuring structural connectivity strength offers a promising imaging surrogate to detect tumour-related brain alterations.

2.2.2 Connectivity strength measurement

As I introduced in **Section 1.2.3,** the recent development of neuroimaging techniques has facilitated the characterisation of brain connectivity at the whole-brain level based on diffusion MRI (dMRI). The derived fractional anisotropy (FA) map is commonly used to measure tract strength. The tract-based spatial statistics (TBSS) is a method to estimate the strength of specific tracts using a FA skeleton derived by mapping the local maxima FA voxels to the template (Smith et al., 2006). As a voxel-based method, however, TBSS fails to consider the spatial continuity of the fibre pathway, which has difficulties in multiple testing

and tracking of the fibres that the tumour infiltrates along (Bach et al., 2014). Further, as the projection procedure in TBSS is purely based on the FA values, the traditional TBSS does not consider the orientation of the tract fibres that are frequently affected in brain tumour patients.

Tractography is a widely used fibre-tracking method to measure tract connectivity. This method has the advantage of detecting the fibre pathway with spatial consistency. However, as I described in **Section 1.2.3.3**, performing tractography on brain tumour patients has the following challenges:

1) The tract pathways in the vicinity of the tumour are often anatomically deviated, which may cause errors and artefacts in fibre tracking.

2) Many brain tumours are remarkably heterogeneous (Parker et al., 2015). Notably, the oedema region surrounding the tumour may cause artefacts in fibre tracking, as the FA value is commonly affected in these regions (Schult et al., 2019).

To tackle those challenges, a specially tailored approach needs to be designed for constructing brain networks of tumour-bearing brains.

2.2.3 Our contributions

We propose a method of estimating structural connectivity for network construction in brain tumour patients without direct fibre tracking on patients (Fig. 2.1). Inspired by a method for traumatic brain injury (Squarcina et al., 2012), we first performed tractography on healthy controls and generated an unbiased tract template, with the location of each tract fibre derived. The TBSS approach was then employed to derive the skeletonised FA maps from patients for estimating the connectivity strength of each specific tract in patients. To mitigate the bias in TBSS voxel projection caused by tumour mass effect, we further proposed an improved TBSS tailored to brain tumours, using an iterative projection of FA voxels guided by the tract orientation based on the voxel-wise eigenvector.

We compared the connectivity strength estimated by the proposed approach and the conventional tractography methods in multiple datasets of brain tumour patients. The results show that our approach reflects more functional relevance. Further, the different extent of network disruption revealed by our approach corresponds to the prior clinical knowledge of

tumour histology.

2.2.4 Related work

The conventional tractography methods include Fibre Assignment by Continuous Tracking (FACT) and Unscented Kalman Filter (UKF) tractography.

FACT tractography (Mori & Van Zijl, 2002) is a deterministic method that tracks fibre streamlines from a seed region by following the primary eigenvector from one voxel to the next. FACT is highly sensitive to the changes in FA and tensor values in the white matter. As a result, the tracking frequently fails when encountering peritumoral oedema, leading to overestimated disruption of the structural networks. In some other cases, it may produce spurious tract rings around the tumour, which may underestimate the connectivity reduction (Chen et al., 2015).

UKF tractography is shown to be able to track inside peritumoral oedema using two tensor models (Liao et al., 2017). However, to achieve this, the model weakly controls the false positive fibres compared to healthy subjects (Chen et al., 2015). The trade-off between false positive and false negative rates is challenging to be optimised among patients, which could particularly cause bias in the group analysis when individual tumours have a heterogeneous extent of peritumoral oedema.

2.3 Methods

2.3.1 Datasets

Three datasets of glioma or meningioma patients were included, with both diffusion MRI (dMRI) and resting-state functional MRI (rs-fMRI) available:

1) Four low-grade gliomas (LGGs), five high-grade gliomas (HGGs) and two meningiomas (dMRI: 60 directions, b = 1000 s/mm2; rs-fMRI: TR = 2.5 s) were obtained from (Pernet et al., 2016);
2) OpenNeuro database: 7 LGGs, 4 HGGs, and 14 meningiomas (dMRI: 101 directions, b = 0,

700, 1200, 2800 s/mm2; rs-fMRI: TR = 2.4 s) (Aerts & Marinazzo, 2019).

3) An in-house dataset: 12 HGGs (dMRI: 12 directions for each b values, b = 0, 350, 650, 1000, 1300, 1600 s/mm2; rs-fMRI: TR = 2.43 s). In total, 11 LGGs, 21 HGGs and 16 meningiomas were included.

We also included the high angular resolution dMRI (b = 1000, 54 directions) from the Alzheimer's disease Neuroimaging Initiative (ADNI, http://adni.loni.usc.edu/) for constructing an unbiased template of white matter (WM) connection with high spatial resolution. Ten elderly healthy subjects were selected from the ADNI-CN (healthy control) research group (mean age 60.9 ± 1.5 years, median age 60.2 years, range 58.4 - 62.1 years, three males).

This study was approved by the local institutional review board of Cambridge University Hospital. For in-house MRI data collection, informed written consent was obtained from all patients.

2.3.2 Overall view of the method

The proposed method includes three main steps:

– Producing an unbiased tractography template (Fig. 2.1A),

– Generating individualised FA skeleton (Fig. 2.1B),

– Combining tractography template with FA skeleton to estimate the connectivity strength between each pair of brain regions in patients.

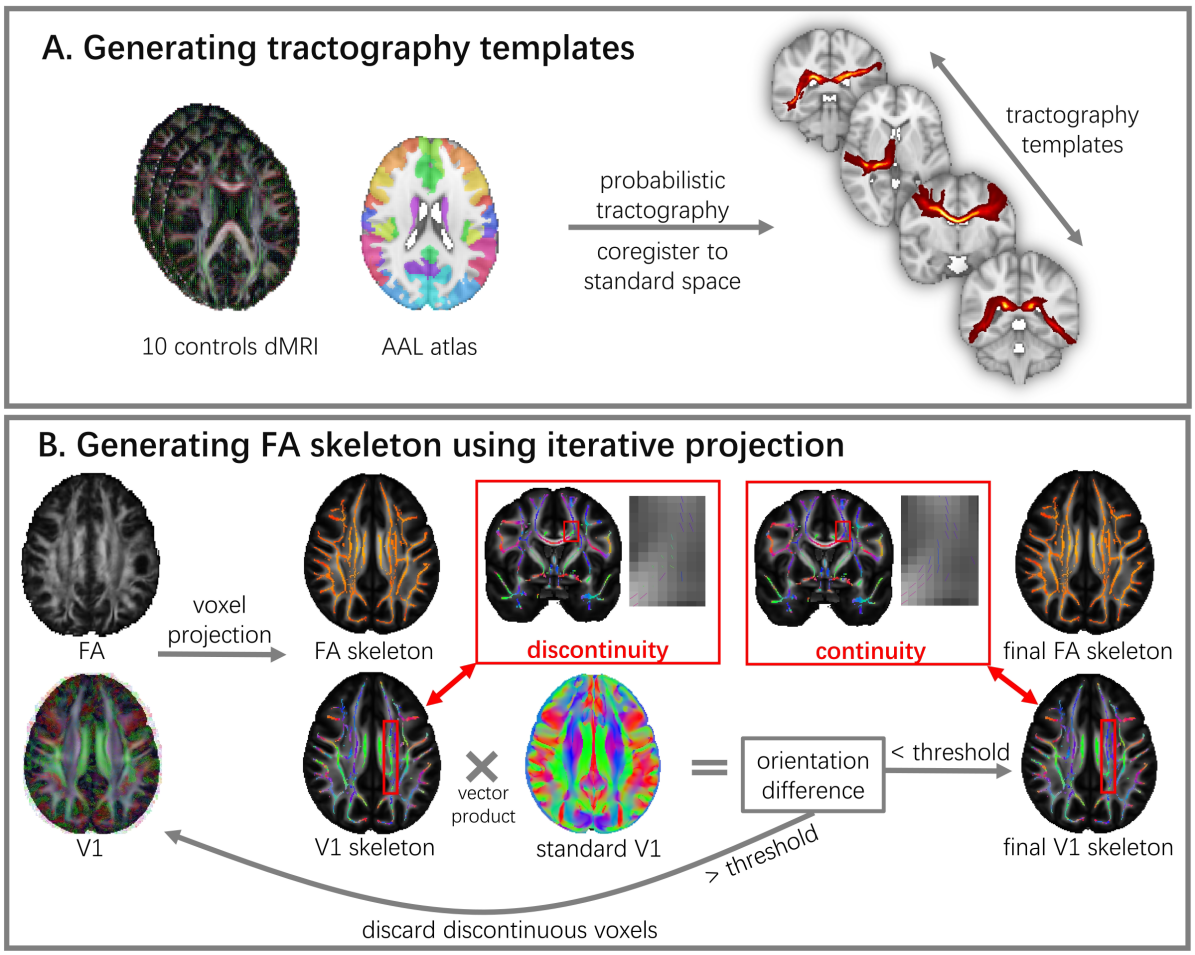


Fig.2.1. Flowchart of network construction. A. An unbiased tractography template is generated using probabilistic tractography in ten healthy subjects to indicate the location of the tracts between brain regions parcellated using the brain atlas. B. By using an iterative projection approach that considers the direction of voxels (V1), a skeletonised FA map with maximum tract continuity can be produced. The red arrows indicate the discontinuity in the FA skeleton from the traditional TBSS that is corrected with our proposed method.

2.3.2.1 Tractography template

An unbiased white tract template was generated in four steps using ten age-matched elderly healthy controls obtained from the Alzheimer's disease Neuroimaging Initiative (ADNI, http://adni.loni.usc.edu/).

In detail, the cortical/subcortical regions on dMRI were parcellated into 90 brain regions using the Automatic Anatomical Labelling (AAL) atlas (Tzourio-Mazoyer et al., 2002) in the

standard space (Grabner et al., 2006). The AAL atlas included the grey-white matter boundary to facilitate tractography. Deformable registration was performed using Advanced Normalization Tools (ANTs) (Avants et al., 2009).

Eddy currents and subject motions in dMRI were corrected using the FMRIB software library (FSL, https://fsl.fmrib.ox.ac.uk/fsl/) eddy tool (version 6.0.0). A crossing fibre model was fitted to each control's dMRI using the FSL function bedpostx. Probabilistic tractography between each pair of the 90 regions was subsequently performed using FSL Probtrackx2 (Behrens et al., 2007). Pairwise probabilistic tractography was performed between 90 regions of AAL atlas (Tzourio-Mazoyer et al., 2002) using Probtrackx2 to generate a path distribution map in healthy controls (Behrens et al., 2007).

Each ROI was used as a seed (starting ROI) and target (ending ROI) once in the tracking. For each pair of seed/target ROIs, 5000 streamlines were sampled from the seed mask. Only the streamlines reaching the target mask were retained. The threshold of tracking curvature was set to 0.2 (80 degrees). Streamline samples were terminated when they had travelled 2000 steps with a step length of 0.5mm or entered the cortical/subcortical regions. Streamlines were discarded if they entered the cerebrospinal fluids in the ventricle or re-entered the seed region.

Distribution maps were generated for all possible WM connections between the 90 cortical/subcortical regions in the healthy controls. The yielded distribution maps were nonlinearly transformed to the MNI-152 space using the ANTs and averaged to mean connection distribution across the controls using fslmaths, which was thresholded to only retain the voxels with top 5% probability, and finally binarised, providing conservative pathways for the template, a tract atlas in the standard space.

2.3.2.2 Individual FA skeleton from the iterative projection

An FA skeleton of each patient was generated at the individualised native space using an improved TBSS approach.

1) We fitted all dMRIs with a tensor model using the FSL diffusion toolbox to generate FA maps. The yielded FA maps were nonlinearly co-registered to a FA template in the standard

space using the deformable function of ANTs, which could mitigate the brain deformation caused by the tumour (Prasanna et al., 2019). This approach could outperform FNIRT (Andersson et al., 2007) (default registration tool in TBSS) in co-registering FA (Schwarz et al., 2014) and pathology-bearing T1 (Ou et al., 2014). To minimise the potential signal-noise ratio effect from different MRI protocols, we normalised the FA maps using the histogram-matching method (Nyúl et al., 2000)

In addition, the corresponding principal eigenvector V1 maps were also transformed into the standard space. Instead of using the patient group thinned FA skeleton, we used the standard FA skeleton (FMRIB58 FA skeleton) of FSL as the target for projection to reduce bias introduced by the tumour.

2) We further improved TBSS, which only projects the voxels with local maximum value at the tract centre on the FA skeleton. Specifically, we compared the principal eigenvector (V1) of the projected voxel to the standard V1 and calculated the orientation difference using the vector product. The voxels with an orientation difference over 90 degrees were discarded, whereas neighbour voxels were selected instead. The projection iteration continued until all voxels on the skeleton converged to a minimum direction difference from the standard FA skeleton. Using this procedure, the continuity of the voxel directions on each tract could be improved. An individualised FA skeleton was generated in each patient.

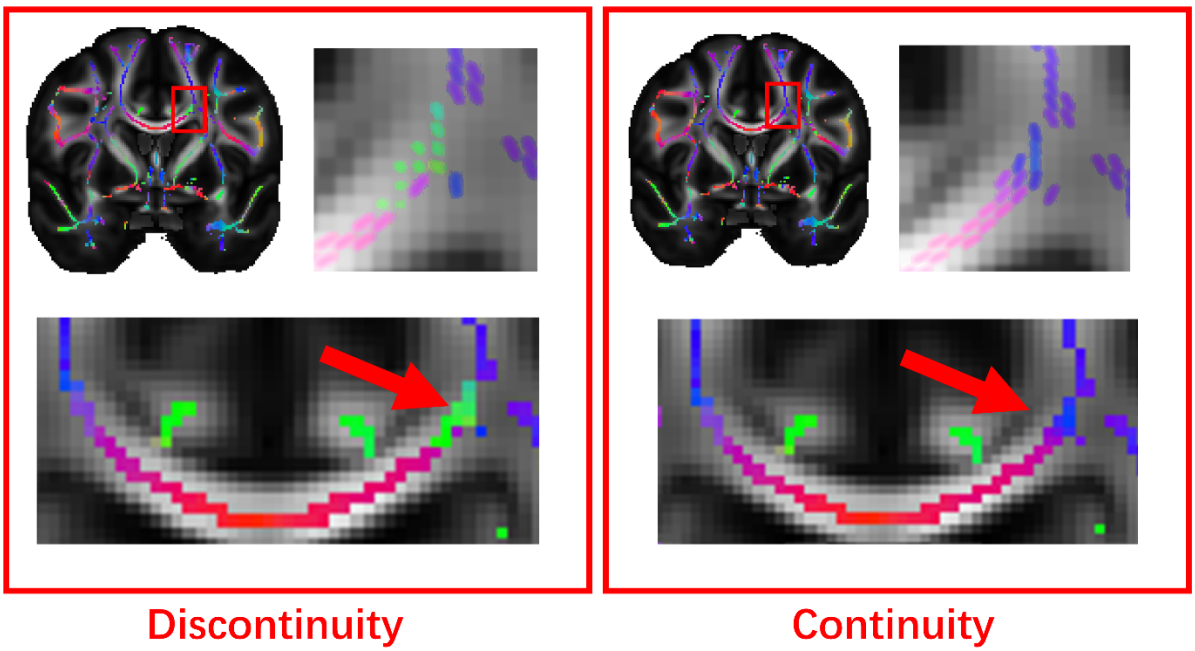


Fig.2.2. Example of corrected tract direction

2.3.2.3 Structural connectivity strength estimation

The segments of the individualised FA skeleton within each tract of the template were extracted and averaged, representing the connectivity strengths of the major tracts.

2.3.3 Correlation between XTRACT and their corresponding edges

XTRACT atlas (Warrington et al., 2020) are well-defined atlas for 42 major white matter bundles from the FSL library. To determine the robustness of the edge strengths estimated with our approach, we compared the strength of connectivity in XTRACT tracts and the strength of edges that correspond to XTRACT tracts. Theoretically, if the edges are robust enough, the damage on the edges should be significantly correlated with the damage on the major tracts bundles. The strengths of XTRACT tracts are determined with a similar approach as the proposed methods by substituting the tractography atlas with the XTRACT atlas. To identify edges that belong to specific XTRACT tracts, we calculate the percentage of overlapping between edge ROIs from the tractography atlas and the tracts ROIs defined by the XTRACT atlas. If over 90% of voxels are inside a specific XTRACT tract, we define this edge as belonging to that XTRACT tract. Because the XTRACT atlas is a non-overlapping atlas, in this way, each tract can be assigned with several different edges. Finally, the correlation between XTRACT and their corresponding edges in the patient group can be calculated. The XTRACT tracts (e.g., middle cerebellar peduncle) without highly overlapped edges are dropped.

2.3.4 Baseline methods

FACT was performed using diffusion toolkits (Wang et al., 2007), while UKF was performed using the UKFTratography packages in 3DSlicer (https://www.slicer.org/) via the SlicerDMRI project (http://dmri.slicer.org) (Norton et al., 2017; F. Zhang et al., 2020). For both methods, the mean FA value of the tracts connecting two ROIs of the AAL atlas was

calculated using MRTrix3 by sampling and averaging the FA values along the streamlines generated by the tractography (Tournier et al., 2019).

2.3.5 Functional brain networks

We constructed functional networks from rs-fMRI using GRETNA (Wang et al., 2015). Firstly, the rs-fMRI signals were regressed, bandpass-filtered, smoothed with a kernel with a full width at half maximum of 6mm and co-registered to the standard space. Secondly, the brain regions of each patient were parcellated using the AAL atlas. Finally, a pairwise Pearson correlation was performed between the mean rs-fMRI signals in 90 brain regions.

2.3.6 Whole-brain structural and functional connectivity coupling

To measure the individualised functional relevance of a structural network, we calculated the whole brain structural connectivity-functional connectivity (SC-FC) coupling. Spearman rank correlation was performed between the non-zero elements of the structural connections with their corresponding functional connections to produce a correlation coefficient for each patient. To compare the group difference, the correlation coefficients were transformed using Fisher Z-Transformation.

2.3.7 Group-wise structural-functional connection correlation

The strength of functional connections varies due to the distinct extent of disruptions in corresponding structural connections. By testing the correlation of each functional and structural connection, the functional connections sensitive to structural damage can be identified. To weakly control the family-wise error in multiple comparisons, we used network-based statistics (NBS) (Zalesky et al., 2010), providing higher sensitivity in controlling the false discovery rate. NBS is a method to control the family-wise error rate (in the weak sense) when mass-univariate testing is performed at every connection comprising the graph. The original method was proposed for significantly different subnetworks between the target group and the control group. In this study, we adapted it for controlling multiple comparisons of correlation with similar approaches.

2.3.8 Difference between SC-FC coupling and structural-functional connection correlation.

In this study, we introduced two methods to quantify the interaction between functional and structural networks: the SC-FC coupling and group-wise structural-functional connection correlation. Specifically, the SC-FC coupling is an individualised coefficient which is calculated by correlating the whole brain-level structural and functional networks. The high SC-FC coupling in patients may suggest the integrity of interaction between structural and functional networks, which require strong sensitivity of structural networks.

In contrast, group-wise structural-functional connection correlation is group statistics. Tumour damage usually causes variations in structural connectivity. As a result, similar variations may also appear in functional connectivity. Hence, we can imply that the method which identifies higher group-wise structural-functional correlation is more sensitive to tumour damage.

2.3.9 Clinical validation

The prior clinical knowledge establishes that meningiomas normally cause less disturbance to the brain than gliomas. A robust network construction method should be sensitive to the difference between meningioma and glioma. We used the global efficiency, calculated according to graph theory, to characterise the brain networks, which were compared in meningioma and glioma patients (Latora & Marchiori, 2001).

2.4 Results

2.4.1 Iterative TBSS projection

Table 2.1. Mean orientation differences between patient FA skeleton and standard FA

Traditional TBSS projection (radians)	Iterative TBSS projection (radians)	*P*-value
0.424 ± 0.057	0.388 ± 0.035	3.8e-4

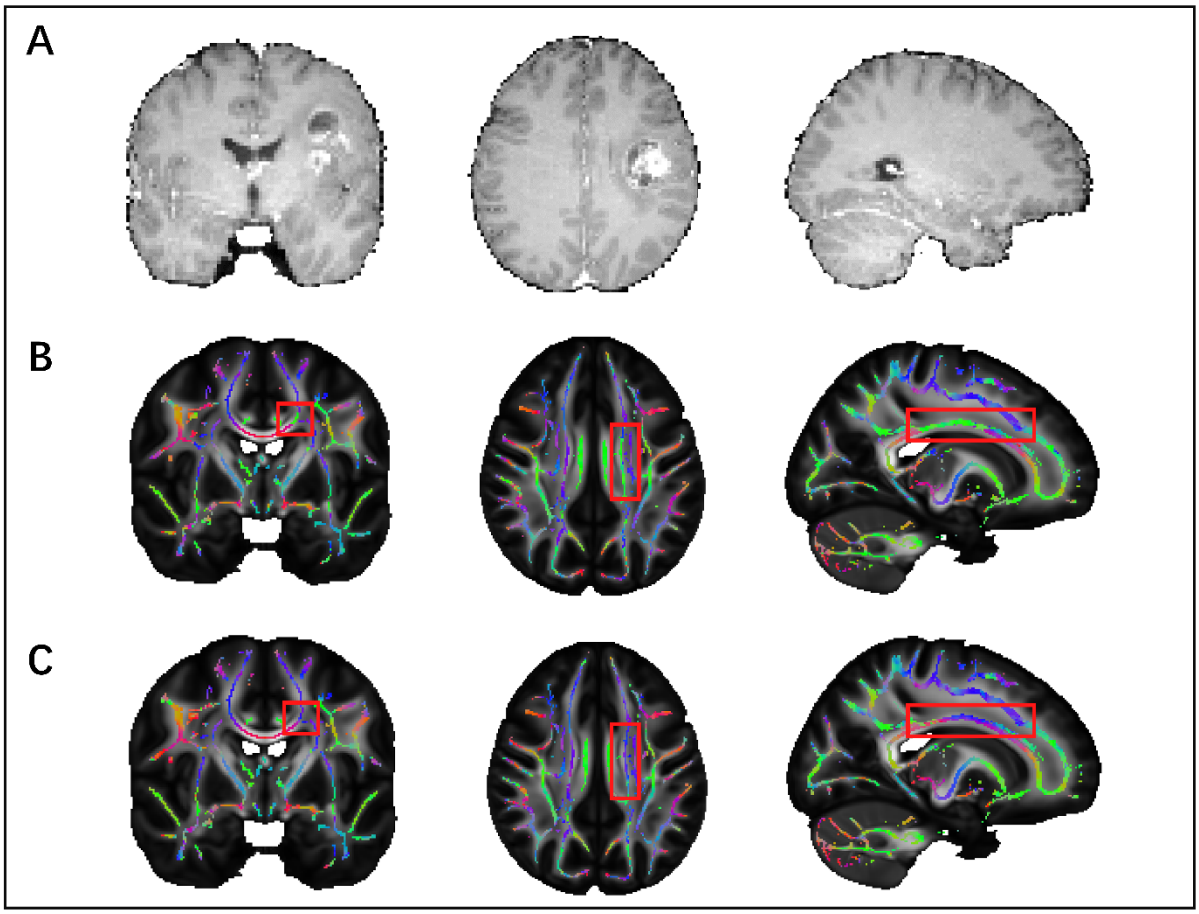


Fig.2.3. Example of voxel projection in coronal (left), axial (middle) and sagittal (right) views. A. T1 contrast MRI indicating tumour location. B. Traditional TBSS voxel projection: the tracts surrounding the tumour display different directions (green) from the contralesional tract (blue). C. The proposed method improves the direction continuity of the tract.

The proposed approach showed smaller orientation differences between patient FA skeleton and standard FA compared to the baseline methods (Table 2.1). One example is illustrated in Fig. 2.2. Tracts that are displaced by the tumour have voxels from the wrong directions projected onto the FA skeleton. In comparison, our approach could ensure the maximum orientation continuity of the tracts.

2.4.2 Correlation between XTRACT and their corresponding edges

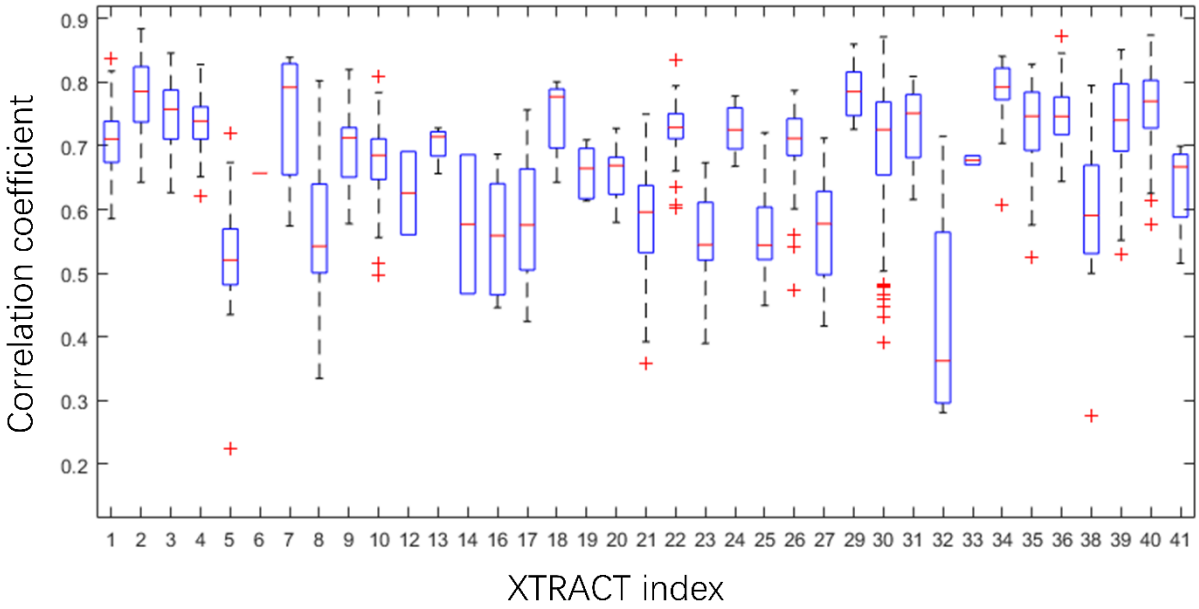


Fig.2.4 Correlation between XTRACT and corresponding edges. Tract indexes 11, 28, and 37 are dropped due to no edges having more than 90% overlapping.

Figure 2.4 shows that 30/41 XTRACT tracts have a strong correlation (r >0.6) with their corresponding edges in patients. Only 1 XTRACT tract (Superior longitudinal fasciculus 1) has a median correlation smaller than 0.5 with its corresponding edges. In contrast, Anterior thalamic radiation has the highest median correlation of 0.78 with its corresponding edges.

2.4.3 Whole brain structural and functional connectivity coupling

Table 2.2. SC-FC Coupling coefficient (z-transformed)

Methods	Mean ± SD	*P*-value (vs FACT)	*P*-value (vs UKF
Proposed	0.25±0.07	3.3e-26	3.5e-8
UKF	0.16±0.08	3.8e-10	-
FACT	0.07±0.05	-	-

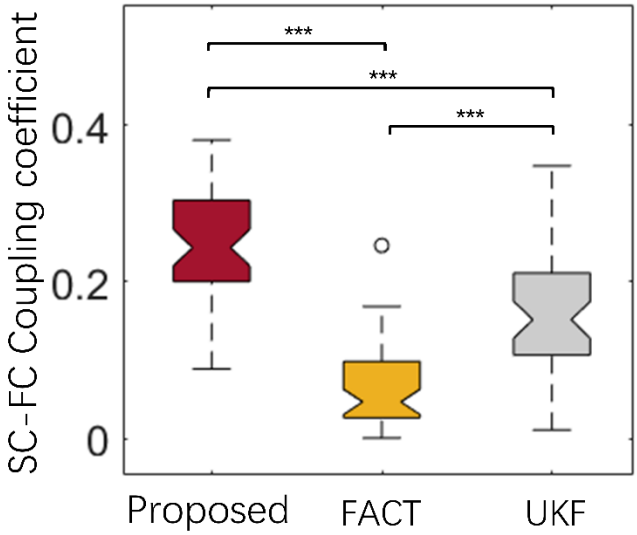


Fig.2.5. Whole brain SC-FC coupling coefficient (z-transformed) derived from three different methods.

The proposed method achieved higher SC-FC coupling (0.25±0.07), which is significantly higher than UKF (0.16±0.08) and FACT (0.07±0.05) (Table 2.2, Fig. 2.5), suggesting the robustness of the brain network constructed using the proposed method. It's worth mentioning that UKF had a higher coupling score than FACT, which implied the strong disruption of a brain tumour on the traditional tractography.

2.4.4 Group-wise structural-functional connection correlation

The proposed method identified significantly correlated (P = 0.0014). Functional and structural sub-networks across the patient group, suggesting its high sensitivity to functional-related structural disruptions (Fig.2.3). Although a subnetwork consisting of 3 edges is also identified from UKF tractography, it does not compose significant power (P > 0.05). It is worth mentioning that most connections in the subnetwork are inter-hemisphere connections, which is partially corresponding to the corpus callosum (Fig. 2.4).

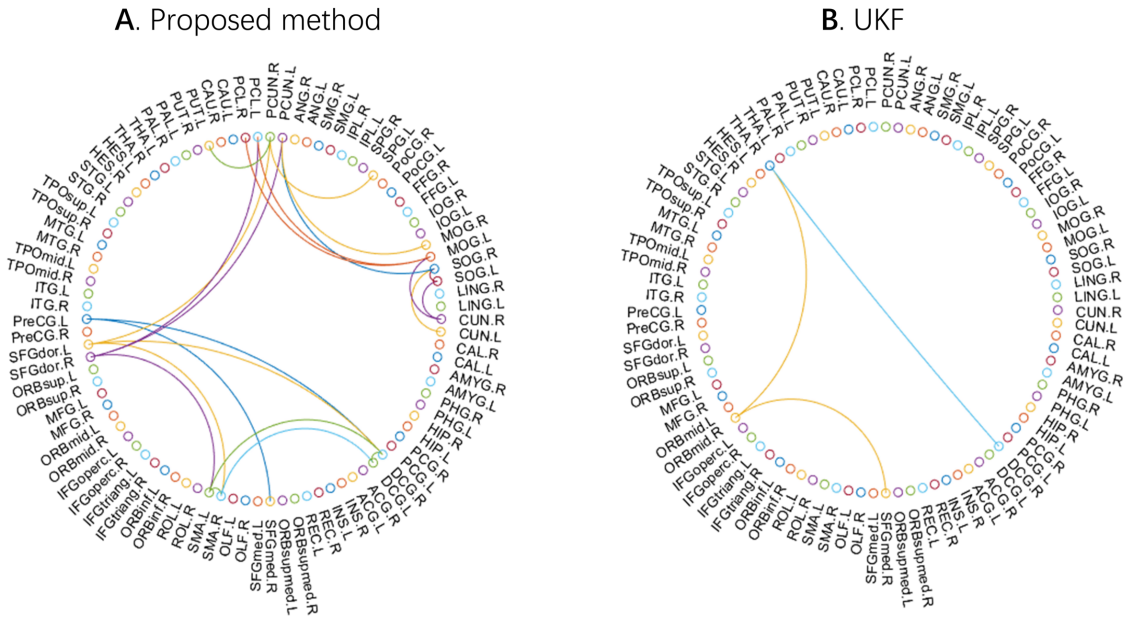


Fig.2.6. A. Sub-network is identified by the proposed method, with clusters of significantly correlated structural and functional connections (P = 0.0014). B. Fewer correlated structural and functional connections are identified by the UKF (P > 0.05). Family-wise errors of both methods are corrected by NBS with 5000 permutations.

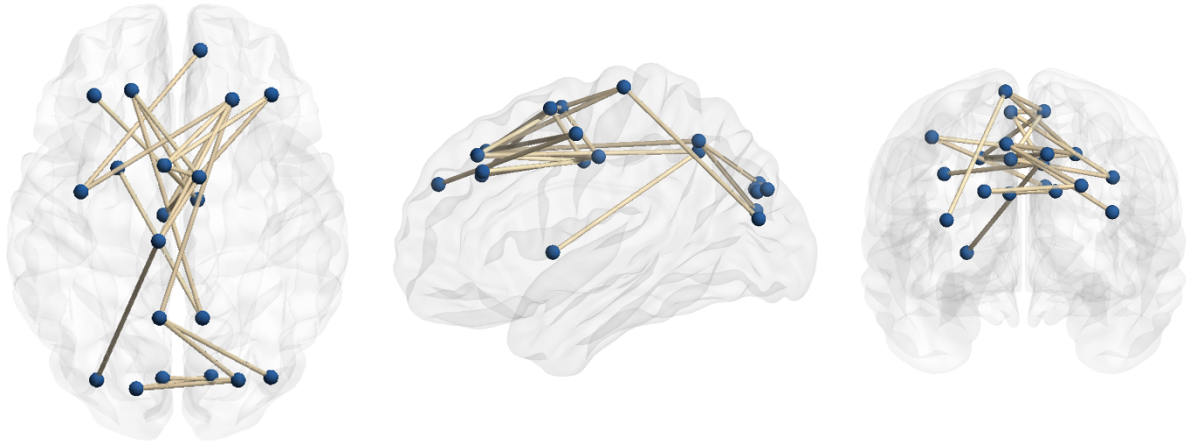


Fig.2.7. 3D Visualisation of sub-network that have a strong correlation between structural edges and functional edges identified by the proposed method.

2.4.5 Global efficiency of different tumour types

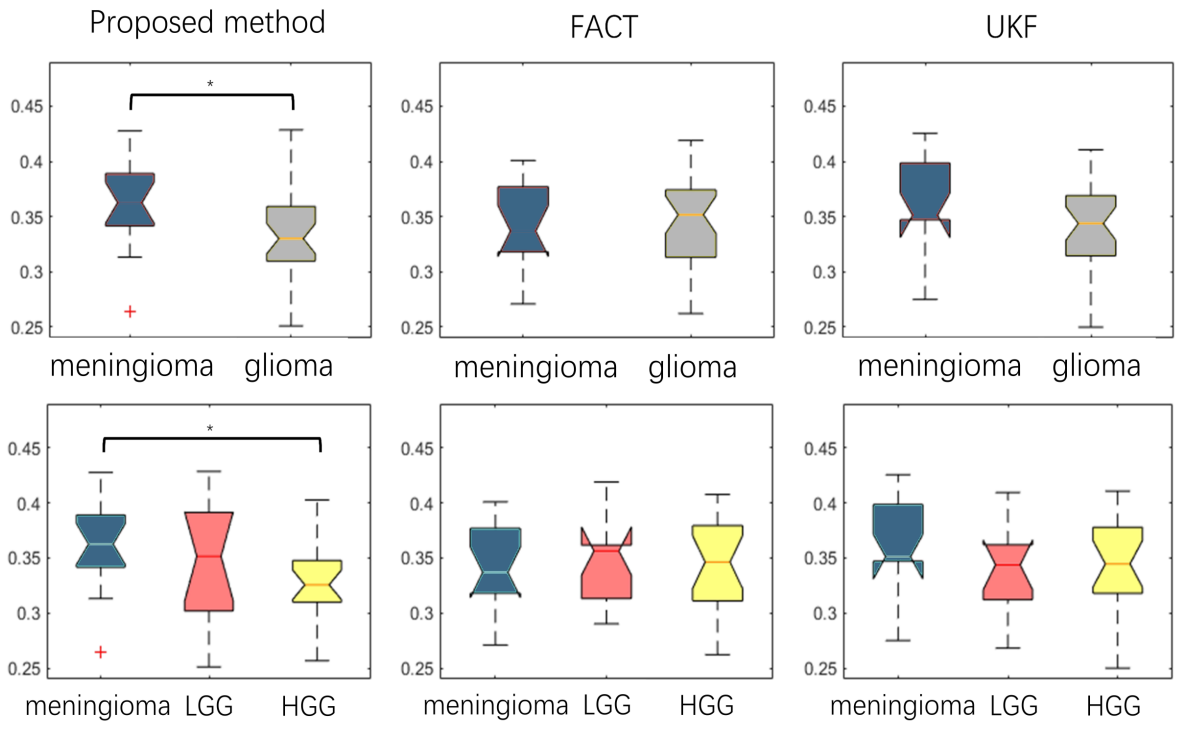


Fig.2.8. Global efficiency of the structural networks constructed using the proposed method, FACT, and UKF. Compared to glioma, meningioma patients display significantly higher global efficiency in the network constructed using the proposed approach. $*$: $P < 0.05$

The meningioma group, in general, has significantly higher global efficiency than the glioma group (P = 2.9e-4), while the baseline methods did not capture a significant difference in Fig. 2.8. Further, in a subgroup of meningioma and high-grade glioma with comparable size, meningioma patients still have significant higher global efficiency comparing to high-grade glioma group (P = 9.3e-5), while baseline methods did not show a significant difference.

2.5 Discussion

We proposed a new approach to estimate structural brain networks in tumour patients. To avoid tracking errors in brain tumour patients, we chose an indirect approach to bypass the need to track fibres in tumours that affect the brain. This approach is inspired by a similar method that estimates brain networks in traumatic brain injuries. However, the original approach cannot be directly translated for brain tumour patients due to the strong mass effect caused by the tumour. As such, we improved the approach specifically for brain tumour patients by integrating direction information into the method.

One of the advantages of our method is that it can quantitively measure the degree of disruption in structural networks. In contrast, traditional tractography will simply fail to track white matter connections in tumour-disrupted regions, leaving a zero value as the strength of the connection. Additionally, the main potential source of errors in our method is co-registration, which is mitigated with the TBSS projection step, whereas the traditional way of constructing would be prone to both co-registration errors and tractography errors.

We designed different experiments to evaluate the performance of our approach. However, since there is no ground truth for structural networks, we can only infer the robustness of our method indirectly. First, by comparing with a major tract atlas (XTRACT), we find a high correlation between major tracts and their corresponding edges. To identify the functional sensitivity of our method, we also construct a functional network for comparison. One experiment suggests our method could identify a large inter-hemispherical structural subnetwork corresponding to group-wise structural-functional connection correlation. It is

worth mentioning that those connections overlapped with the connectivity of the corpus callosum, which is found to be difficult to reveal by traditional tractography (Yendiki et al., 2014). The further experiment suggested structural networks from our methods generally have stronger coupling with functional networks. Finally, our method was found to be more sensitive to the difference in brain networks between glioma and meningioma than traditional methods, which implies its ability to detect diffuse infiltration by the glioma.

Our method has several limitations: first, the structural network from our methods is less indirect than traditional or tumour-adapted tractography methods. Hence it has limited value in applications such as surgical planning. Secondly, our method is not sensitive to connectivity disruption on the grey-white matter boundaries, which is the limitation shared with traditional tractography and TBSS.

2.6 Conclusion

This study proposes an approach to construct structural networks and estimate the connectivity, which employs an improved TBSS approach and the tractography template from healthy controls. This method is shown to be robust compared to conventional tractography, with higher functional and clinical relevance. The proposed method shows promise in aiding treatment planning and patient risk assessment.

In conclusion, this chapter validated the first hypothesis in **Chapter 1.4.2** that the approach developed from a tractography template and white matter skeleton could produce more robust and functionally relevant brain networks than traditional approaches for brain tumour patients.

Chapter 3. Structural connectome quantifies tumour invasion and predicts survival in glioblastoma patients

This chapter is based on the following publication:

Wei, Yiran et al., Structural connectome quantifies tumour invasion and predicts survival in glioblastoma patients, *Brain*, 2022; awac360, https://doi.org/10.1093/brain/awac360

3.1 Abstract

In Chapter 2, we propose a methodology to systematically identify tumour invasion by quantifying the structural connectome in glioblastoma patients. In this Chapter we applied the same methodology to larger cohorts of patients. We first recruit two independent prospective glioblastoma cohorts: the Discovery cohort with 117 patients and the Validation cohort with 42 patients. Next, we employ diffusion MRI of healthy subjects to construct tractography templates indicating white matter connection pathways between brain regions. The connectome is constructed using the method in Chapter 2. Additionally, to quantify the disrupted connectome, we calculate the deviation of the connectome strengths of patients from that of the age-matched healthy controls. We then categorise the disruption into regional disruptions based on the relative location of connectome to focal lesions. We also characterise the topological properties of the patient connectome based on the graph theory. Finally, we investigate the clinical, cognitive and prognostic significance of connectome features using the Pearson correlation test, mediation test and survival models.

Our results show that the connectome disruptions in glioblastoma patients are widespread in the normal-appearing brain beyond focal lesions, associated with lower pre-operative performance ($P < 0.001$), impaired cognitive function ($P < 0.001$), and worse survival (overall survival: hazard ratio = 1.46, $P = 0.049$; progression-free survival: hazard ratio = 1.49, $P = 0.019$). Additionally, these distant disruptions mediate the effect on topological alterations of the connectome (mediation effect: clustering coefficient: -0.017, $P < 0.001$,

characteristic path length: 0.17, $P = 0.008$). Further, the preserved connectome in the normal-appearing brain demonstrates evidence of connectivity reorganisation, where the increased neural connectivity is associated with better overall survival (log-rank $P = 0.005$).

In conclusion, our connectome approach could reveal and quantify the glioblastoma invasion distant from the focal lesion and invisible on the conventional MRI. The structural disruptions in the normal-appearing brain were associated with the topological alteration of the brain and could indicate a treatment target. Our approach promises to aid in more accurate patient stratification and more precise treatment planning.

3.2 Introduction

This chapter is designed to test the second hypothesis proposed in **Chapter 1.4.2,** including 1) structural brain networks representing white matter connectivity have the potential to characterise the early invasion of glioblastomas. 2) the disruptions of brain networks are associated with patients' cognition, performance, and survival time.

As I introduced in **Chapter 1**, glioblastoma is the most common primary malignant brain tumour in adults, characterised by diffuse infiltration into the surrounding tissue (Ricard et al., 2012). It is increasingly accepted that glioblastoma widely influences the brain structure and function beyond the focal lesion (Aerts et al., 2016; Cuddapah et al., 2014; Daniel et al., 2020; Stoecklein et al., 2020). Evidence shows that glioblastoma can induce profound reorganisation of neural connectivity (Aerts et al., 2016; Yu et al., 2020), while neuronal activity can promote tumour progression (Venkataramani et al., 2019). This bidirectional interaction underscores the promise of characterising neural connectivity for a better understanding of glioblastoma invasion, which may facilitate more accurate patient stratification for personalised management.

As I discussed in **Section 1.2.3**, Diffusion MRI (dMRI) is a method to estimate the structural connectivity of the brain. It is more sensitive to detecting occult tumour invasion than conventional T1-weighted and FLAIR images (Price et al., 2003). Evidence shows that dMRI can indicate the tissue signature of glioma (Price et al., 2004), offering value to evaluate invasiveness, detect peritumoral invasion (Li, Wang, Yan, Piper, et al., 2019), indicate subventricular zone involvement (van Dijken et al., 2017), and predict molecular phenotypes (Price et al., 2017). These studies, however, have focused on the *focal* tumour, instead of the *systematic* disturbance of the brain.

In **Section 1.3**, I introduced network neurosciences as a model representing structural connectivity as a complex network, namely structural connectome (Bullmore & Sporns, 2009; Rubinov & Sporns, 2010). This approach models brain regions as nodes while the white matter connections among brain regions are as edges. Graph theoretical analysis of the derived structural networks shows to characterise various neurological and psychiatric

disorders (Crossley et al., 2014; Raj et al., 2015; Sun et al., 2015). Moreover, studies suggest that brain tumours may alter the connectome topology while brain networks correspondingly demonstrate robustness and reorganisation (Aerts et al., 2016; Aerts et al., 2020; Kinno et al., 2014; Liu et al., 2020). Recent evidence shows that the topological features derived from the connectome may predict tumour location frequency in glioma patients (Mandal et al., 2020) and appear to predict patient survival (Liu et al., 2016). However, it remains largely unknown whether the connectome disruption could be quantified for patient stratification. Of particular significance is whether the robustness of the connectome could impact patient outcomes.

The purpose of this study was to characterise the disruption of the structural connectome in glioblastoma patients and investigate the clinical significance. We hypothesised that glioblastoma could induce both focal and global disturbance to the structural connectome, leading to topological alteration of the brain and impacting patient outcomes. We tested this hypothesis in two prospective glioblastoma cohorts. Firstly, we constructed the structural networks using the dMRI from glioblastoma patients and healthy controls. Secondly, we quantified the focal and distant disrupted connectome separately from each patient. Thirdly, we calculated the disruption indices and topological features and examined their significance in survival models. Lastly, we modelled the alteration of the preserved connectivity after removing the disrupted connectome and investigated its significance on patient survival. The results revealed widespread disruptions of the structural connectome, which could lead to topological alterations and show prognostic value in glioblastoma patients.

3.3 Methods

3.3.1 Subjects

Patients with a radiological diagnosis of *de novo* supratentorial glioblastoma were prospectively recruited for resection (Discovery: July 2010 - August 2015; Validation: July 2017 - October 2019) by the multidisciplinary team (MDT) in Cambridge University Hospitals. This study were approved by the local institutional review board of Cambridge University Hospital. For MRI data collection, informed written consent was obtained from all

patients. For both cohorts, patients were consecutively recruited following identical inclusion and exclusion criteria, with data prospectively collected.

Inclusion Criteria: radiological diagnosis of *de novo* glioblastoma; Age 18 - 75; likely to be suitable for radiotherapy with concomitant and adjuvant temozolomide (Fig. 3.1).

Exclusion Criteria: unsuitable for a contrast-enhanced MRI; poor image quality; pregnancy or plan for pregnancy; previous history of cranial surgery or cranial radiotherapy/chemotherapy; allergic to aminolaevulinic acid or suffering from porphyria; post-operative non-glioblastoma histology.

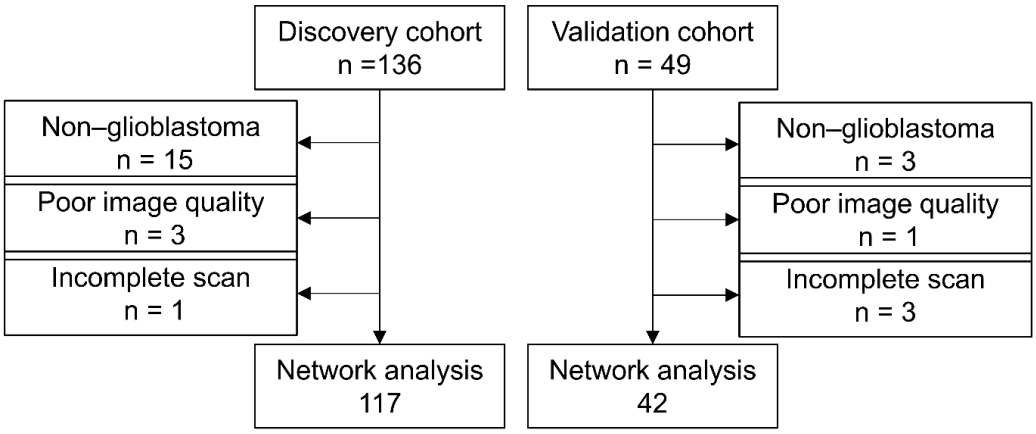


Fig 3.1. Data inclusion follow-up for the Discovery and Validation cohort.

All patients underwent pre-operative 3D MPRAGE (pre-contrast [T1] and post-contrast [T1C]), T2-weighted FLAIR, and dMRI sequences (Table 3.1). Patient pre-operative cognitive performance was tested using the Mini-Mental State Examination (MMSE), dichotomised as <27 or >=27 as reported (Gorlia et al., 2008).

Table 3.1 MRI acquisition sequences for the Discovery and Validation cohort

	Discovery	Validation
T1-weighted imaging		
Scanner	Siemens	GE
Sequence	MPRAGE	BRAVO
Field Strength (Tesla)	3	3
Flip Angle (degree)	9	12
Resolution X, Y, Z (mm)	1.0 × 1.0 × 1.0	1.0 × 1.0 × 1.0
FOV X × Y (mm)	256 × 240	256 × 256
Slice gap (mm)	0	0
TR (ms)	2300	8.16
TE (ms)	2.98	3.18
Inversion time (ms)	900	450
T2-weighted imaging		
Flip Angle (degree)	150	111
Resolution X, Y, Z (mm)	0.69 × 0.69 × 5	0.23 × 0.23 × 6
FOV X, Y (mm)	220 × 165	240 × 240
Slice gap (mm)	0.5	1
TR (ms)	4840	4942
TE (ms)	114	87.6
T2-weighted fluid-attenuated inversion recovery (FLAIR)		
Flip Angle (degree)	150	111
Resolution X, Y, Z (mm)	0.78 × 0.78 × 4.0	0.47 × 0.47 × 6.0
FOV X, Y (mm)	250 × 200	240 × 240
Slice gap (mm)	1	0
TR (ms)	7840	8000
TE (ms)	95	124.6
Inversion time (ms)	2500	2129
Diffusion-weighted imaging		
Flip Angle (degree)	90	90
Resolution X, Y, Z (mm)	2.0 × 2.0 × 2.0	0.93 × 0.93 × 3.0
FOV X, Y (mm)	192 × 192	256 × 128
Slice gap (mm)	0	3
TR (ms)	8300	8000
TE (ms)	98	87.4
B value	350, 650, 1000, 1300, 1600	1000
Gradient direction	12 for each b value	64

A control cohort with age-matched healthy controls used for generating control brain networks was obtained from the IXI dataset (https://brain-development.org/ixi-dataset/). The IXI dataset includes T1, T2, PD, dMRI, and MRA data for some or all of the 619 healthy subjects.

For the present study, 117 age-matched healthy controls (mean age 59.9 ± 10.1years, median age 62.6 years, range 20.9-76.0 years, 63 males) were selected from the IXI dataset. Therefore, each patient in the Discovery cohort was matched with a corresponding healthy

control with an age difference < 2 years. No significant age difference was found between the Discovery and healthy control cohorts (two-sample t-test, $P = 0.605$). The dMRI scans of the healthy controls were acquired in two hospitals using two Scanners (Table 3.2)

Table 3.2 MRI acquisition sequences for the IXI dataset

	Hammersmith Hospital	**Guy's Hospital**
Scanner	Philips Medical Systems Intera	Philips Medical Systems Gyroscan Intera
Field Strength (Tesla)	3	1.5
Flip Angle (degree)	90	90
Resolution X, Y, Z (mm)	1.75, 1.75, 2.00	1.75, 1.75, 2.35
FOV X, Y (mm)	112, 110	112, 110
TR (ms)	11894.4	9054
TE (ms)	51	80
B value	1000	1000
Gradient direction	15	15

We also included the high angular resolution dMRI from the Alzheimer's disease Neuroimaging Initiative (ADNI, http://adni.loni.usc.edu/) for constructing an unbiased template of white matter (WM) connection with high spatial resolution. Ten elderly healthy subjects were selected from the ADNI-CN (healthy control) research group (mean age 60.9 ± 1.5 years, median age 60.2 years, range 58.4 - 62.1 years, three males). No significant age difference was found between the control and Discovery cohorts (Two-sample t-test $P = 0.712$). The diffusion MRI protocol of the healthy controls is in Table 3.3

Table 3.3 MRI acquisition sequences for the ADNI

Scanner	SIEMENS
Field Strength (Tesla)	3
Flip Angle (degree)	90
Resolution X, Y, Z (mm)	2,2,2
FOV X, Y, Z (mm)	115, 115, 80
Pulse Sequence	EP
TR (ms)	7200
TE (ms)	56
B value	1000
Gradient direction	54

3.3.2 Treatment

All patients underwent maximal safe surgery using 5-aminolevulinic acid fluorescence (5-ALA, Medac, Stirling, UK) and neuro-navigation (StealthStation, Medtronic, Fridley, MN, USA). For maximal safe resection in both study cohorts, where appropriate, other adjuvants, including awake surgery, cortical and subcortical mapping, and intraoperative electrophysiology, were also applied. According to the post-operative MRI, within 72 hours, the extent of resection was assessed as complete or partial resection of enhancing tumour or biopsy. Adjuvant therapy was determined by the MDT as standard based on the patient post-operative status. All patients were followed up according to the response assessment in neuro-oncology (RANO) criteria. Overall survival (OS) and progression-free survival (PFS) were used as endpoints.

3.3.3 Tumour segmentation

All anatomical MRI (T1, T2, and FLAIR) were co-registered to T1C images with an affine transformation using the linear image registration tool (FLIRT) function in the FMRIB Software Library (FSL) (Jenkinson et al., 2002). To segment the tumour, we applied a multi-scale 3D Deep Convolutional Neural Network (Kamnitsas et al., 2016), implemented in the Cancer Imaging Phenomics Toolkit (CaPTk, https://cbica.github.io/CaPTk/index.html). The manual correction was performed using 3D slicer v4.6.2 (https://www.slicer.org/) by a neurosurgeon and a researcher after an initial training period and reviewed by an experienced neuroradiologist. The final consensus was achieved to ensure inter-rater reliability.

3.3.4 Quantifying the brain connectome

Chapter 1.2.3 discussed the limitaiton of applyCing tractography to brain tumour patients. While Chapter 2 proposed a method to bypass the bias of performing tractography on the lesioned brain. To recap, the complete pipeline in Chapter 2 includes the following steps: **1)** constructing a group-based tract template (**Fig. 3.2A**); **2)** producing individualised skeletonised FA maps (**Fig. 3.2B**); **3)** combining the template with the FA skeleton maps to

estimate the connectome strength in both patients and controls (**Fig. 3.2C & D**); **4)** In this Chapter, an additional step is added: identifying the significantly disrupted connectome in patients **(Fig. 3.2E-G)**.

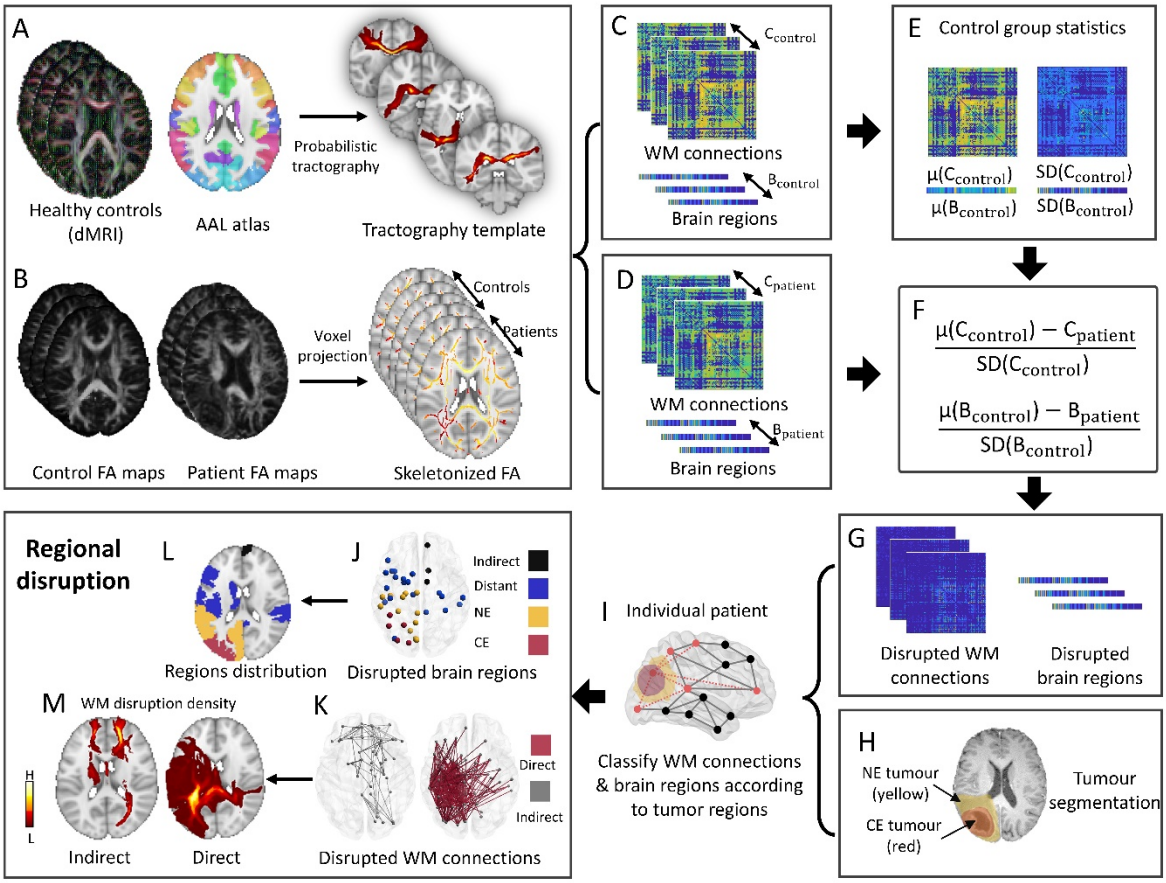


Fig. 3.2. Study design. (**A**) Probabilistic tractography is performed on the high-resolution dMRI of ten healthy controls to generate a template for the white matter connections among the 90 regions on the AAL atlas. (**B**) Skeletonised fractional anisotropy (FA) maps are generated from both patients and age-matched healthy controls to estimate the WM connection strength using an improved voxel projection procedure based on TBSS. (**C-D**) The strengths of WM connections are derived in healthy controls and patients by combining WM connection templates and skeletonised FA. The strengths of brain regions are calculated by aggregating the strengths of linking WM connections. (**E-G**) By comparing patients to controls, the disrupted connectome in patients is identified as the WM connection ($C_{patient}$) or brain region ($B_{patient}$) with a strength of over 2SD (95% confidence) lower than the mean strength of the control group (($\mu(C_{control})$ or $\mu(B_{control})$). The disruption indices of

WM connections and brain regions are calculated by averaging the disruption matrices/vectors. (**H**) The lesion is segmented as contrast-enhancing (CE, red) and non-enhancing (NE, yellow) tumours. (**I**-**K**) The brain region disruptions are classified as CE, NE, Distant, and Indirect disruptions. The WM connection disruption is classified as Direct and Indirect disruptions. (**L**) Categorical disrupted brain regions are mapped to the standard space. (**M**) Disrupted WM connections are mapped to the standard space producing a disruption density map. **AAL**: automated anatomical labelling, **TBSS**: Tract-Based Spatial Statistics, **WM**: white matter, **FA**: fractional anisotropy.

3.3.4.1 Constructing a template of white matter connections

An unbiased WM connection template was generated by following the same methods as **Chapter 2.3.2.1.**

3.3.4.2 Generating skeletonised FA maps

The individualised FA skeletons representing the centre integrity of white matter tracts in subjects are generated by following the same methods as **Chapter 2.3.2.2**

3.3.4.3 Estimating strengths of white matter connections and brain regions

We calculated the strength B_i for region i, by aggregating the connectivity strength of the WM connection C_{ij} connected to this region by following the same methods as **Chapter 2.3.2.3.**

3.3.4.4 Identification of significantly disrupted connectome

In this Chapter, we developed an additional steps to identify significantly disrupted connectome: we first calculated the mean strength and SD of each WM connection across all healthy controls, which was compared to individual patients (**Fig. 3.2G**). We defined the

significantly decreased connectome in patients as those with a strength of over 2SD (95% confidence) lower than the mean strength of the whole control group.

3.3.5 Estimating connectome disruptions

We calculated the patient-wise global disruption index by averaging the disruption of WM connections and brain regions, respectively. To address intra-tumour heterogeneity, we segmented the lesion as contrast-enhancing (CE, the entire area within T1 contrast-enhancing rim) and peritumoral non-enhancing (NE, the hyper-intensities surrounding CE on FLAIR) subregions (**Fig. 3.2H & I**). Based on the segmented tumour, we categorised the disrupted WM connections and brain regions as below (**Fig. 3.2J & K**):

3.3.5.1 Disrupted WM connections

1) **Direct disruption:** directly disrupted by tumour, travelling across the contrasting enhancing or non-enhancing tumour.
2) **Indirect disruption:** disrupted without crossing the lesion.

3.3.5.2 Disrupted brain regions

1) **Tumour disrupted regions:** disrupted regions within the lesion, further categorised into **CE** or **NE disrupted regions,** according to the overlap with tumour subregions.
2) **Distant disrupted regions:** disrupted regions within the normal-appearing brain and connected to the lesion via WM connections.
3) **Indirect disrupted regions:** disrupted regions without any connection to the lesion.

Finally, we calculated the regional disruption index as the average of each category.

3.3.6 Group distribution of tumour disruption

To generate a tumour frequency map, we nonlinearly transformed all tumour masks from individual patients to the standard space using ANTs, with voxel-wise tumour distribution density normalised at the group level. Regional disrupted WM connections and brain regions

are mapped to the standard space for visualisation (**Fig. 3.2L & M**). We also quantified the disruption probability of brain regions and major tracts among patients. For tracts, we mapped the WM connections to the 42 anatomical tracts constructed from the 1,000 healthy subjects available in the XTRACT toolbox of FSL. The disruption probability for each brain region or tract was calculated as the percentage of patients with this brain region or tract disrupted. We also calculated the proportion of disrupted connectomes out of all the patients.

3.3.7 Topological features of the connectome

We calculated the two most commonly used topological features for each patient using the Brain Connectivity Toolbox (Rubinov & Sporns, 2010): characteristic path length and clustering coefficient. Briefly, the clustering coefficient measures the probability of two direct topological neighbours of a specific brain region is connected. The characteristic path length measures the average shortest path length of the network (**Table 3.4**) (Watts & Strogatz, 1998). We filtered the connectome with a population-consistency-based strength threshold to reduce the noise in feature calculation (Roberts et al., 2017).

Table 3.4 Definition of topological features

Feature	Formula	Mathematical meaning	Interpretation
Clustering coefficient (Cl)	$Cl = \frac{1}{N}\sum_{i \in N} \frac{2t_i}{k_i(k_i - 1)}$, where Cl is the average clustering coefficient in the networks, ki is the degree/strength of node i, and ti is the number of closed triangles attached to i. N is the number of nodes.	The probability that two nodes directly connected to a third node separately are also linked to each other	A measure of functional segregation or specialisation.
Characteristic path length (Lp)	$Lp = \frac{1}{N(N-1)}\sum_{j \neq i} l_{ij}$, where L is the average shortest path length between nodes in the network, lij is the shortest path length from node j to node i.	the average shortest path length between all possible pairs of nodes in a network.	A measure of global efficiency and network integration.
In brain networks, the node refers to brain regions and the edge refers to white matter connections between brain regions			

3.3.8 Preserved connectivity of disrupted distant regions

By removing the disrupted WM connections, we investigated the preserved connections, defined as the remaining WM connections to the disrupted Distant regions. Through pairwise comparison between patients and age-matched controls, we categorised patients into two subgroups with overall increased or decreased connectivity respectively, according to the summed strength of the preserved connectivities.

3.3.9 Statistical analysis

All analyses were performed in RStudio v3.2.3 and MATLAB 2019b. The Benjamini-Hochberg procedure (BH-FDR) correction was performed for all multiple comparison tests. The hypothesis of no effect was rejected at a two-sided level of 0.05. The difference between global/regional disruptions and topological features of patient cohorts/subgroups were compared using the two-sample t-test. Pearson correlation was used to test the correlations between disruption indices, MMSE score, tumour volume and topological features. Multiple regression was used to identify significant regional disruptions contributing to topological changes. The mediation model was used to test whether the above-identified contributor mediated the effect of the lesion on brain topology.

We performed survival analysis to evaluate disruption indices and topological features using OS and PFS. Patients alive at the last known follow-up were censored. Kaplan-Meier survival curves were compared using a log-rank test, based on disruption indices and topological features dichotomised by either median or the optimal cut-off defined using the maximally selected rank statistics in the R package 'Survminer', (H. Lin & Zelterman, 2002) whichever was more significant.

In addition to the univariate Cox proportional hazards model, we conducted a multivariate Cox proportional hazards model accounting for all relevant clinical covariates, including O-6-methylguanine-DNA methyltransferase (MGMT) methylation status, isocitrate

dehydrogenase-1 (IDH-1) mutation, sex, age, the extent of resection, adjuvant therapy, tumour volume. We also included two tumour location features from the Visually Accessible Rembrandt Images (VASARI) feature set describing the involvement of eloquent cortex and deep white matter ("Visually Accessible Rembrandt Images (VASARI) feature set for human glioma" 2014) to account for the effects of tumour cortical/subcortical brain regions.

We used the receiver operating characteristic (ROC) curves to evaluate the accuracy in predicting OS. We fit a generalised linear model and calculated the AUC of the ROC curve. The model included the significant disruption indices and topological features from the univariate Cox proportional hazards models.

3.4 Results

3.4.1 Subject characteristics

For the Discovery cohort, we recruited 136 patients for pre-operative MRI scanning. After excluding 19 patients according to the trial exclusion criteria, we finally included 117 of 136 (86.0 %) patients (mean age 59 years, range 22-75 years, 89 males) for analysis. Six patients (5.1 %) were lost to follow-up. The median overall survival (OS) was 392 (range 34-1932) days. The median progression-free survival (PFS) was 275 (range 13-1393) days.

For the Validation cohort, 49 patients were initially recruited, and 42 patients were finally included according to the trial exclusion criteria (mean age 59 years, range 28-75 years, 30 males). Ten patients (23.8 %) were alive or lost to follow-up. The median OS was 335 (range 55- 962) days. The median PFS was 246 (range 21-805) days. Two study cohorts showed no significant differences in clinical variables (**Table 3.5**).

We included 117 healthy age-matched subjects (mean age 59.9 years, 78 males) from the IXI datasets as healthy controls. In addition, we included 10 healthy subjects (mean age 60.9 years, 5 males) from the ADNI for the tractography template. All cohorts showed no significant difference in age.

Table 3.5. Summary of the patient cohorts

Variable	Patient Number		*P* value
	Discovery	Validation	
Age at diagnosis			
<60	42	18	0.425
≥60	75	24	
Sex			
Male	89	30	0.236
Female	28	12	
The extent of resection (of enhancing tumour)			
Complete	77	32	0.572
Partial	32	6	
Biopsy	8	4	
MGMT-methylation status [a]			
Methylated	49	21	0.363
Unmethylated	68	21	
IDH-1 mutation status			
Mutant	7	1	0.360
Wild type	110	41	
Pre-operative Tumour volumes (cm^3) [b]			
Contrast-enhancing	44.7 ± 28.8	45.2 ± 29.4	0.841
Non-enhancing	50.3 ± 36.2	46.4 ± 32.6	0.652

(a): MGMT-methylation status unavailable for 4 patients in the Discovery cohort; **(b)**: mean ± SD of original data. MGMT: O-6-methylguanine-DNA methyltransferase; IDH-1: Isocitrate dehydrogenase 1.

3.4.2 Global disrupted connectome demonstrates the clinical significance

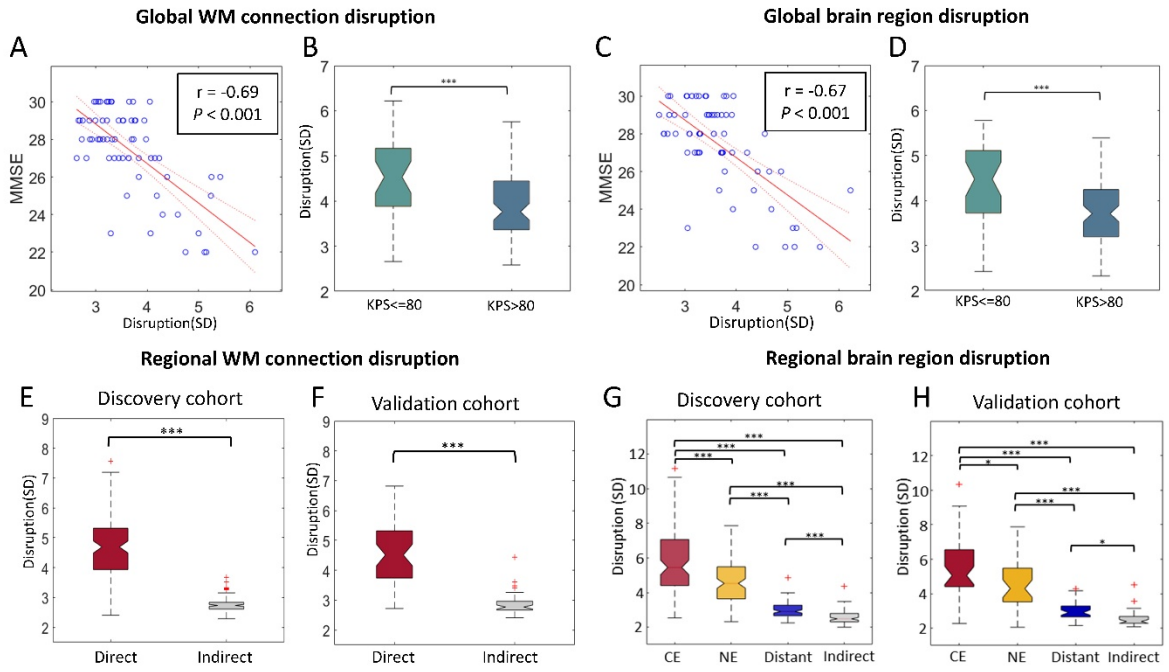


Fig. 3.3. The clinical significance of disruption indices. (A, C) The global disruption indices of WM connections and brain regions are both negatively correlated with the MMSE score. **(B, D)** Higher disruption is associated with worse KPS. (**E, F**) In both Discovery and Validation cohorts, Direct connection disruption is higher than Indirect disruption. (**G, H**) Disruptions of tumour regions (CE, NE) are more significantly disrupted than the normal-appearing brain (Distant, Indirect). **WM**: white matter. **TBSS**: tract-based spatial statistics; **MMSE**: Mini-Mental State Examination; **KPS**: Karnofsky Performance Status. *P* value significant codes: $P < 0.001$ ***.

We observed that the global disruption of WM connections (Pearson: r = -0.67, $P < 0.001$; Spearman: rho=-0.48, $P < 0.001$, **Fig. 3.3A**) and brain regions (Pearson: r = -0.69, $P < 0.001$; Spearman: rho = -0.52, $P < 0.001$, **Fig. 3.3C**) were both negatively correlated with the MMSE score. To exclude the potential effect of age on cognition, a linear regression model

was used to predict the MMSE score based on the Disruption indices adjusting for age (MMSE ~ Disruption indices + Age). The results show that only the disruption indices were significant (Age: $P = 0.296$, Global WM disruption: $P < 0.001$; Age: $P = 0.425$, Global brain region disruption: $P < 0.001$). The correlation test between age and MMSE score showed no significance (Pearson: r = -0.17, $P = 0.156$; Spearman: rho= -0.17, $P = 0.176$).

We further compared the patient subgroups stratified by the KPS score of 80 as reported (Chaichana et al., 2010). We found that a worse KPS score was associated with higher disruptions of both brain regions and WM connections (both $P < 0.001$, **Fig. 3.3B & D**). We also found significant negative correlations between the KPS score and the global disruption indices (WM disruption: Pearson, r = -0.51, $P < 0.001$; Spearman: rho=-0.41, $P < 0.001$, Brain region disruption: Pearson, r = -0.49, $P < 0.001$; Spearman: rho=-0.31, $P < 0.001$). These results indicate that the stratified patient subgroups may have different global disruption indices.

Finally, we trained logistic regression models to predict the better or worse KPS as stratified above. The baseline model including two preoperatively available variables: age and tumour volume, achieved an AUC of 0.79 (CI: 0.68-0.91). Adding the global disruption indices into the model improved the AUC to 0.86 (CI: 0.77-0.94, Fig. **3.**3A). The out-of-sample prediction on the Validation cohort showed improved performance (AUC = 0.71, CI: 0.53-0.89) than the baseline (AUC = 0.60, CI: 0.43-0.78, **Fig. 3.4B**).

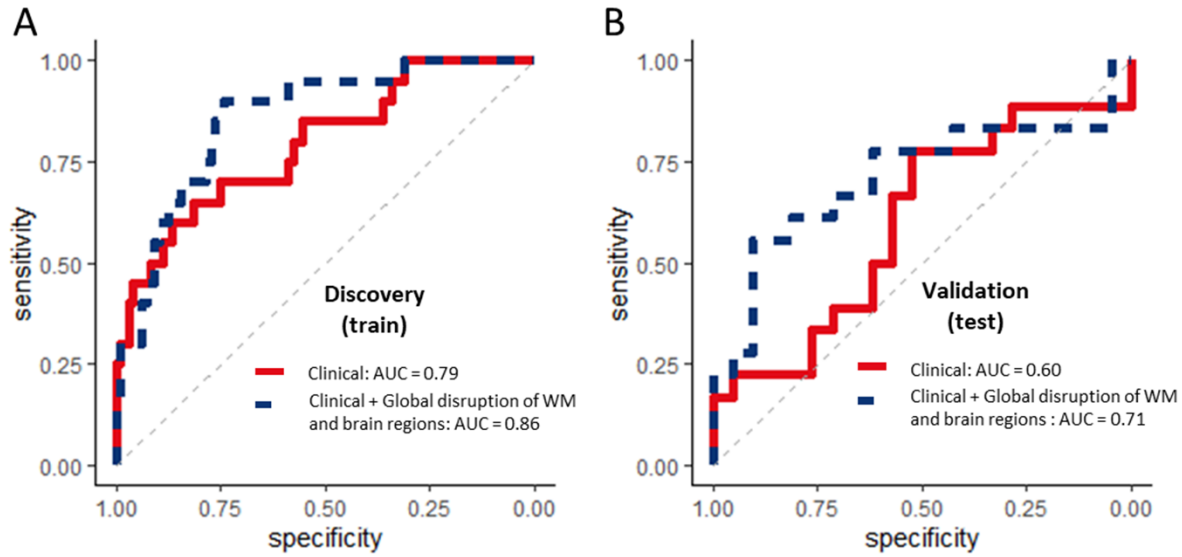


Fig. 3.4. Predicting KPS cut-off with a logistic model. (A) The logistic models trained on clinical data and clinical data (Age, tumour volume) with global disruption showed a slight increase in the AUC from 0.79 to 0.86 for the Discovery cohort. (**B**) The out-of-sample prediction on the Validation cohort showed a larger increase in the AUC from 0.60 to 0.71.

To rigorously assess the reproducibility of WM connection strength estimation, we compared the strengths of a cerebellar tract (middle cerebellar peduncle, MCP) that is not affected by the supratentorial tumours in our cohorts. No significant difference was found between controls and patients, **Fig. 3.5**).

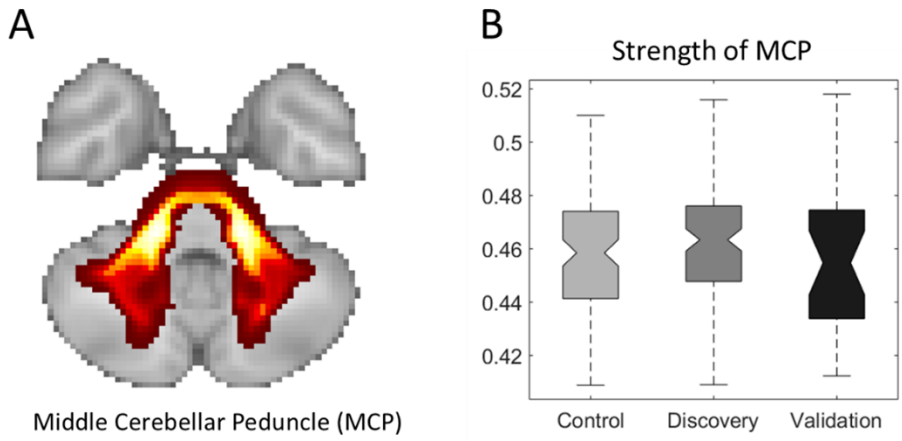


Fig. 3.5. White matter connection strengths of the middle cerebellar peduncle across three cohorts. (A) The middle cerebellar peduncle (MCP) is expected unaffected by the supratentorial tumour in the two study cohorts. **(B)** Patient and control cohorts show no significant difference in the MCP connection strength (Two-sample T test *P* value: Control vs Discovery = 0.063, Control vs Validation = 0.370; Two-sample F test *P* value: Control vs Discovery = 0.648, Control vs Validation = 0.757).

3.4.3 Regional disrupted connectome characteristics

3.4.3.1 Tumour regions are more significantly disrupted than distant regions

Table 3.6. Comparison of the two patient cohorts

	Discovery		Validation		
Category	Mean ± SD	95%CI	Mean ± SD	95%CI	*P* value
White matter connection disruption					
Direct	4.77 ± 1.56	2.60-7.43	4.95 ± 1.50	2.92-8.00	0.518
Indirect	2.59 ± 0.39	2.51-2.67	2.54 ± 0.53	2.43-2.65	0.520
Brain region disruption					
CE	5.83 ± 2.00	2.80-8.74	5.51 ± 1.80	2.28-7.45	0.363
NE	4.67 ± 1.33	2.77-7.43	4.54 ± 1.53	2.30-7.45	0.603
Distant	2.90 ± 0.71	2.30-3.83	3.08 ± 0.76	2.33-4.33	0.169
Indirect	2.56 ± 0.39	2.15-3.37	2.62 ± 0.55	2.17-4.05	0.447

The two study cohorts showed no significant difference in disruption indices (**Table 3.6**). In comparing disruptions of WM connections, we observed significantly higher Direct disruption (4.77 ± 1.56) than Indirect disruption (2.59 ± 0.39, $P < 0.001$, **Fig. 3.3E & F, Table 3.3)**. Similarly for brain regions, focal tumours (CE: 5.83 ± 2.00; NE: 4.67 ± 1.33) were more significantly disrupted than the normal-appearing brain (Distant: 2.90 ± 0.71, Indirect: 2.56 ± 0.39, each $P <0.001$, **Fig. 3.3G & H**). The Validation cohort showed similar disruption patterns. These results correspond to our understanding of tumour invasion and support the robustness of the regional disruption indices.

3.4.3.2 The regional disruptions are correlated with focal tumour volume

Pearson correlation tests showed that the WM connection disruptions in the tumour (Direct) and normal-appearing brain (Indirect) were positively correlated ($r = 0.44$, $P <0.001$). Similarly, the disruption of Distant regions was positively correlated with that of tumour regions (Distant vs. CE: $r = 0.43$, $P < 0.001$; Distant vs. NE: $r = 0.34$, $P = 0.028$, **Table 3.7**). Further, the tumour volume (measured by CE tumour) was positively correlated with the disruptions of both Direct connections ($r = 0.52$, $P < 0.001$) and Distant regions ($r = 0.33$, $P < 0.001$, **Table 3.8**). Collectively, these data indicate that a larger focal tumour is associated with higher connectome disruption throughout the brain.

Table 3.7. Pearson correlations of disruption indices

White matter connection disruption						
	Discovery			Validation		
Category	r (*P*) Indirect			r (*P*) Indirect		
Direct	0.44 (<0.001)			0.51 (<0.001)		
Brain region disruption						
	Discovery			Validation		
Category	r (*P*) NE	r (*P*) Distant	r (*P*) Indirect	r (*P*) NE	r (*P*) Distant	r (*P*) Indirect
CE	0.41 (<0.001)	0.43 (<0.001)	0.21 (0.156)	0.63 (<0.001)	0.54 (0.002)	0.39 (0.094)
NE	-	0.34 (0.028)	0.26 (0.056)	-	0.54 (0.002)	0.42 (0.056)
Distant	-	-	0.11 (0.237)	-	-	0.22 (0.176)

P value adjusted by FDR

Table 3.8. Pearson correlations between connectome disruption and tumour volume

	Discovery		Validation	
	Pearson r	***P***	**Pearson r**	***P***
Direct connections	0.52	<0.001	0.72	<0.001
Indirect connections	0.07	0.453	0.09	0.563
CE regions	0.48	<0.001	0.62	<0.001
NE regions	0.20	0.041	0.52	0.002
Distant regions	0.33	<0.001	0.39	0.013
Indirect regions	-0.06	0.489	0.19	0.234

P value adjusted by FDR

3.4.3.3 The normal-appearing brain shows widespread disruption

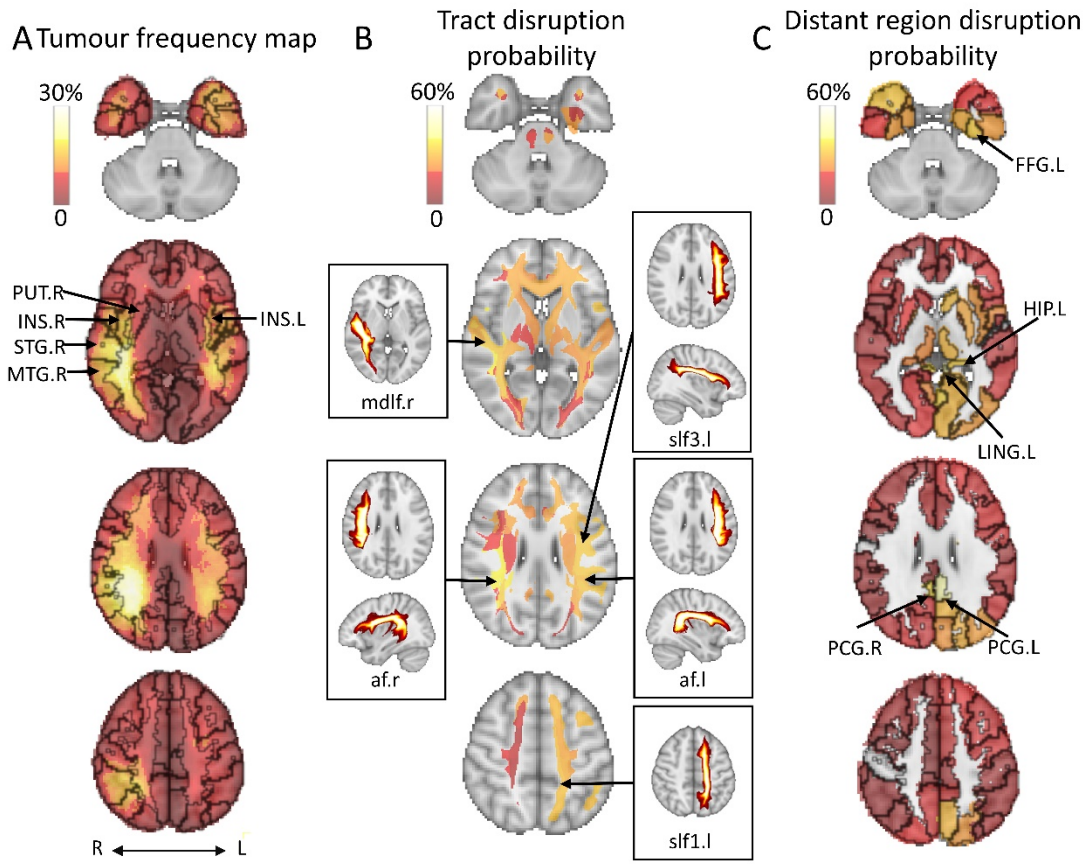


Fig. 3.6 Tumour density and disrupted anatomical structures. (**A**) Tumour frequency maps are generated using tumour segmentation masks. The top five disrupted focal brain regions include the right superior temporal gyrus (STG.R), right middle temporal gyrus (MTG.R), right insula (INS.R), left insula (INS.L), and right lenticular nucleus, putamen (PUT.R). (**B**) The top five disrupted anatomical tracts and their maximum intensity projection: right arcuate fasciculus (af.r), right middle longitudinal fasciculus (mdlf.r), left superior longitudinal fasciculus 3 (slf3.l), left arcuate fasciculus (af.l), left superior longitudinal fasciculus 1 (slf1.l). (**C**) The top five disrupted Distant regions include the left posterior cingulate gyrus (PCG.L), right posterior cingulate gyrus (PCG.R), left lingual gyrus (LING.L), left fusiform gyrus (FFG.L), and left hippocampus. L/l: left; R/r: right. WM: white matter. **MMSE**: Mini-Mental State Examination; **KPS**: Karnofsky Performance Status. *P* value significant codes: $P < 0.001$ ***, $P < 0.01$ **, $P < 0.05$ *.

Table 3.9. Proportions of the disrupted connectome

White matter connection disruptions								
	Discovery				Validation			
Category	Mean ± SD	*P* (vs. Indirect)			Mean ± SD	*P* (vs. Indirect)		
Direct	20.4 ± 9.6%	<0.001			20.7 ± 10.1%	<0.001		
Indirect	11.5 ± 6.7%	-			13.2 ± 6.6%	-		
Brain region disruptions								
	Discovery				Validation			
Category	Mean ± SD	*P* (vs. NE)	*P* (vs. Distant)	*P* (vs. Indirect)	Mean ± SD	*P* (vs. NE)	*P* (vs. Distant)	*P* (vs. Indirect)
CE	5.8 ± 5.1%	<0.001	<0.001	<0.001	5.9 ± 4.0%	0.341	<0.001	<0.001
NE	11.3 ± 7.2%	-	<0.001	<0.001	8.6 ± 7.9%	-	0.007	<0.001
Distant	16.8 ± 12.0%	-	-	<0.001	16.3 ± 9.9%	-	-	<0.001
Indirect	3.2 ± 3.0%	-	-	-	2.1% ± 2.3%	-	-	-

P value adjusted by FDR

Table 3.10. Disruption probabilities of the XTRACT tracts

Index	Tracts	Disruption probability
1	ac	0.20
2	af.l	0.32
3	af.r	0.40
4	ar.l	0.23
5	ar.r	0.27
6	atr.l	0.27
7	atr.r	0.23
8	cbd.l	0.28
9	cbd.r	0.23
10	cbp.l	0.20
11	cbp.r	0.20
12	cbt.l	0.24
13	cbt.r	0.21
14	cst.l	0.25
15	cst.r	0.18
16	fa.l	0.29
17	fa.r	0.26
18	fma	-
19	fmi	0.27
20	fx.l	-
21	fx.r	-
22	ifo.l	0.28
23	ifo.r	0.30
24	ilf.l	-
25	ilf.r	-
26	mcp	-
27	mdlf.l	0.27
28	mdlf.r	0.38
29	or.l	0.23
30	or.r	0.29
31	slf1.l	0.30
32	slf1.r	-
33	slf2.l	0.30
34	slf2.r	-
35	slf3.l	0.32
36	slf3.r	-
37	str.l	0.22
38	str.r	0.17
39	uf.l	0.29
40	uf.r	0.29
41	vof.l	-
42	vof.r	-

P value adjusted by FDR. '-' denotes the tracts that are not significantly disrupted.

We calculated the proportion of disrupted regions out of all brain regions. Noteworthy, in the group analysis, a higher proportion of Distant regions (16.8 ± 12.0%) was identified than focal lesions (CE: 5.8 ± 5.1%, $P < 0.001$), recapitulated by the Validation cohort (**Table 3.9**), indicating that the normal-appearing brain was widely disrupted.

At the group level, the average disruption probability of Distant regions was higher (17.2 ± 9.0%) than focal lesion (CE: 11.8 ± 6.8%, $P < 0.001$), possibly due to the more extensive coverage of the Distant regions. This finding further confirmed that the disruption of brain regions was widespread beyond the lesion.

We further compared the tumour frequency map (**Fig. 3.6A**) with the distribution probability map of brain regions and tracts. Notably, the top five tracts most likely disrupted were mainly association tracts and close to the high-frequency regions (**Fig. 3.6B, Table 3.10**), suggesting that the association tracts may be more vulnerable in glioblastoma patients. The top five most likely disrupted Distant regions (**Fig. 3.6C)** were mainly in the low-frequency regions.

3.4.4 Topological features and their association with Distant regions

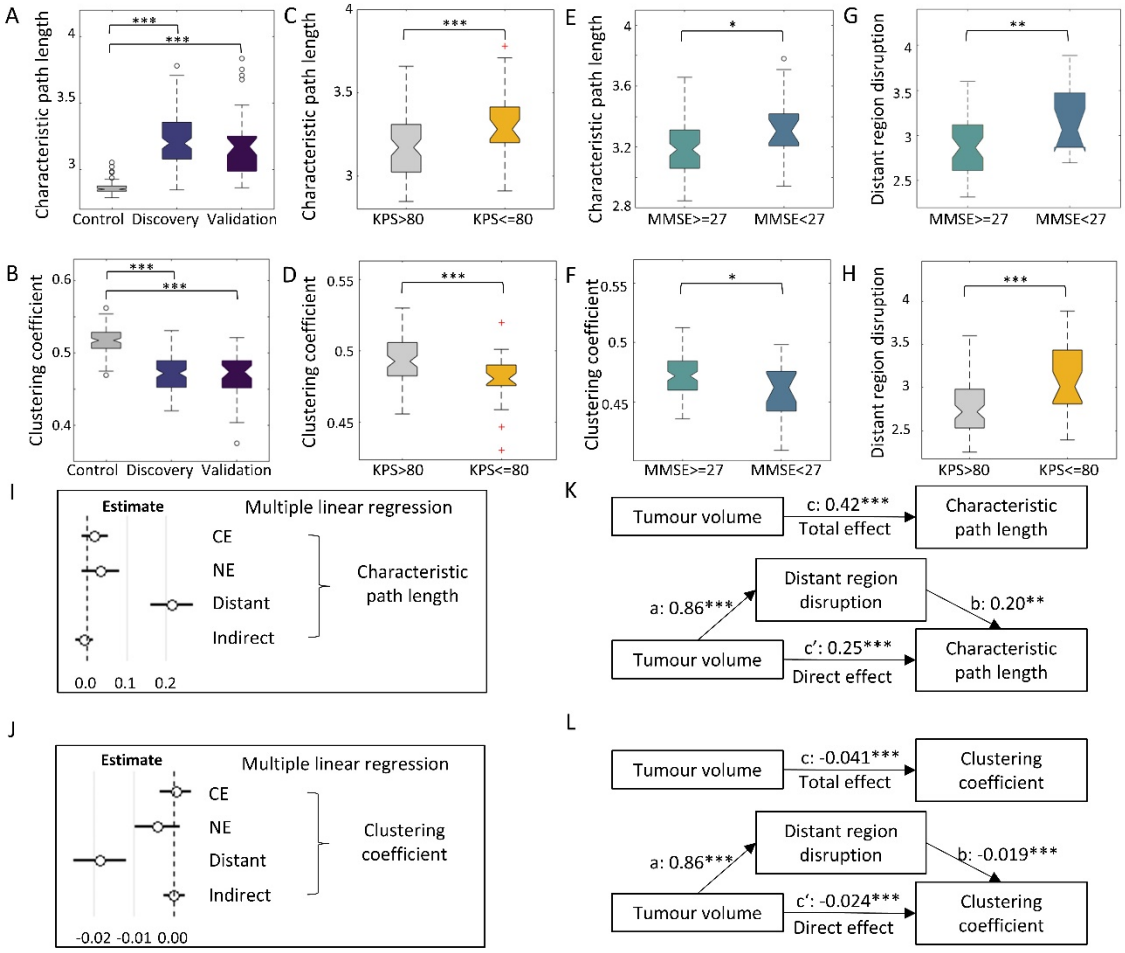


Fig. 3.7. Topological alteration of the connectome. Patients show increased characteristic path length **(A)** and decreased clustering coefficient **(B)** than the controls. Patient subgroups with worse pre-operative KPS **(C, D)** and MMSE **(E, F)** scores show increased characteristic path length and decreased clustering coefficient. Disruption of Distant regions is higher in the subgroups with worse MMSE **(G)** and KPS **(H)**, and it is the only significant predictor of characteristic path length **(I)** and clustering coefficient **(J)** in multiple linear regression. **(K)** The effects of tumour volume on characteristic path length are mediated by the disruption of Distant regions: total effect (c path) = 0.42, $P < 0.001$; direct effect (c' path) = 0.25, $P < 0.001$; mediation effect (c – c') = 0.17, $P = 0.008$. (**L**) The effects of tumour volume on the

clustering coefficient are mediated by the disruption of Distant regions: total effect (c path) = -0.041, $P < 0.001$; direct effect (c' path) = -0.024, $P < 0.001$; mediation effect (c – c') = -0.017, $P < 0.001$. **WM:** white matter, **MMSE**: Mini-Mental State Examination; **KPS**: Karnofsky Performance Status. **CE**: contrast-enhancing, **NE**: non-enhancing. *P* value significant codes: $P < 0.001$ ***, $P < 0.01$ **, $P < 0.05$ *.

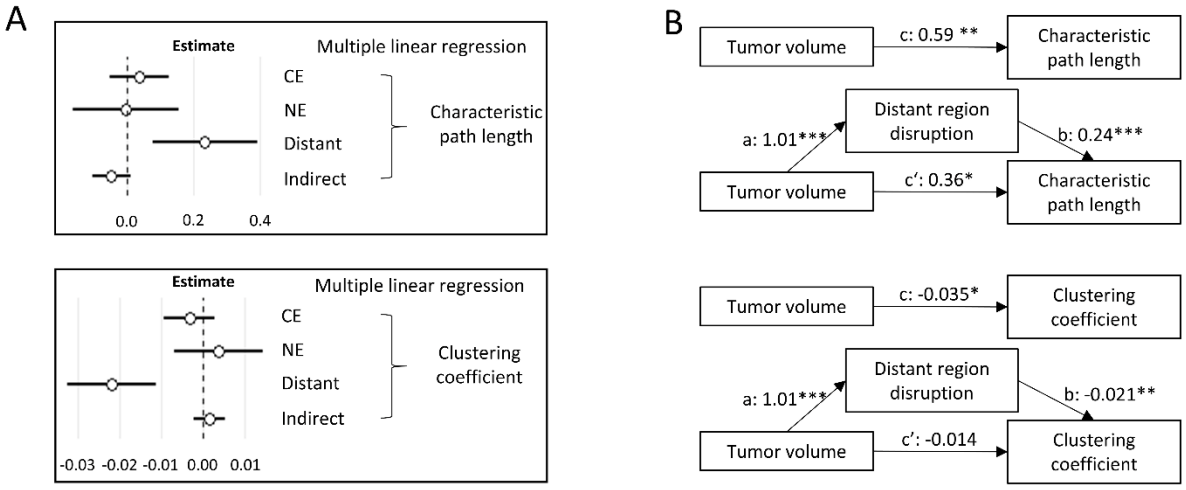


Fig. 3.8. Topological alteration of the structural connectome of the Validation cohort. (A) The disruption of the Distant regions is the only significant predictor for characteristic path length (estimate = 0.23, $P = 0.005$) **(upper)** and clustering coefficient (estimate = -0.022, $P < 0.001$) **(lower)** in multiple linear regression models. **(B)** The effects of tumour volume on characteristic path length are mediated by the disruption of the Distant regions **(upper)**: total effect (c path) = 0.59, $P = 0.008$; direct effect (c' path) = 0.36, $P = 0.01$; mediation effect (c – c') = 0.23, $P < 0.001$ (mediated by the disruption of the Distant regions). The effects of tumour volume on the clustering coefficient are mediated by the disruption of the Distant regions **(lower)**: total effect (c path) = -0.035, $P < 0.001$; direct effect (c' path) = -0.014, $P = 0.367$; mediation effect (c – c') = -0.021, $P = 0.005$ (mediated by the disruption of Distant regions). *P* values significant codes: $P < 0.001$ ***, $P < 0.01$ **, $P < 0.05$ *.

3.4.4.1 The focal tumour alters the topological property of the connectome

We observed significantly higher characteristic path length in patient networks than in healthy controls ($P < 0.001$, **Fig. 3.7A**). In contrast, the clustering coefficient of patients was significantly lower than that of healthy controls ($P < 0.001$, **Fig. 3.7B**, **Table 3.11**). These results reveal that tumour lesions could dramatically alter the topology property of the structural connectome. No difference was found between topological features between the two patient cohorts, which suggests the robustness of our approach.

Table 3.11. Topological features of healthy controls and patient cohorts

Topological features	Group	Mean ± SD	95% CI	*P* (vs. Validation)	*P* (vs. Control)
Clustering coefficient	Discovery	0.47 ± 0.03	0.43 - 0.52	1.000	<0.001
	Validation	0.47 ± 0.03	0.41 - 0.52	-	<0.001
	Control	0.52 ± 0.02	0.48 - 0.55	-	-
Characteristic path length	Discovery	3.22 ± 0.20	2.93 - 3.57	1.000	<0.001
	Validation	3.18 ± 0.24	2.88 - 3.73	-	<0.001
	Control	2.86 ± 0.04	2.80 - 2.93	-	-
P value adjusted by FDR					

We next determined the clinical significance of connectome topology by comparing the topological properties of the patient subgroups stratified by MMSE and KPS scores. We found that the patients with lower MMSE or KPS scores presented lower clustering coefficient (MMSE: $P = 0.012$, KPS: $P < 0.001$, **Fig. 3.7C & E**) and higher characteristic path length (MMSE: $P = 0.013$, KPS: $P < 0.001$, **Fig. 3.7D & F)**. Moreover, characteristic path length ($r = 0.43$, $P < 0.001$) was positively correlated with tumour volume, while clustering coefficient ($r = -0.45$, $P < 0.001$) was negatively correlated with tumour volume, indicating that a larger focal lesion may have a greater influence on the connectome topology (**Table 3.12**).

Table 3.12. Pearson correlations between topological features and tumour volume

	Discovery		Validation	
	Pearson r	***P***	**Pearson r**	***P***
Clustering coefficient	-0.45	<0.001	-0.49	0.002
Characteristic path length	0.43	<0.001	0.58	<0.001

P value adjusted by FDR

3.4.4.2 The disruption of Distant regions is associated with the topological alteration

To understand the relation between the regional disruption with topological properties, we performed a multiple linear regression, which revealed that the disruption of Distant regions was the only significant predictor of characteristic path length (Estimate = 0.21, $P < 0.001$) and clustering coefficient (Estimate = -0.018, $P < 0.001$, **Fig. 3.7I & J)**.

We further performed the mediation analysis, which showed that tumour volume had both significant direct and indirect effects (mediated by the disruption of Distant regions) on characteristic path length (direct: $P < 0.001$, indirect $P = 0.008$) and clustering coefficient (direct & indirect $P < 0.001$) (**Fig. 3.7K & L)**. The findings were confirmed by the Validation cohort (**Fig. 3.8**).

We additionally compared the disruptions of Distant regions in the subgroups stratified by the MMSE and KPS scores. We noticed that the patients with higher MMSE or higher KPS scores displayed significantly lower disruption of Distant regions **(Fig. 3.7G & H)**, consistent with the distinct network topological properties in these subgroups. The results further imply the association between the disrupted Distant regions and connectome topology.

For both disruption indices and topological features, we evaluated the prognostic value using log-rank tests and Cox proportional hazards models.

3.4.4.3 Topological features and disruption of Distant regions are prognostic

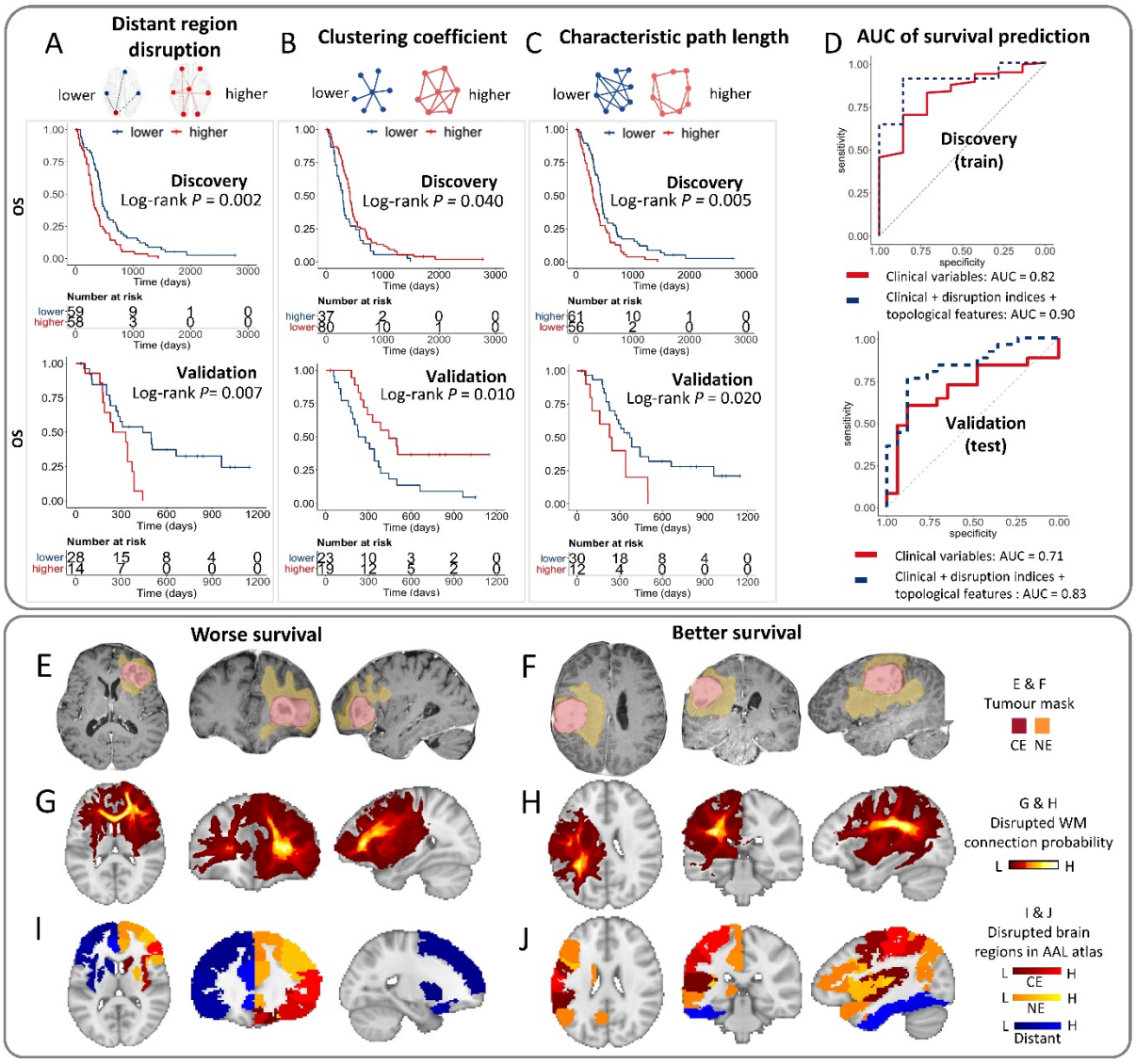


Fig. 3.9 The prognostic value of disruption indices and topological features. Top: In both cohorts, higher disruption of Distant regions **(A)**, lower clustering coefficient **(B)**, and higher characteristic path length **(C)** are associated with worse OS. **(D)** The model of predicting OS using clinical factors, disruption indices, and topological features shows improved AUC than clinical factors alone. Bottom: Two examples with worse or better survival (OS: 317 vs. 1555 days; PFS: 159 vs. 747 days). Both are IDH wildtype and MGMT unmethylated tumours of similar visible size in two males (aged 67 vs. 69 yrs.), who underwent complete resection

followed by temozolomide chemoradiotherapy **(E & F)**. Patients have similar tumour sizes on post-contrast T1 (23.6 vs. 25.0 cm^3). The patient with worse survival **(G)** has more widespread connection disruption beyond the visible lesion, compared to the patient with better survival **(H)**; The disruption indices of Distant regions (blue) are 3.0 **(I)** and 2.8 **(J)**, respectively. Their topological features are distinct (clustering coefficient 0.44 vs. 0.48: characteristic path length 3.31 vs. 3.17). **OS**: Overall survival. **HR**: Hazard ratio. **WM**: white matter. **AUC:** Area under the ROC Curve. **CE:** contrast-enhancing. **NE**: non-enhancing.

3.4.5 Logistic model for survival prediction

We trained a logistic regression model on the Discovery cohort to predict the two-year OS using the disruption indices and topological features significant in the univariate Cox model. The baseline model, including the above significant clinical variables (i.e., age, EOR, and adjuvant therapy), achieved an AUC of 0.82 (CI: 0.68-0.96). By adding the disruption indices and topological features into the baseline model, the AUC was improved to 0.90 (CI: 0.80 - 0.99, Fig. 3.5D). We further tested this trained model in the Validation cohort for out-of-sample validation, which confirmed the improved accuracy (AUC = 0.83, CI: 0.71-0.96) by including disruption indices and topological features over the baseline model (AUC = 0.71, CI: 0.54-0.87).

We presented two examples (**Fig. 3.9E-J)** with similar clinical variables but different disruptions of Distant regions, topological features, and finally distinct survival (above and below the median, respectively).

3.4.6 Log-rank test

In the subgroups stratified by the mean disruption of Distant regions (2.9), patients with higher disruption had worse survival than lower disruption (OS: median 293 vs. 449 days, P = 0.002, PFS: median 238 vs. 307 days, P = 0.019, **Fig. 3.9A**). Further, the subgroups stratified by the optimal cut-off of topological features (clustering coefficient: 0.46;

characteristic path length: 3.20) also had distinct survival. Precisely, the subgroup with a higher clustering coefficient had better survival than that with a lower clustering coefficient (OS: median 475 vs. 294 days, P = 0.040, PFS: median 306 vs. 238 days, P = 0.002, **Fig. 3.9B**). The subgroup with lower characteristic path length showed better survival than that with higher characteristic path length (OS: median 465 vs. 288 days, P = 0.005, PFS: median 312 vs. 244 days, P = 0.012, **Fig. 3.9C**). We further confirmed the findings in the Validation cohort using identical cut-offs.

3.4.7 Cox proportional hazards modelling

Table 3.13. Univariate survival statistics of Discovery cohort.

Feature	OS			PFS		
	HR	95%CI	*P*	HR	95%CI	*P*
Clinical variables						
Age	1.03	1.01 -1.05	**0.004**	1.03	1.00-1.05	**0.021**
Sex[a]	0.81	0.52-1.25	0.333	0.75	0.47-1.19	0.217
Performance[b]	1.60	1.09-2.36	**0.018**	1.63	1.04-2.55	**0.033**
IDH[c]	0.59	0.25-1.36	0.211	0.52	0.22-1.21	0.131
MGMT[d]	0.77	0.52-1.14	0.196	0.68	0.43-1.07	0.094
EOR[e]	1.89	1.26-2.84	**0.002**	1.90	1.19-3.03	**0.007**
Adjuvant treatment[f]	0.21	0.13-0.34	**<0.001**	0.22	0.11-0.41	**<0.001**
Tumour volume	1.01	1.00-1.01	**0.001**	1.01	1.00-1.02	**0.045**
Eloquent location[g]	0.93	0.64-1.36	0.711	1.06	0.69-1.62	0.807
Deep white matter[h]	0.85	0.58-1.24	0.386	0.86	0.57-1.31	0.487
Non-enhancing volume	0.87	0.72-1.05	0.135	0.87	0.70-1.07	0.192
Disruption indices						
Direct connection	1.07	0.87-1.30	0.790	1.08	0.88-1.32	0.464
Indirect connection	1.36	1.13-1.65	**0.007**	2.43	1.02-5.81	**0.046**
CE regions	0.95	0.86-1.04	0.667	0.96	0.86-1.06	0.418
NE regions	1.01	0.88-1.15	0.939	1.00	0.87-1.15	0.979
Distant regions	1.46	1.08-1.99	**0.049**	1.49	1.07-2.07	**0.019**
Indirect regions	1.06	0.87-1.29	0.790	0.80	0.83-1.28	0.795
Topological features						
Clustering coefficient	0.63	0.42-0.93	**0.035**	0.49	0.30-0.78	**0.002**
Characteristic path length	1.56	1.06-2.29	**0.035**	1.82	1.16-2.84	**0.009**

[a]Female as the reference. [b]KPS 90-100 as the reference. [c]IDH wildtype as reference. [d]Unmethylated MGMT as reference. [e]Incomplete resection as reference. [f]Concurrent chemoradiotherapy (CCRT) as reference. [g]Non-eloquent location as reference. [h]Affected deep white matter as reference. EOR: extent of resection. KPS: Karnofsky Performance Score

From the Cox proportional hazards models (**Table 3.13**), we observed that higher disruptions of Indirect connection (OS: HR = 1.36, P = 0.007; PFS: HR = 2.43, P = 0.046) and Distant regions (OS: HR = 1.46, P = 0.049; PFS: HR = 1.49, P = 0.019) were associated

with worse survival. For topological features, a higher clustering coefficient was associated with better survival (OS: HR = 0.63, P = 0.035; PFS: HR = 0.49, P = 0.002), while a higher characteristic path length was associated with worse survival (OS: HR = 1.56, P = 0.035; PFS: HR = 1.82, P = 0.009).

In the multivariate model adjusting for all the significant clinical covariates from the univariate models, the disruption of Distant regions and topological features remained significant (**Fig. 3.10, Table 3.14**). Their prognostic value was confirmed by the Validation cohort (**Table 3.15 & 3.16**).

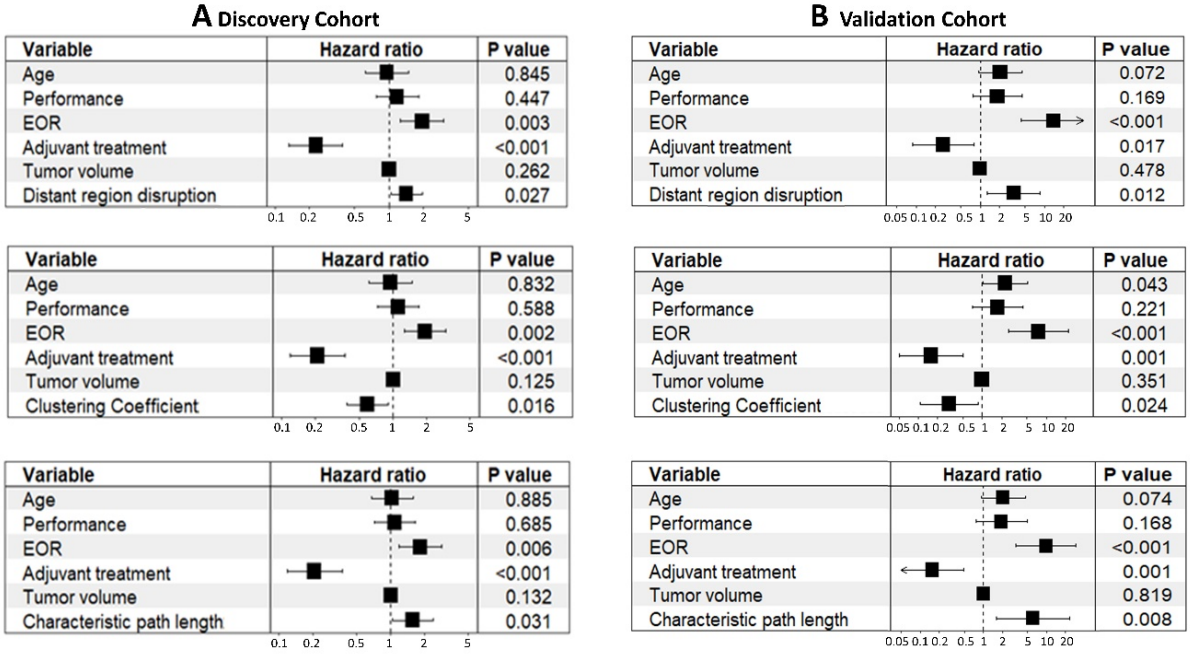


Fig. 3.10 Forest plots of multivariate survival modelling. For the Discovery **(A)** and Validation **(B)** cohorts, the higher disruption of Distant regions, higher characteristic path length, and lower clustering coefficient are associated with worse survival. The prognostic value is independent of the significant clinical variables. **EOR**: the extent of resection.

Table 3.14. Multivariate survival statistics of the Discovery cohort

Feature	OSN			PFSN		
	HR	95%CI	*P* value	HR	95%CI	*P* value
Age	1.03	0.66-1.59	0.907	1.18	0.73-1.91	0.507
Performance[a]	1.19	0.77-1.84	0.432	1.21	0.72-2.02	0.474
EOR[b]	1.68	1.07-2.64	0.024	1.97	1.19-3.27	0.008
Adjuvant treatment[c]	0.24	0.14-0.41	<0.001	0.27	0.13-0.55	<0.001
Tumour volume	1.01	1.00-1.02	0.102	1.00	0.99-1.01	0.352
Indirect connections	1.32	1.07-1.61	**0.009**	1.17	0.95-1.44	0.146
Age	0.96	0.62-1.48	0.845	0.99	0.61-1.61	0.976
Performance[a]	1.18	0.77-1.81	0.447	1.27	0.76-2.14	0.365
EOR[b]	1.96	1.26-3.03	0.003	2.25	1.35-3.74	0.002
Adjuvant treatment[c]	0.23	0.13-0.39	<0.001	0.23	0.11-0.47	<0.001
Tumour volume	1.01	1.00-1.02	0.262	1.00	0.99-1.01	0.940
Distant regions	1.43	1.04-1.95	**0.027**	1.58	1.11-2.24	**0.011**
Age	0.95	0.61-1.49	0.832	1.10	0.67-1.79	0.709
Performance[a]	1.13	0.73-1.73	0.588	1.14	0.69-1.88	0.620
EOR[b]	1.96	1.27-3.01	0.002	2.09	1.27-3.41	0.003
Adjuvant treatment[c]	0.21	0.12-0.37	<0.001	0.26	0.12-0.54	<0.001
Tumour volume	1.01	1.00-1.02	0.125	1.00	0.99-1.01	0.552
Clustering coefficient	0.59	0.38-0.91	**0.016**	0.53	0.32-0.88	**0.013**
Age	1.03	0.67-1.59	0.885	1.16	0.72-1.87	0.550
Performance[a]	1.09	0.71-1.68	0.685	1.08	0.65-1.80	0.766
EOR[b]	1.85	1.20-2.85	0.006	1.97	1.19-3.25	0.008
Adjuvant treatment[c]	0.21	0.12-0.37	<0.001	0.24	0.11-0.49	<0.001
Tumour volume	1.01	1.00-1.02	0.132	1.00	0.99-1.01	0.594
Characteristic path length	1.59	1.04-2.43	**0.031**	1.58	0.97-2.57	0.067

(a). KPS Performance > 70 as the reference; **(b)**. Complete resection as the reference; **(c)** Non-CCRT as the reference. *P* value adjusted. **EOR**: extent of resection, **KPS**: Karnofsky Performance Score; **CCRT**: temozolomide concurrent chemoradiotherapy. **Bold *P* values** are still significant after adjusted by FDR

Table 3.15. Univariate survival statistics of the Validation cohort

Feature	OS			PFS		
	HR	95%CI	*P* value	HR	95%CI	*P* value
Clinical variables						
Age	1.05	1.01-1.09	0.018	1.05	1.00-1.10	0.016
Sex[a]	0.99	0.47-2.09	0.973	1.55	0.68-3.50	0.294
Performance[b]	1.58	0.78-3.22	0.205	0.82	0.39-1.71	0.595
IDH[c]	0.63	0.09-4.67	0.652	0.36	0.05-2.75	0.327
MGMT[d]	0.61	0.30-1.24	0.178	0.44	0.20-0.95	**0.036**
EOR[e]	8.69	3.42-22.1	**<0.001**	3.35	1.06-10.5	**0.039**
Adjuvant treatment[f]	0.15	0.07-0.36	**<0.001**	0.28	0.11-0.73	**0.010**
Tumour volume	1.00	1.00-1.00	0.790	1.00	1.00-1.00	0.545
Eloquent location[g]	0.65	0.23-1.85	0.416	0.71	0.28-1.80	0.467
Deep white matter[h]	0.42	0.19-0.94	**0.036**	1.85	0.80-4.30	0.150
Non-enhancing volume	1.33	0.90-1.96	0.159	1.30	0.87-1.96	0.198
Disruption indices						
Direct connection	1.10	0.78-1.57	0.577	1.09	0.74-1.61	0.659
Indirect connection	1.22	0.44-3.41	0.702	3.62	1.25-10.5	**0.018**
CE region	1.02	0.83-1.26	0.833	1.01	0.78-1.30	0.954
NE region	1.01	0.82-1.25	0.896	0.99	0.77-1.28	0.969
Distant region	3.36	1.50-7.53	**0.003**	2.03	1.10-3.77	**0.025**
Indirect region	0.92	0.70-1.24	0.614	0.94	0.72-1.24	0.667
Topological features						
Clustering coefficient	0.43	0.21-0.88	**0.021**	0.28	0.10-0.75	**0.012**
Characteristic path length	3.61	1.21-10.8	**0.021**	5.75	1.49-22.2	**0.011**

(a). Female as the reference; **(b)**. KPS Performance > 70 as the reference; **(c)**. IDH wildtype as the reference; **(d)** Unmethylated MGMT as the reference; **(e)**. Complete resection as the reference; **(f)** Non-CCRT as the reference. **(g).** Non-eloquent location as reference. **(h)** Deep white matter tracts affected as reference. **EOR**: extent of resection. **KPS**: Karnofsky Performance Score; **CCRT**: temozolomide concurrent chemoradiotherapy. *P* value adjusted by FDR

Table 3.16. Multivariate survival statistics of the Validation cohort

Feature	OS			PFS		
	HR	95%CI	*P* value	HR	95%CI	*P* value
Age	1.81	0.82-4.03	0.143	2.62	1.12-6.13	0.026
Performance[a]	1.82	0.72-4.62	0.205	4.00	1.46-11.0	0.007
EOR[b]	10.0	3.21-31.4	<0.001	7.01	1.75-28.1	0.006
Adjuvant treatment[c]	0.15	0.05-0.44	0.001	0.16	0.04-0.61	0.007
Tumour volume	1.00	0.98-1.02	0.922	1.01	0.99-1.03	0.326
Indirect connections	1.30	0.90-1.87	0.163	2.20	1.39-3.47	**0.001**
Age	2.05	0.94-4.49	0.072	3.01	1.28-7.12	0.012
Performance[a]	1.86	0.77-4.52	0.169	3.26	1.21-8.83	0.020
EOR[b]	14.0	4.36-45.2	<0.001	5.31	1.39-20.4	0.015
Adjuvant treatment[c]	0.26	0.09-0.79	0.017	0.42	0.09-1.83	0.246
Tumour volume	0.99	0.98-1.01	0.478	1.00	0.98-1.02	0.934
Distant regions	3.36	1.30-8.67	**0.012**	2.47	1.08-5.66	**0.033**
Age	2.31	1.03-5.18	0.043	2.88	1.19-6.97	0.019
Performance[a]	1.75	0.71-4.32	0.221	2.41	0.94-6.13	0.066
EOR[b]	7.60	2.56-22.6	<0.001	2.24	0.47-10.7	0.311
Adjuvant treatment[c]	0.16	0.05-0.49	0.001	0.27	0.07-1.05	0.059
Tumour volume	0.99	0.98-1.01	0.351	1.00	0.98-1.02	0.797
Clustering coefficient	0.30	0.11-0.85	**0.024**	0.28	0.06-1.25	0.095
Age	2.08	0.93-4.63	0.074	2.50	1.07-5.88	0.035
Performance[a]	1.94	0.76-4.96	0.168	2.72	1.04-7.14	0.042
EOR[b]	9.88	3.30-29.6	<0.001	3.22	0.78-13.3	0.106
Adjuvant treatment[c]	0.16	0.05-0.49	0.001	0.21	0.05-0.87	0.031
Tumour volume	1.00	0.99-1.02	0.819	1.01	0.99-1.03	0.384
Characteristic path length	6.16	1.61-23.5	**0.008**	7.89	1.40-44.5	**0.019**

(a). KPS Performance = 0 as the reference; **(b)**. Complete resection as the reference; **(c)** Non-CCRT as the reference. *P* value adjusted. **EOR**: extent of resection, **KPS**: Karnofsky Performance Score; **CCRT**: temozolomide concurrent chemoradiotherapy. **Bold *P* values** are still significant after adjusted by FDR

3.4.8 Preserved connectivity and recurrence distance associated with Distant regions

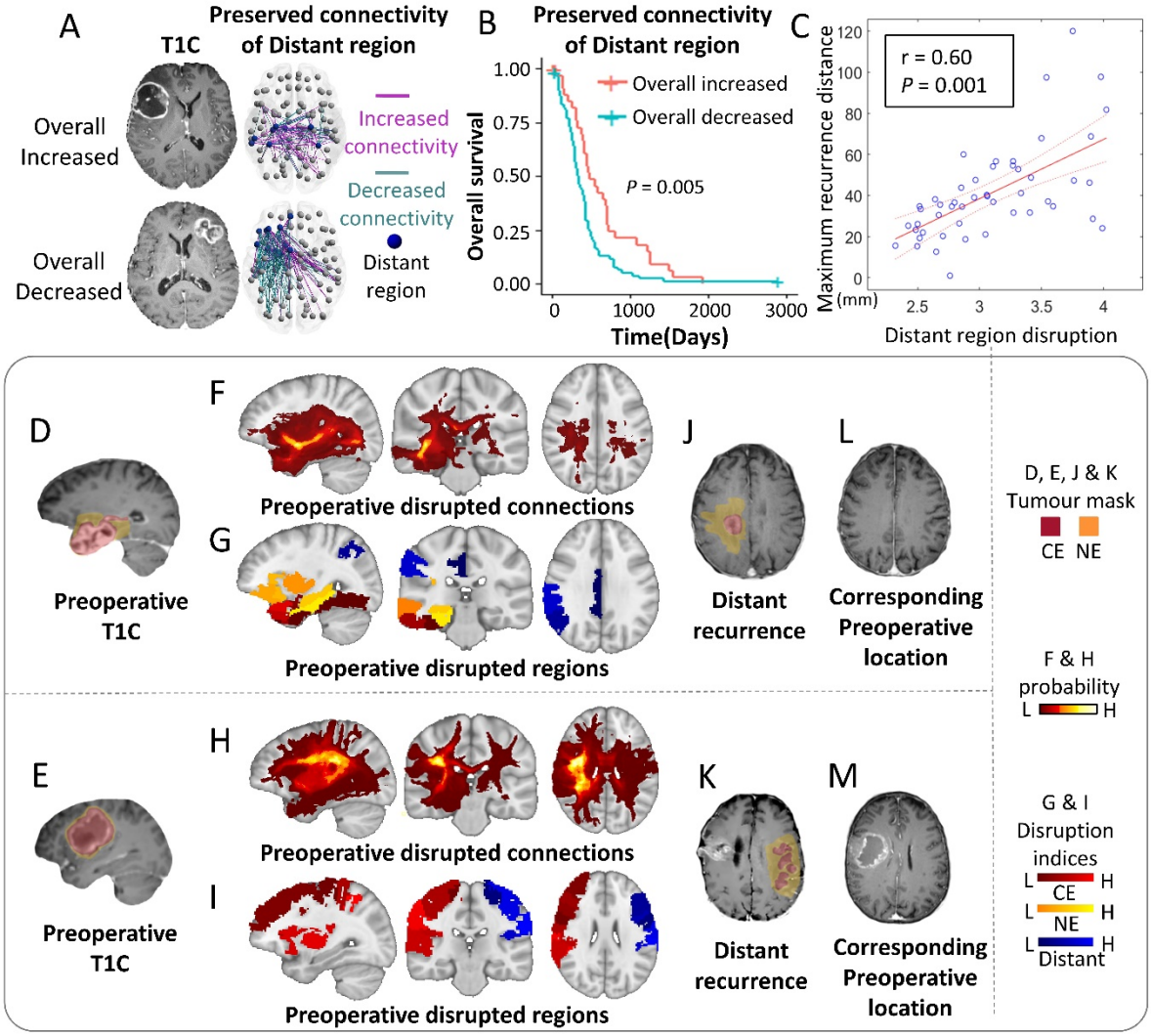


Fig 3.11. The disruptions of the Distant regions indicate survival significance and distant recurrence. Top: After removing the disrupted WM connections of the Distant regions, the preserved connections are categorised as increased or decreased connectivity in comparisons with healthy controls and aggregated to stratify patients. Two examples of overall increased and decreased connectivity are in **(A)**. The subgroup with overall increased connectivity shows better survival than overall decreased connectivity **(B)**. The disruption index of the Distant region is positively correlated with the maximum recurrence distance **(C)**. **Bottom**: two examples of distant recurrence. Both patients present solitary visible lesions on

pre-operative post-contrast T1 (T1C) images **(D, E)**, widespread disrupted WM connections **(F, H)** and brain regions **(G, I)**. In both patients, the distant recurrence location, either ipsilesional recurrence **(J)** or contralesional recurrence **(K)**, corresponds to the Distant regions (blue), which are linked to the primary lesion via the WM connections shown in **(F, H)**. A retrospective review of the pre-operative T1C images reveals no visible lesion in the recurrence location **(L, M)**. **T1C**: T1 contrast. **WM**: white matter. **CE**: contrast-enhancing. **NE**: non-enhancing.

3.4.8.1 The preserved connectome of Distant regions indicates patient survival

As the Distant region disruption is the most significant biomarker, we further analysed its potential effect on the preserved connectome. Firstly, we observed that 93.2% (109/117) patients displayed overall changes in connectivity Among them, 24.7% (29/117) patients displayed overall increased connectivity, while 68.4% (80/117) patients showed overall decreased connectivity. We present two case examples with overall increased and decreased connectivity in the preserved connectome of the Distant regions, respectively (**Fig. 3.11A**). The log-rank test showed that those patients with overall increased connectivity were associated with better survival (P = 0.005, **Fig. 3.11B**), confirmed by the validation cohort (**Fig. 3.12**). The findings suggest that more integrated brain connectivity is associated with better patient survival, suggesting *a priori* more resilient connectome or network reorganisation.

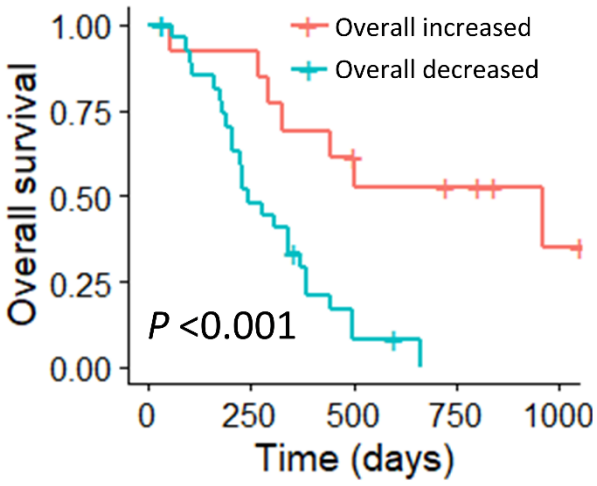


Fig. 3.12. Kaplan-Meier plot showing patient stratification in the Validation cohort using the preserved connectivity of Distant regions. Patients with overall increased strength (10/42, 23.8%) show better overall survival than the patients with decreased strength (32/42, 76.2%). Log-rank test: $P < 0.001$.

3.4.8.2 Disrupted connectome indicates tumour recurrence

Finally, we found that the higher Distant region disruption was positively correlated with the furthest recurrence distance from the tumour centroid (r= 0.60, $P < 0.001$, **Fig. 3.11C**). We present two cases that showed distant recurrence in follow-up scans, where the disrupted Distant regions indicated occult tumour invasion invisible on the pre-operative MRI (**Fig. 3.11D-M**).

3.5 Discussion

The present study employed a connectome approach to investigate the disruption of structural connectivity in glioblastoma. Our main findings include: 1) glioblastomas cause widespread disrupted neural connectivity beyond the focal lesion. 2) the disruption of the normal-appearing brain could mediate the alteration of connectome topology, associated with worse patient performance, and impact patient survival. 3) the preserved connectome demonstrates evidence of network reorganisation associated with survival.

The finding that glioblastomas can cause widespread structural impairment is in line with the previous studies using resting-state fMRI, reporting that glioma induced widespread functional impairment (Daniel et al., 2020; Stoecklein et al., 2020). The evidence supports that glioblastoma should be treated as a systematic disease rather than a local disease. Moreover, we found that only the disruption of Distant regions was associated with topological alteration and patient survival among all the regional disruptions, suggesting the importance of characterising global neural connectivity.

In the anatomical mapping of the disrupted connectome, we found that the top disrupted Distant regions, e.g., posterior cingulate cortex and hippocampus, are essential structures of the limbic system, suggesting the propensity of the occult invasion affecting the limbic system. Moreover, the top affected anatomical tracts, e.g., arcuate fasciculus and superior longitudinal fasciculus, are long association tracts widely connecting separated gyri, suggesting that tumour invasion might spread through these tracts. Although at the macroscopic scale, our imaging findings may provide a perspective for previously reported neural-cancer interaction (Monje et al., 2020).

We found that the connectivity measures could provide superior biomarkers for brain tumour stratification over conventional clinical factors, e.g., tumour location and volume. The network efficiency of the human brain generally reflects the integrity of brain function (Sporns & Zwi, 2004). Glioblastoma patients displayed decreased network efficiency than healthy controls, likely due to tumour disturbance on brain function. Interestingly, our results suggest that the preserved connectome demonstrates evidence of reorganisation. The increased connectivity, indicating a more integrated network and more robust function, is associated with favourable survival. Although the mechanism remains further elucidated, it could suggest opportunities for understanding neural-cancer interaction for patient prognosis.

Our study has important clinical implications. Due to the remarkable heterogeneity of glioblastoma, the development of quantitative prognostic markers is crucial for precise diagnosis and treatment. The structural connectome and topological features confer a novel approach to investigating the systematic changes of neural connectivity in glioblastoma. It could enable us to understand the interaction between tumour invasion and neural

connectivity, which promises to stratify patients more precisely, help to develop targeted therapeutics, and reduce neurological deficits. From a translational perspective, our approach shows the potential to quickly produce metrics to enhance prognosis determination and patient stratification through automated imaging analytical software in the clinic, incorporating various data processing and modelling procedures, which could assist clinical decision-making in future. Additionally, tumour invasion in the normal-appearing brain visualised on the imaging could be integrated into the neuro-navigation and radiotherapy planning systems, offering more precise guidance for treatment targets.

Our study has limitations. Firstly, structural connectome can only directly measure the connectivity of connecting tracts. Although most brain regions are connected via tracts, some functionally related regions may not be structurally connected. Future work could include resting-state MRI and functional connectivity. Secondly, we only included *de novo* glioblastoma who received first-line treatment in the trial. Molecular markers, i.e., IDH and MGMT methylation, were not significant as previously reported in our cohorts. Finally, neuronal degeneration, such as Wallerian Degeneration, may also lead to the disruptions of WM connections, which may not be differentiated by our approach. Nonetheless, the significant prognostic value of disruption indices could support the capability of our approach in indicating tumour invasion.

3.6 Conclusion

In conclusion, this chapter validated the second hypothesis in **Chapter 1.4.2** that structural brain networks representing white matter connectivity have the potential to characterise the early invasion of glioblastomas and disruptions of brain networks are associated with the patient's clinical variables. Additionally, we discovered that glioblastoma causes widespread impairment of the structural connectome. The invisible disruption on conventional MRI and connectome integrity are correlated with patient survival. Studying neural connectivity may provide a valuable tool for patient stratification and precise treatment for brain tumours.

Chapter 4. Predicting isocitrate dehydrogenase mutation status in glioma using structural brain networks and graph neural networks

This is based on the following conference publication:

Wei, Yiran, et al. "Predicting isocitrate dehydrogenase mutation status in glioma using structural brain networks and graph neural networks." *International MICCAI Brainlesion Workshop*. Springer, Cham, 2022.

4.1 Abstract

Based on the literature review in **Chapter 1.1.2.** The IDH gene mutation provides critical diagnostic and prognostic value for glioma. It is of crucial significance to non-invasively predict IDH mutation based on pre-treatment MRI, which is discussed in **Chapter 1.2.** Machine learning/deep learning models show reasonable performance in predicting IDH mutation using MRI. However, most models neglect the systematic brain alterations caused by tumour invasion, where widespread infiltration along white matter tracts is a hallmark of glioma. Structural brain networks provide an effective tool to characterise brain organisation, which could be captured by the graph neural networks (GNN) to more accurately predict IDH mutation.

Here we propose a preliminary method to predict IDH mutation using GNN, based on the structural brain network of patients. Specifically, we first construct a network template of healthy subjects, consisting of atlases of edges (white matter tracts) and nodes (cortical/subcortical brain regions) to provide regions of interest (ROIs). Next, we employ autoencoders to extract the latent multi-modal MRI features from the ROIs of edges and nodes in patients, to train a GNN architecture for predicting IDH mutation. The results show that the proposed method outperforms the baseline models using the 3D-CNN and 3D-DenseNet. In addition, model interpretation suggests its ability to identify the tracts infiltrated

by tumours, corresponding to clinical prior knowledge. In conclusion, integrating brain networks with GNN offers a new avenue to study brain lesions using computational neuroscience and computer vision approaches.

4.2 Introduction

This chapter is a preliminary experiment designed to test the third hypothesis proposed in **Chapter 1.4.2,** including 1) it is feasible to construct brain networks from anatomical MRI with the assistance of anatomical priors and deep learning feature extraction. 2) models that learn from brain networks could better predict genotypes of gliomas than models that only learn from tumour images.

4.2.1 Significance of predicting IDH mutational status

As I introduced in **Section 1.1.2**, the mutation status of IDH genes is one of the most important biomarkers for the diagnosis and prognosis of gliomas, where IDH mutants tend to have a better prognosis than IDH wild-types (Yen et al., 2010). Due to their crucial value in clinical practice, IDH mutations have been established as one of the landmark molecular markers for glioma patients, recommended by the World Health Organisation classification of tumours of the Central Nervous System for routine assessment in glioma patients (Louis et al., 2016).

As I described in **Section 1.1.2**, the most widely used approaches to determine IDH mutation status, i.e., immunohistochemistry and targeted gene sequencing, rely on tumour samples (Louis et al., 2016), which therefore cannot be assessed on those patients who are not suitable for tumour resection or biopsy. Further, as the assays usually are time-consuming and expensive, they are not available in some institutions.

Meanwhile, the radiogenomic approach has shown promise in predicting molecular markers based on radiological images. Mounting evidence has supported the feasibility of predicting IDH mutation status using the pre-operative MRI (Choi et al., 2020; Hyare et al., 2019; Liang et al., 2018). The most used MRI sequences include pre-contrast T1, postcontrast T1, T2, and T2-weighted-Fluid-Attenuated Inversion Recovery (FLAIR). Integrating the

quantitative information from multi-modal MRI promises to provide a non-invasive approach to characterise glioma and predict IDH mutations for better treatment planning and prognostication (Li, Wang, Yan, Torheim, et al., 2019).

4.2.2 Brain structural networks

As I introduced in **Chapter 1**, evidence shows that glioma cells tend to invade along the white matter pathway (Wang et al., 2019) and infiltrate the whole brain (Stoecklein et al., 2020). Additionally, as I reported in **Chapter 2**, the clinical significance of structural brain networks is identified in brain tumours.

Therefore, investigating structural brain networks could offer a tool to investigate glioma invasion on both tumour core and normal-appearing brain regions. Further, a previous study revealed that IDH mutations could be associated with different invasive phenotypes of glioma (Price et al., 2017). To this end, we hypothesise that employing the structural brain networks could provide value for predicting IDH mutation status. With prior knowledge of brain structure and anatomy incorporated, a more robust prediction model could be achieved.

4.2.3 Graph neural networks

The advantage of GNN is discussed in **Chapter 1.3.3.2.** By employing the GNN on structural brain networks, the topological information contained in the structural brain networks could be effectively explored, which would consequently incorporate the prior knowledge of brain organisation and perceive the critical information of tumour invasion at the whole-brain level.

4.2.4 Related work

Current methods of predicting IDH mutation status include radiomics/machine learning-based, deep learning-based, or a combination of both. Radiomics/machine learning-based methods extract high dimensional handcrafted features from the MRIs, e.g., tumour intensity, shape, texture, etc., to train machine learning prediction models of molecular markers,

tumour grades, or patient survival (Hyare et al., 2019). Deep learning-based approaches provide an end-to-end model without pre-defined imaging features in the prediction tasks (Liang et al., 2018). Some other methods integrated the radiomic features into a deep neural network to enhance prediction performance (Choi et al., 2020). Albeit reasonable prediction accuracy, most of these methods are mainly driven by computer vision tasks, without considering the systematic alteration of the brain organisation during tumour invasion. Incorporating the prior knowledge from the neuroscience field shows promise to improve the prediction model. A more comprehensive comparison will be conducted in **Chapter 5.**

4.2.5 Proposed methods

Here we propose an approach of using GNN to predict IDH mutation status, based on the structural brain networks generated from multi-model MRI and prior human brain atlases. Our contributions include:

– A method to incorporate the prior knowledge of brain atlases with the anatomical MRI to generate structural brain networks.

– A novel architecture of GNN with a specialised graph convolutional operator for aggregating multi-dimensional latent features of the multi-model MRI.

– To our best knowledge, this is the first study that leverages GNN on the multi-modal MRI to predict the IDH mutation status of glioma.

4.3 Methods

4.3.1 Datasets

This study included the pre-operative multi-modal MRI (pre-contrast T1, postcontrast T1, T2, and FLAIR) of 389 glioma patients. MRI images of 274 patients were downloaded from The Cancer Imaging Archive (TCIA) website (Clark et al., 2013), whereas 115 patients were available from an in-house cohort. 17 of 389 patients who have missing IDH mutation status or incomplete MRI modalities were excluded. Of the included patients, 103 patients are IDH mutants, and 269 are IDH wild-type.

4.3.2 Imaging pre-processing

We processed the multi-modal MRI following a standard pipeline (Bakas et al., 2017). Firstly, the T1, T2, and FLAIR were co-registered to the post-contrast T1 using the FMRIB's Linear Image Registration Tool (Jenkinson et al., 2002). Then, brain extraction was performed on all MRI modalities to remove the skull using the Brain Extraction Tool in the FMRIB Software Library (FSL) (Jenkinson et al., 2002; Smith, 2002). We also performed histogram matching (Nyúl et al., 2000) and voxel smoothing with SUSAN noise reduction (Smith & Brady, 1997). A researcher and a neurosurgeon performed a sequential manual correction of brain masks (e.g., the researcher corrected masks first then the neurosurgeon double-checked corrected masks, each mask was corrected twice by two individuals). Finally, all modalities were non-linearly co-registered using the Advanced Normalization Tools (ANTs) (Avants et al., 2009) to the MNI152 standard space, i.e., MNI-152-T1-2MM-brain provided by the FSL (Figure 4.1A).

4.3.3 Constructing patient structural brain networks

4.3.3.1 Brain network template

We leveraged the brain network template derived from healthy subjects to construct brain networks in lesioned brains (Salvalaggio et al., 2020). First, we used the prior brain atlases in healthy subjects as the template of brain networks, generating regions of interest (ROIs) for characterising the brain networks in patients based on multi-modal MRI. Specifically, we used the Automated Anatomical Labelling (AAL) atlas (Tzourio-Mazoyer et al., 2002) as the node ROIs (Figure 4.1B), which includes 90 brain cortical and subcortical regions. Further, we generated a brain connectivity atlas from ten healthy subjects scanned by high-resolution diffusion MRI to derive the edge ROIs of the structural brain networks (Figure 4.1C). We used a similar approach to generating a brain connectivity atlas (Fagerholm et al., 2015). In brief, firstly, pairwise tractography among the 90 regions of the AAL atlas was performed in healthy subjects, and then the resultant tract pathways were co-registered to the MNI152

standard space. Next, the corresponding tracts of all healthy subjects were averaged for each edge between two nodes. Finally, the top 5% voxels of the tract density were retained and binarised to generate robust edge ROIs. The generated edge atlas is shown in Figure 4.1C.

4.3.3.2 Latent features of nodes and edges from autoencoders

MRI voxels within the ROIs of the node or edge atlases across the whole brain were extracted and then concatenated to voxel vectors (Figure 4.1D & E). We then used two autoencoders to extract the latent features from the voxel vectors of node and edge, respectively. Vector size was set as 2500 (voxels) × 4 (modalities) = 10000. For edges and nodes with few voxels, the vectors were padded with zeros. The patient cohort was shuffled and split into an 80:20 ratio for training and testing data. Two autoencoders were trained by edge and node voxel vectors of the training data (Figure 4.1F & G). Finally, the latent features of edge or node voxels were derived, with the dimension of the edge or node vectors substantially decreased from 10000 to 12 (Figure 4.1H & I). The 12 latent features were used as the input of the GNN (Figure 4.1J). The logistic sigmoid function was applied as a transfer function for both the encoder and decoder. L2 regularisation with a coefficient of 0.001 was used. MSE loss was set as the loss function.

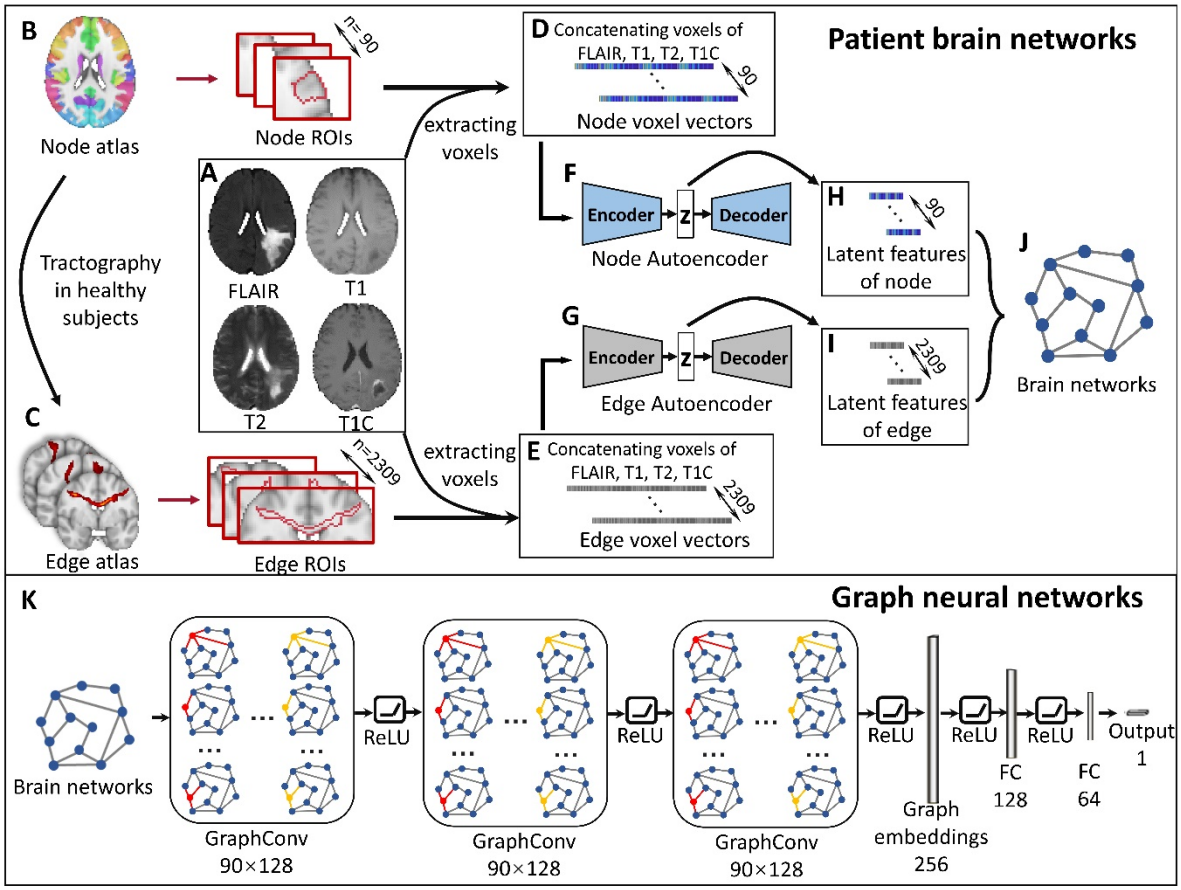


Fig. 4.1. Study workflow. Upper: the pipeline of constructing patient brain networks. **A**: Patient MRIs are pre-processed and co-registered to the atlas space. **B**: The AAL atlas of 90 ROIs is used as the node atlas. **C**: The edge atlas is generated from performing tractography among the 90 ROIs on the diffusion MRI of healthy subjects. **D & E** Multi-modal MRI voxels within the node/edge ROIs are extracted and concatenated to voxel vectors to characterise the node/edge. 90 nodes were from the AAL atlas while 2309 edges are the edges that exist in 9 of 10 healthy subjects in tractography. **F & G**: Two autoencoders are trained using edge and node voxel vectors. **H & I**: Encoders of trained autoencoders are used to extract the low dimensional latent features *z* from the high dimensional node/edge voxels vector, respectively. **J** Latent node/edge features are then rearranged into graph format as the input of the GNN. **K** Graph convolutional neural networks consist of three hidden graph convolutional layers, one graph embedding layer, and two fully connected (FC) layers.

4.3.4 Predicting IDH mutation status using GNN

The patient brain networks constructed above were used to train the GNN, with the multi-modal MRI latent features as inputs. In addition to the 80:20 ratio of training and testing data, training data was split again into an 80:20 ratio for cross-validation. The proposed GNN consist of three graph convolutional layers similar to the one defined in [14], one node-to-graph embedding layer, and two fully connected feed-forward layers (Figure 4.1K). We used a binary cross-entropy loss, while the optimisation was done using Adam optimiser.

The graph convolutional operator is defined as follows:

$$\mathbf{x}_i^{'} = \mathbf{\Theta}_1 \mathbf{x}_i + \sum_{z=1}^{Z} \mathbf{\Theta}_2 \sum_{j \in \mathrm{N}(i)} e_{j,i,z} \cdot \mathbf{x}_j \tag{1}$$

Where $\mathbf{x}_\mathbf{i}^{'}$ denotes the features of the node i after convolution, $\mathbf{\Theta}_1$ and $\mathbf{\Theta}_2$ denote the trainable network weights. $\cdot$ is the multiply operator. $e_{j,i,z}$ represents the z th edge feature from the source node j to the target node i. $j \in \mathrm{N}(i)$ denotes all indices of nodes j connecting to the node i with nonzero edge features. Z denotes the size of latent edge features.

The graph embedding operator is defined as follows:

$$\mathrm{G}^Z = \sum_{i=1}^{N} \Theta \mathbf{x}_i \tag{2}$$

Where G^Z denotes the graph embedding of the size Z of all nodes of the graph. $\mathbf{\Theta}$ denote the trainable network weights. N denotes the number of nodes in the graph. Z denotes the size of latent node features.

Random edge drop was applied to augment data during training. The weighted loss was applied in the network to mitigate the effect of data imbalance. Learning rate decay was used to stabilise the training process. Early stopping mechanism, weight decay, and dropout layers after fully connected layers were used to prevent over-fitting.

4.3.5 Benchmark models

We adopted a three-dimensional Densely Connected Convolutional Network (3D-DenseNet) (Figure 4.2A) and a three-dimensional convolutional neural network (3D-CNN) (Figure 4.2B) as the benchmarks. Specifically, a classic 121-layer version of 3D-DenseNet follows the architecture described in (Liang et al., 2018) while a traditional 3D-CNN with four hidden convolutional layers with batch normalisation and pooling was applied, followed by a max-pooling layer and an output layer. Data were split using the same method as the GNN model. Weighted loss, learning rate decay, and early stopping are all applied, which was similar to the GNN settings. The same loss function and optimiser were applied to the benchmark models as the GNN model. Two experiments with different input were conducted: whole-brain MRI and MRI voxels inside tumour ROIs (contrasting-enhancing tumour core and necrosis) which are generated according to (Bakas et al., 2017)

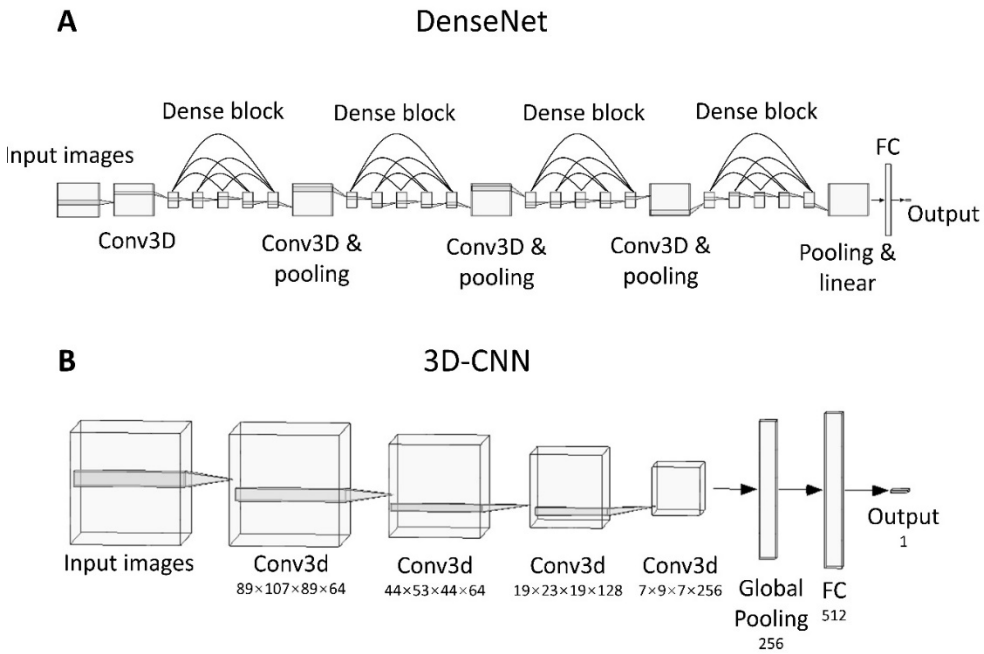


Fig. 4.2. Architecture of the benchmark models. A. Classic three-dimensional Densely Connected Convolutional Networks (3D-DenseNet) consist of four convolutional layers and

four densely connected blocks. **B**. Three-dimensional convolutional neural networks (3D-CNN) consist of four hidden convolutional layers with max-pooling and batch normalisation, one global pooling layer followed by dropout, and one fully connected dense layer.

4.4 Results

4.4.1 Model performance

Our experiments show that the proposed model performs better than the baseline models (Table 4.1) for both cross-validation and testing. Interestingly, the benchmark models with tumour voxels as inputs perform better than the models with the whole brain as inputs, which suggests the potential bias from the extensive brain regions beyond the local tumour. Of note, our proposed GNN model, leveraging the brain network generated based on prior atlas and whole brain MRI, performs better than all the benchmark models, which may suggest that incorporating prior knowledge of brain networks could help the deep learning models capture more informative features regarding tumour invasion over either the local tumour or the whole brain.

Table 4.1. Performances of IDH prediction models

Methods	**Accuracy** (%)	**Sensitivity** (%)	**Specificity** (%)
	Train		
3D-CNN + whole brain MRI	69.1	61.2	72.1
3D-CNN + tumour ROIs	80.1	77.7	81.0
3D-DenseNet + whole brain MRI	76.1	67.0	79.6
3D-DenseNet + tumour ROIs	84.1	86.4	83.3
GNN + brain networks	87.9	97.4	88.1
	Test		
3D-CNN + whole brain MRI	67.2	63.1	68.8
3D-CNN + tumour ROIs	78.2	75.7	79.2
3D-DenseNet + whole brain MRI	73.1	63.1	77.0
3D-DenseNet + tumour ROIs	83.3	83.5	83.2
GNN + brain networks	86.6	87.7	86.3

4.4.2 Model interpretation

To interpret the learning process of the GNN model, we applied the GNNExplainer (Ying et al., 2019). GNNExplainer outputs a probability score that infers the importance of the edges in the prediction task and outputs a compact subnetwork of the networks. The task was achieved by maximising both a graph neural network's prediction and distribution of possible subnetworks. Only subnetworks with edges that have probability scores greater than 50% were retained.

Overall, we observe that the IDH wild-type is associated with a wider distribution of edge invasion, captured by the GNN model. Figure 4.3 presents two typical cases of IDH mutant and wild-type, respectively, which also present the distribution of key white matter

tracts (edges) that are important to the prediction accuracy. In line with our prior knowledge that IDH wild-type generally causes more widespread invasion, the results of the model interpretation could further support the usefulness of the proposed GNN model.

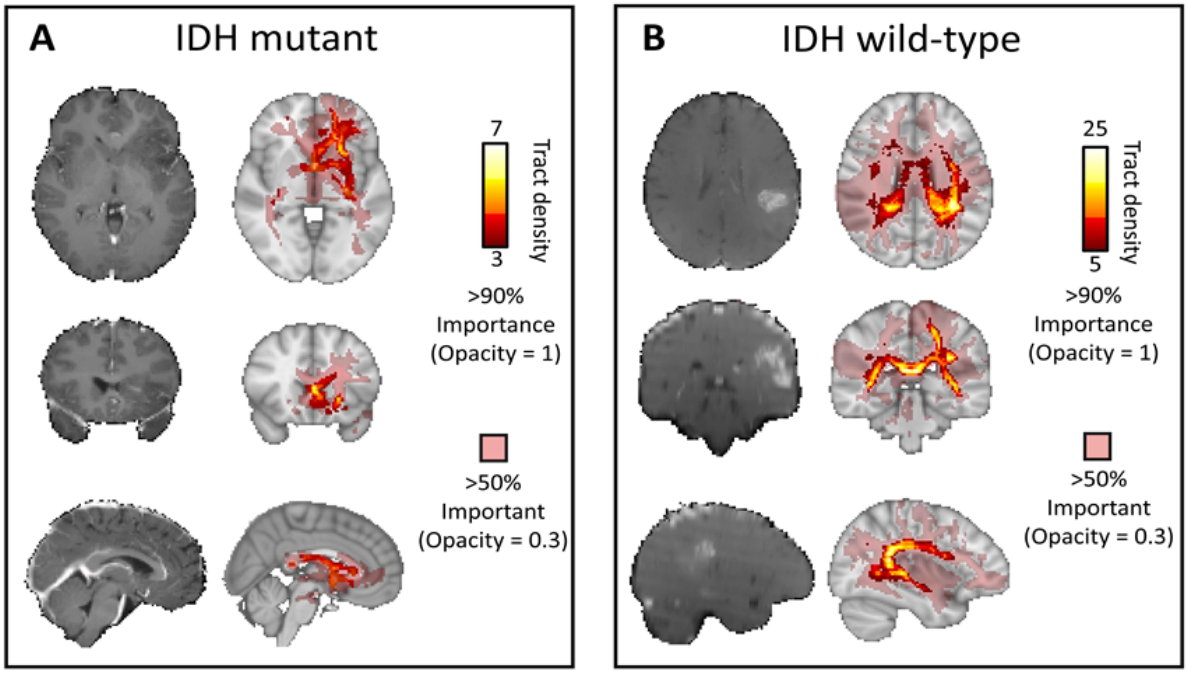


Fig. 4.3. Examples of IDH mutant and wild-type. An IDH mutant **B**. IDH wild type. For both patients, the left panels indicate the T1-weighted images, and the right panels show the output of GNNExplainer, illustrating the voxel distribution of edges that have over 50% and 90% probability of importance in IDH mutation prediction. The tract density of a voxel is defined as the number of tracts crossing the voxel.

4.5 Discussion

We proposed a preliminary method to construct structural brain networks with multimodal anatomical MRI and predict the IDH mutation status using graph neural networks. This study is inspired by the conclusion from previous clinical research in Chapter 3, which showed that the structural brain networks are sensitive to the impact of brain tumours beyond lesions. Hence, we constructed a model that learns from ROIs defined by a prior anatomical

connectivity atlas instead of the conventional tumour region ROIs.

One advantage of our method is it proposed a more convenient way to construct brain networks compared to the traditional approach which requires diffusion-weighted imaging. Additionally, by applying visualisation tools (e.g. GNNExplainer) of graph neural networks, clinical interpretation could be generated, which has the potential for medical applications such as assisting surgical planning.

Our method has several limitations. There is no ground truth for structural brain networks, hence we could not determine whether our feature-based brain networks reflect the true brain connectivity, It is also possible that our so-called brain networks just reflect the feature extracted from extended ROIs of tumour regions. Further, this method requires complex pre-processing including deformable registration of tumour-bearing MRI to standard space MRI. If the co-registration has an error, the downstream steps would be severely affected. Hence, the approach requires a manual check on each result of co-registration, which limits its potential to apply to large datasets. Finally, since this is preliminary work to test the feasibility of constructing brain networks from anatomical MRI, we did not compare it with sufficient published SOTA models in this Chapter. **In Chapter 5**, we will compare SOTA models with IDH status prediction.

4.6 Conclusion

In this paper, we propose a method to generate brain networks based on multimodal MRI and predict the IDH mutation status using GNN and the generated brain networks. Numerical results demonstrate that the proposed method outperforms benchmark methods. In future work, we could use the radiomic approach to extract representative features from the node and edge ROIs. Furthermore, special end-to-end GNN models could be developed to directly take the high-dimensional multi-modal MRI voxels as inputs.

To conclude, this chapter validated the third hypothesis proposed in **Chapter 1.4.2,** that

it is feasible to construct brain networks from anatomical MRI and anatomical priors by using deep learning feature extraction. We also discovered that models that learn from brain networks could better predict genotypes of gliomas than models that only learn from tumour images. Combining brain networks with GNN promises to serve as a powerful novel tool for deep learning models developed in radiogenomic studies.

Chapter 5 Multi-modal learning for predicting the genotype of glioma

This chapter is based on the following journal publication

Wei, Yiran, et al. "Multi-modal learning for predicting the genotype of glioma." IEEE Transactions on Medical Imaging (2023).

5.1 Abstract

The significance of predicting IDH mutation using MRI has been discussed in **Chapters 1 & 4.** In this study, we propose a novel multi-modal learning framework to predict IDH mutation using three separate encoders to extract features of focal tumour image, tumour geometrics and global brain networks. To mitigate the limited availability of diffusion MRI, we develop a self-supervised approach (**similar to Chapter 4**) to generate brain networks from anatomical multi-sequence MRI. Moreover, to extract tumour-related features from the brain network, we design a hierarchical attention module for the brain network encoder. Further, we design a bi-level multi-modal contrastive loss to align the multi-modal features and tackle the domain gap at the focal tumour and global brain. Finally, we propose a weighted population graph to integrate the multi-modal features for genotype prediction. Experimental results on the testing set show that the proposed model outperforms the baseline deep learning models. The ablation experiments validate the performance of different components of the framework. The visualised interpretation corresponds to clinical knowledge with further validation. In conclusion, the proposed learning framework provides a novel approach to predicting the genotype of glioma.

5.2 Introduction

This chapter is designed to test the fourth hypothesis proposed in **Chapter 1.4.2. N**amely, multi-modal data might reflect the different views of the same tumour's invasiveness. Hence

multi-modal learning could better characterise tumours to predict the genotypes.

5.2.1 Background and contributions

As I discussed in **Chapter 1**, glioma is characterised by remarkable heterogeneity and diverse survival outcomes (Louis et al., 2016). I introduced in **Section 1.1.2** that the isocitrate dehydrogenase (IDH) gene mutation is one of the most significant molecular markers for the diagnosis and prognosis of glioma (Louis et al., 2016). In clinical practice, the most commonly used approaches to determine IDH mutation status, i.e., immunohistochemistry and gene sequencing, rely on tumour samples, which, therefore, cannot be assessed on those patients who are unsuitable for tumour resection or biopsy. Further, as sequencing assays are usually time-consuming and expensive, they are unavailable in all institutions (Louis et al., 2016).

As I mentioned in **Section 1.2**, MRI is the mainstay for managing glioma patients, serving as a routine tool to characterise brain tumours. An increasing number of studies show that MRI can predict the genotype of glioma (e.g. IDH mutations) using machine learning or deep learning models, with a unique non-invasive advantage over the conventional invasive approaches relying on tumour tissue.

Deep learning has achieved better performance than the radiomics approaches based on machine learning models (Liang et al., 2018). For instance, recent studies show that the geometric data describing tumour shape provide robust tumour phenotyping across multiple tissue histology and imaging modalities. However, most deep learning models are based on convolutional neural networks (CNN), which cannot leverage the information in non-Euclidean data modalities. In addition, glioma tends to invade the whole brain beyond the focal tumour.

As I reported in **Chapter 3 and 4,** characterising the global brain using the network approach has shown significance in predicting survival and cognitive decline in brain tumour patients. Hence, integrating these multi-modal data, i.e., tumour image, tumour geometrics, and global brain network, could enhance glioma genotype prediction.

Multi-modal learning shows excellent performance to integrate multiple data modalities

while minimising the domain gap between them. For example, cross-modal attention is shown able to align the fine-grained features between modalities (Lee et al., 2018).

Additionally, cross-modal contrastive loss shows promising performance in extracting global representations from images and the corresponding texts (Y. Zhang et al., 2020). Nonetheless, most multi-modal learning methods are designed for the data modalities independent of each other, which may not suit data modalities with geometric relation, i.e., tumour images reflect localised features of the focal tumour, while brain networks contain information from the whole brain. A multi-modal learning scheme which can effectively learn the geometric inter-relation of focal tumor and global brain could better help characterise tumor invasion that widely affects the whole brain.

This study develops a novel learning framework tailored to characterise brain tumours and predict genotypes (e.g. binary classification of IDH status: mutations vs wild-types) in glioma. Specifically, we design a self-supervised approach to construct brain networks from anatomical MRIs apart from the image and geometric data derived from the segmentation masks. Then, we develop three separate encoders to extract multi-modal features. In particular, hierarchical attention is designed to assist the brain network encoder in feature extraction. Afterwards, we design a bi-level multi-modal contrastive loss to tackle the domain gap between the focal tumour and the global brain. Finally, we construct a weighted population graph that models the patient cohort based on multi-modal features. A graph neural network (GNN) is trained to classify patients.

Our contributions include:

a) Structural brain networks are conventionally constructed from diffusion MRI. To mitigate the limited availability of diffusion MRI, we propose a self-supervised approach of contrastive representative learning to reconstruct the edge attributes of the brain network from anatomical MRI, which could help to map the domain knowledge from diffusion MRI to anatomical MRI.
b) To allow the brain network encoder to extract the most relevant brain network features and reduce the confounding effect from concomitant pathology, we design a hierarchical attention module that sequentially attends to the edges and nodes of the

brain network for identifying network features associated with the focal tumour.

c) To reflect the gradient tumour invasion and tackle the domain gap across the focal tumour and global brain, we present a bi-level contrastive loss, which firstly aligns tumour-level features (i.e., focal tumour image and geometric points cloud) and then further aligns the tumour-level features with the brain-level network features.

d) To better integrate multi-modal features and characterise the patient cohort, we construct a population graph for modelling the patient cohort with multi-modal data. The weighted nodes represent the multi-modal features of individual patients, while the weighted edges represent the continuous similarity between patients.

To highlight, we incorporate the domain knowledge of neuroscience and neuro-oncology into the model design. To our best knowledge, this is the first multi-modal learning method based on tumour image, tumour geometrics, and brain networks, to characterise tumour invasion.

5.2.2. Related work

5.2.2.1 Genotype prediction

Compared to **Chapter 4**, this Chapter presented more comprehensive published baselines. The studies of predicting glioma genotypes consist of radiomics-based machine learning methods and deep learning methods. The radiomics-based machine learning approaches first extract hand-crafted features from the tumour core. Feature selection is performed before training models for predicting the genotype (Bhandari et al., 2021). For example, Gihr et al. successfully used intensity-based radiomics features to predict IDH mutation with reasonable accuracy (Gihr et al., 2020) However, the reproducibility and generalizability of radiomics are often limited by the nonstandard feature engineering and selection procedure. The end to-end deep learning models, i.e., ResNet, and DenseNet, provide a more robust prediction for tumour genotype over radiomics approaches (Ahmad et al., 2019; Chang et al., 2018; Liang et al., 2018). Liang et al. used a 3D-DensNet to predict the IDH mutation, establishing the feasibility of CNN predicting the glioma genotype (Liang et al., 2018). Other deep learning models incorporate radiomics features into the model. Choi et al. integrated radiomics

features into the later layers of CNN to enhance prediction (Choi et al., 2020), which outperforms the conventional ResNet. Despite achieving reasonable performance, the CNN-based models may not learn the information encompassed in the non-Euclidean data, e.g., geometric points cloud and brain networks, which provide crucial tumour biology and neuroscience information. Hence, we propose specialised encoders to obtain features from multi-modal data.

5.2.2.2 Structural brain networks in glioma

As discussed in **Chapter 1.3.1**, most studies use the approach based on diffusion MRI to generate structural brain networks, which promises to indicate subtle tumour invasion. However, robust model training is significantly limited by the data availability of the diffusion MRI. Recent studies indicate that the scalar map of diffusion MRI can be successfully generated from a single anatomical T1 sequence (Gu et al., 2019), which suggests the high-level correlation between anatomical MRI and diffusion MRI, indicating the potential of constructing brain networks using anatomical MRI. However, a single T1 sequence is insufficient to characterise the heterogeneous structural alternation caused by glioma invasion. Therefore, we proposed reconstructing edge attributes by transferring the knowledge of diffusion MRI to multi-sequence MRI using a contrastive loss. Studies of diffusion-based brain networks generally only include edge attributes. To characterise the brain regions invaded by glioma, we further develop an autoencoder approach to reconstruct node attributes based on regional multi-sequence MRI.

5.2.2.3 Multi-modal learning

Multi-modal learning is the deep learning approach that learns from more than one data modality, e.g., images, text, points cloud. Multi-modal learning has shown promising performance in a series of learning schemes. Lee et al. proposed stacked cross attention to discover the full latent alignments between image regions and words in a sentence. By inferring image-text similarity, the model produced interpretable prediction results (Lee et al.,

2018). Zhang et al. employed a contrastive loss between the lung X-ray and corresponding medical reports to extract relevant representations from both images and text (Zhang et al., 2020). Nevertheless, existing methods are not designed for data modalities with inclusion relation, e.g., focal tumour and global brain. Therefore, we propose a bi-level contrastive loss to align the features from the focal tumour and global brain levels.

5.2.2.4 Graph neural networks

The background of GNN and the advantages of GNN in learning brain networks were discussed in **Chapter 1.3.3**. In this Chapter, GNN is further applied to learn from geometrics and perform classification on population graphs.

The fast-developing graph neural network (GNN) family promises to extract features and learning from the geometric data, e.g., points cloud, which can be readily reconstructed from MRI (Qi et al., 2017). For example, Qi et al.(2017) proposed hierarchically generating a graph of points cloud and recursively trained a GNN, which effectively learned local features from the geometric points cloud of the objects.

Further, brain networks are naturally learnable by the GNN due to the graph format. Based on brain networks, GNN has shown high performance in classifying diseases. Ma et al. proposed a combination of recurrent neural networks and GNN with an attention-guided random walk module to extract longitudinal structural graph theory features from the brain network for patient classification (Ma et al., 2020). The results showed that the attention mechanism could reveal the most critical brain regions and temporal domains during AD progression. Nonetheless, the attention mechanism designed for other diseases may not suit glioma due to its distinct pathophysiology. We thus developed a hierarchical attention module that could attend to the brain structure to reduce the confounding effect from concomitant pathology and capture tumour-specific features.

Finally, GNN also shows high performance in classifying the nodes in a large graph such as citation networks (Cabanes et al., 2013). The capability of GNN in handling large graphs could be transferred to patient classification tasks. Parisot et al. proposed a population graph to model the dementia cohort by regarding imaging features of individual patients as

nodes, while the clinical similarity between patients as edges (Parisot et al., 2018). A GNN is trained to classify patients, outperforming traditional machine learning models, e.g., random forest. This study develops a population graph to integrate the multi-modal features. Additionally, we permute the edge and node weights to select the best combination for constructing the population graph.

5.3. Methods

5.3.1 Methodology

5.3.1.1 Study Overview

The proposed prediction model includes three stages: (Fig.5.1): (1) generating multi-modal data of tumour image, tumour geometrics and brain networks from the multi-sequence MRI; (2) multi-modal contrastive learning extracting features from focal tumour image, geometrics and global brain networks; (3) feature integration to construct a population graph for patient classification and genotype prediction.

In this study, we introduced two types of graph data: brain network and population graph. To distinguish the features extracted from the two types of graphs, we define the features from brain networks as attributes and features from the population graph as weight. The superscript E/N only denotes the brain network edge/node in this study. In addition, node embedding represents the aggregated node features during the graph convolution of brain networks. We present the glossary of notations in Table 5.1.

Table 5.1 Glossary of notations

Glossary of notations	
Notation	Definition
$x^I; x^P; x^B$	Input image; Input points cloud; Input brain networks
$i; j; k; m; n; M$	Target patient index; Other patient index; Point index in points cloud; Target node index; Other node index; Minibatch size
Multi-modal data generation	
$b^N; b^E; b^{E'}$	Attribute of brain regions/nodes; Attribute of brain edges from anatomical MRI; Attribute of brain edges from FA
$g^E(\cdot); g^{E'}(\cdot);$	Projection head for brain edge attribute extracted from anatomical MRI; Projection head for brain edge attribute extracted from FA;
$z^E; z^{E'}$	Latent feature for anatomical MRI extracted attribute; Latent feature for FA extracted attribute.
$\mathcal{L}_E$	Contrastive loss for extracting brain connection attributes.
Multi-modal contrastive learning	
$f^I(\cdot); f^P(\cdot);$	Image encoder; Geometric encoder
$u^I; u^P; u^B; u^F$	Image features; Geometric features; Brain network features; Focal tumor features
$a^P; a^E; a^N$	Geometric points attention, Brain network edge attention, Brain network node attention
$f^{B'}(\cdot); z^B$	Brain network encoder before pooling; node embedding of brain networks;
$g_a^N(\cdot); g^F(\cdot);$	Projection head of node embedding; Projection head of focal tumor features concatenated from image and geometrics
$g^I(\cdot); g^P(\cdot); g^B(\cdot); g^F(\cdot);$	Projection head for: image features; geometric features; brain network features; focal tumor features
z_m^N	Node embedding of mth node in brain networks
$z^I; z^P; z^B; z^F;$	Latent feature of: image; geometrics; brain networks; focal tumor
$l^{I2P}; l^{P2I}; l^{B2F}; \mathcal{L}_{multi}$	Contrastive loss from image to geometrics; Contrastive loss from geometrics to image; Contrastive loss from brain networks to focal tumor; Multi-modal contrastive loss
Population graph	
$w^{edge}; w^{node}$	Edge weight of population graph; Node weight of population graph

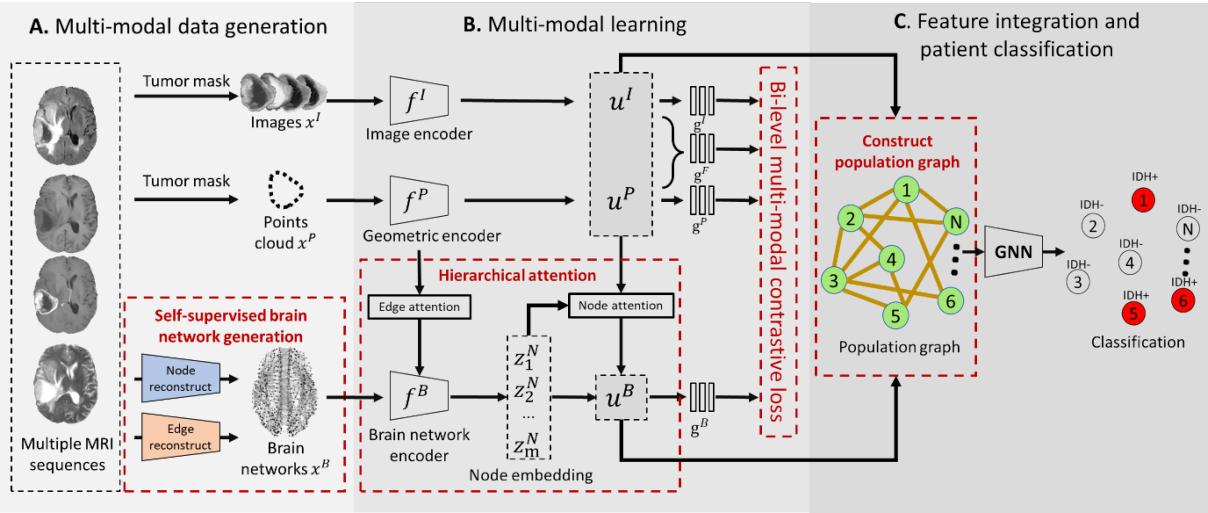


Fig. 5.1. Study overview: A. Multi-modal data generation. Image x^I and geometric x^P data are generated from tumour masks, while brain network data x^B are generated from the pretrained self-supervised models. **B.** Features of tumour image (u^I), tumour geometrics (u^P), focal tumour $u^F = \langle u^I, u^P \rangle$ and global brain network (u^B) are projected by respective projection heads (g^I, g^P, g^F and g^B) for bi-level contrastive learning. The hierarchical attention module attends to the edges and nodes in the brain network. **C.** A population graph is used to integrate multi-modal features and classify patients using a GNN

5.3.1.2 Multi-modal data generation

Our method starts by generating three data modalities from the input multiple MRI sequences (see Fig. 5.1A), and the three data modalities are: (1) the image data of the focal tumour (denoted as x^I) is obtained by assigning Boolean values on the tumour masks and the MRI; (2) the tumour geometric data (denoted as x^P), in the form of points cloud, is generated by sampling the surface meshes of tumour masks using a standard farthest point sampling strategy; and (3) the brain networks (denoted as x^B) are generated by two self-supervised neural networks (NNs) detailed below.

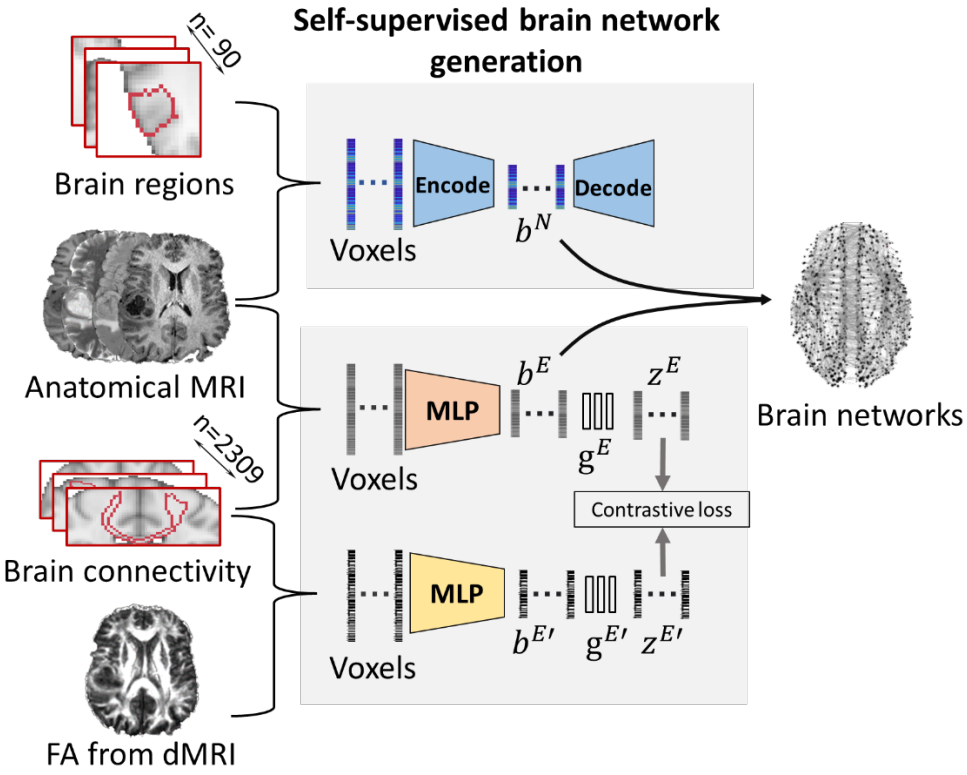


Fig. 5.2. Brain network generation. Two self-supervised models are trained to extract node/edge attributes (b^N, b^E) from node/edge atlas bounded MRI voxels: Node attributes are extracted by the autoencoder, while edge attributes are reconstructed through contrastive learning between anatomical MRI and FA map of dMRI using projection head $(g^E, g^{E'})$, projected latent features $(z^E, z^{E'})$ and a contrastive loss L_E

1) Brain networks construction via self-supervised NNs:

The brain networks, consisting of reconstructed nodes and edges, are generated based on a prior neuroanatomy atlas (Fig. 5.2).

In this study, we denote the edges and nodes of brain networks as attributes of edges b^E and attributes of nodes b^N. The brain node attribute is defined as the features extracted by the pre-trained node autoencoder from the anatomical MRI regions defined by the anatomical atlas. The node attribute represents the independent regional features of the separated brain areas. The brain edge attribute is defined as the feature extracted by the pre-trained edge encoders from the anatomical MRI representing the white matter tract connectivity across

different brain regions defined by the anatomical prior. As shown in the upper half of Fig 5.2, the anatomical MRI is the only input to the autoencoder for reconstructing the node attributes at both the training and testing phases. The trained encoder extracts node attributes from the prior brain atlas (as the nodes of the brain network). Specifically, voxels enclosed by the 90 cortical/subcortical brain regions on the atlases (Tzourio-Mazoyer et al., 2002) are extracted and fed into an NN-based autoencoder (AE) to produce the brain node attributes a^N of the brain networks. The AE consists of a NN encoder that extracts high-level representation vectors from the voxels in the brain node and a NN decoder that attempts to restore the voxels from the representation vectors. By adopting this self-supervised model, representations of the voxels in the brain regions could be extracted as brain node attributes. In contrast, the input to the contrastive learning encoders (MLP) for the edge attributes includes both FA maps and anatomical MRI in the training stage, whereas the FA maps and the corresponding encoder are no longer needed in the testing stage. The trained encoder of anatomical MRI extracts edge attributes from the tract atlas (as the edges of the brain networks). Particularly, we use the tract atlas as the regions of interest for reconstructing brain edge attributes b^E (Wei et al., 2021), indicating the 2,309 pathways of white matter tracts connecting the 90 brain regions. Due to the clinical significance of the fractional anisotropy (FA) map derived from the diffusion MRI in characterising brain connectivity/edge, we utilise the FA map to guide the attributes extraction of anatomical MRI. Firstly, voxels of anatomical MRI and the corresponding FA map enclosed by the tract atlas are input into two multilayer perceptron (MLP), which respectively extract the attribute vectors b^E $b^{E'}$ from voxels. Next, two projection heads $g^E(\cdot)$ $g^{E'}(\cdot)$ project the attributes to a common latent space, where domain alignment is performed between the latent attributes of anatomical MRI ($z^E = g^E(b_n^E)$) and FA ($z^{E'} = g^{E'}(b_n^{E'})$) using a contrastive loss. The brain edge attributes extracted from the anatomical MRI would contain corresponding information in the FA map. The contrastive loss for the brain edge L_E is defined as:

$$\mathrm{L}_E = \frac{1}{M}\sum_{i=1}^{M}\left(-\log\frac{\exp(S(z_i^E, z_i^{E'})/\tau)}{\sum_{j\neq i}^{M}\exp(S(z_i^E, z_j^{E'}))/\tau)}\right) \quad (1)$$

where i is the index of target patients, while j is the index of other patients in the minibatch M; $S(\cdot)$ is the similarity score; τ is the temperature parameter setting to 0.1; M is the size of the minibatch. The negative pair is the edge attribute pair (FA, anatomical MRI) of different patients, whereas the positive pair is the edge attribute pair of the same patient. The loss maximises the distance between the positive pair and minimises the distance between the negative pair to extract the most FA-relevant features from anatomical MRI.

The node and edge attributes are independent features linked together according to the prior anatomical connection for constructing the brain network: $x^B = \{b^E, b^N\}$.

5.3.1.3 Multi-modal learning for image, geometrics and brain networks

The proposed multi-modal learning framework extracts features from the three modalities of data, i.e., focal tumour image, focal tumour geometric, and global brain networks. Moreover, hierarchical attention is developed for the brain network encoder to extract tumour-related brain network features. Finally, the extracted features are projected into a shared latent space for bi-level multi-modal contrastive learning, which could minimise the domain gap from the tumour level (image and geometrics) across the global brain level (focal tumour and brain networks). As shown in Fig. 5.1B, the projection is conducted via three NN-based encoders as follows.

Image encoder:

The image encoder is a 3DCNN defined by $u_i^I = f^I(x_i^I)$, where x_i^I and u_i^I are the image data and output features for the ith patient, and $f^I(\cdot)$ is the 3DCNN model

Geometric encoder:

$f^P(\cdot)$ is defined as the geometric encoder (Fig. 5.3A) outputs the geometric features u_i^P and geometric attention $a_{i,k}^P$ for k th point in the points cloud, defined as $u_i^P, a_{i,k}^P = f^P(x_i^P)$ for the i th patient.

Brain network encoder with hierarchical attention:

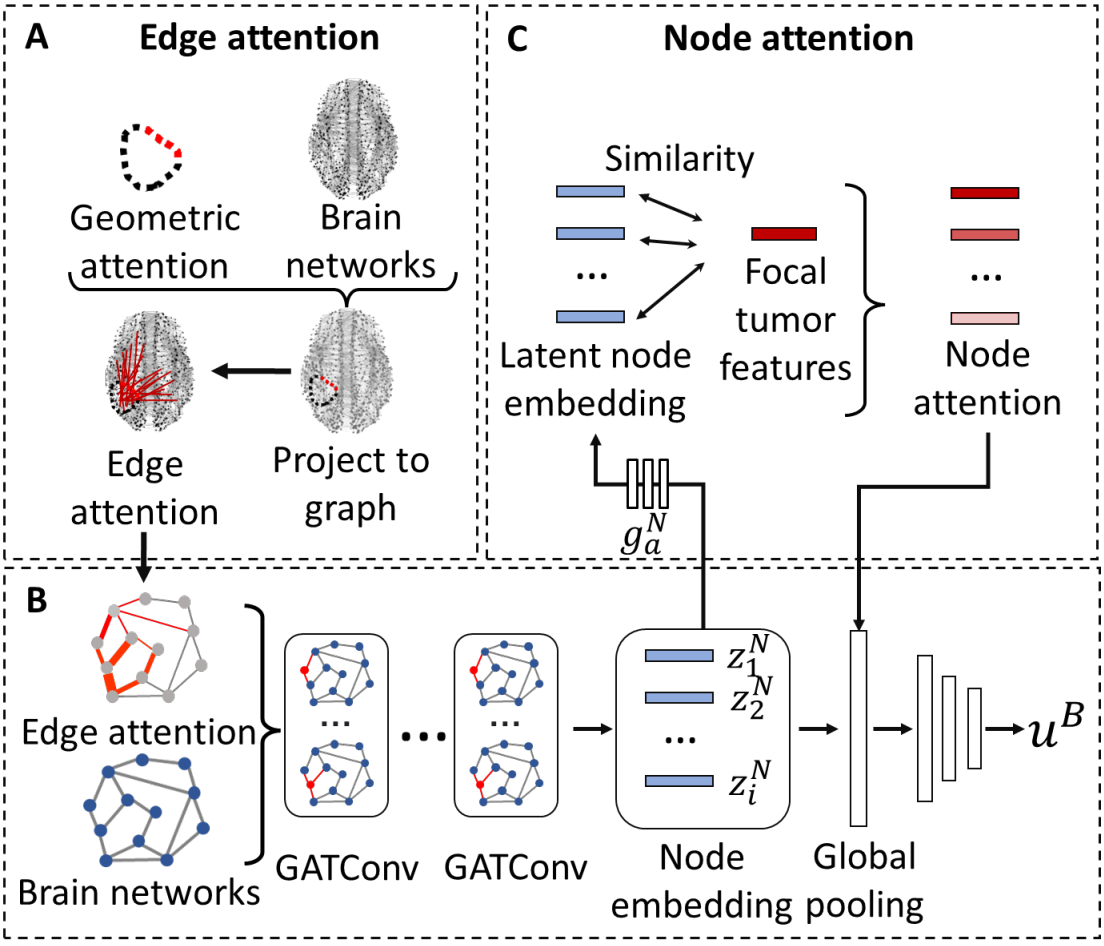


Fig. 5.3. Hierarchical graph attention: A. Geometric boundary attention produced by the geometric encoder is projected to brain networks to obtain edge-level attention. B-C. Edge-attended brain networks are convoluted to produce node embeddings, projected to latent space for generating node-level attention by computing similarity with tumour features. The node-level attention is then utilised in the global pooling level for generating tumour-related

brain-level network features u^B

Brain network features are extracted by training a NN with graph convolution layers, where the NN weights are corrected following a novel hierarchical attention mechanism.
The attention mechanism is structured by edge-level attention and node-level attention. The former is obtained by projecting the geometric attention of the tumour boundary onto the edges (Fig. 5.3B). Specifically, the points clouds are projected to the edge atlas. The crossing edges are then assigned with the boundary attention of the points cloud. The edge attention is defined as:

$$a^E_{i,(m,n)} = \frac{1}{K}\sum_{k}^{K}(a^P_{i,k}) \tag{2}$$

where $a^E_{i,(m,n)}$ is the edge attention of (m,n)th edge connecting mth node and nth node of the ith patient. K is the number of points in points cloud crossed by (m,n)th edge and $a^P_{i,k}$ is the attention of kth point crossed by the (m,n)th edge.

The outputs of the edge-level attention are further encoded by the GATConv layers that convolute the nodes and edges of the brain networks to obtain the node m embedding in the patient i defined by $z^N_{i,m} = f^{B'}(x^B_i)$, where $f^{B'}$ is the components of the brain network encoder before the global pooling layers (Fig. 5.3B). Afterwards, the node embeddings are projected to the latent space by a projection head g^N_a. To extract the tumour-related node embeddings, we applied another projection head g^F to project the concatenated focal tumour features of ith patient: $u^F_i = \langle u^I_i, u^P_i \rangle$, composed by both images and points cloud, into the latent space shared with node embedding. We measure the similarity between the mth node embedding with the tumour features of ith patient by:

$$a^N_{i,m} = S(g^N_a(z^N_{i,m}), g^F(\langle u^I_i, u^P_i \rangle)) \tag{3}$$

where $a_{i,m}^{N}$ is the attention of the m th node of i th patient. $z_{i,m}^{N}$ is the node embedding of m th node of i th patient. $g^{F}(\cdot)$ and $g_{a}^{N}(\cdot)$ are projection heads projecting tumour features (e.g., concatenated image and geometric features $\langle u_i^I, u_i^P \rangle$) and node embeddings to the same latent space; $S(\cdot)$ is the similarity function.

By performing attention in training the brain network encoder, we extract the most tumour-related features from the brain network and reduce the noise caused by confounding effects, e.g., ageing or other concomitant pathology (Fig. 5.3B). The feature extraction of the brain networks is defined as $u_i^B = f^B(x_i^B)$, where x_i^B and u_i^B are the brain network data and brain network features for the i th patient, and f^B represents the GNN-based brain network encoder.

Bi-level multi-modal contrastive loss:

We develop a bi-level multi-modal contrastive loss to further characterise tumour gradient invasion and minimise the domain gap between the focal tumour and the global brain. After extracting the multi-modal features from different encoders, two projection heads are adopted to respectively project the tumour-level features of images and points cloud to the same latent space: $z_i^I = g^I(u_i^I)$, $z_i^P = g^P(u_i^P)$ where z_i^I and z_i^P are the projected latent features of images and points cloud, g^I and g^P are the pre-defined projection heads.

Meanwhile, another two projection heads are employed to respectively project the extracted focal tumour features and brain network features into another latent space: $z_i^B = g^B(u_i^B)$, $z_i^F = g^F(u_i^I, u_i^P)$, where z_i^B and z_i^F are the projected latent feature of brain networks and focal tumour); g^B and g^F are the projection head for the brain network and focal tumour.

Subsequently, a bi-level multi-modal contrastive loss is developed to first reduce the domain gap of tumour-level features by minimising the cosine distance (attract) between the

multi-modal latent features (z_i^I, z_i^P) from the same patient i and maximising the cosine distance (repel) of multi-modal latent feature pairs (z_i^I, z_j^P), (z_i^P, z_j^I) from different patients i and j using contrastive loss. Secondly, the brain-level domain gap is optimised using a similar approach for the features of brain networks (z_i^B) and focal tumours (z_i^F).

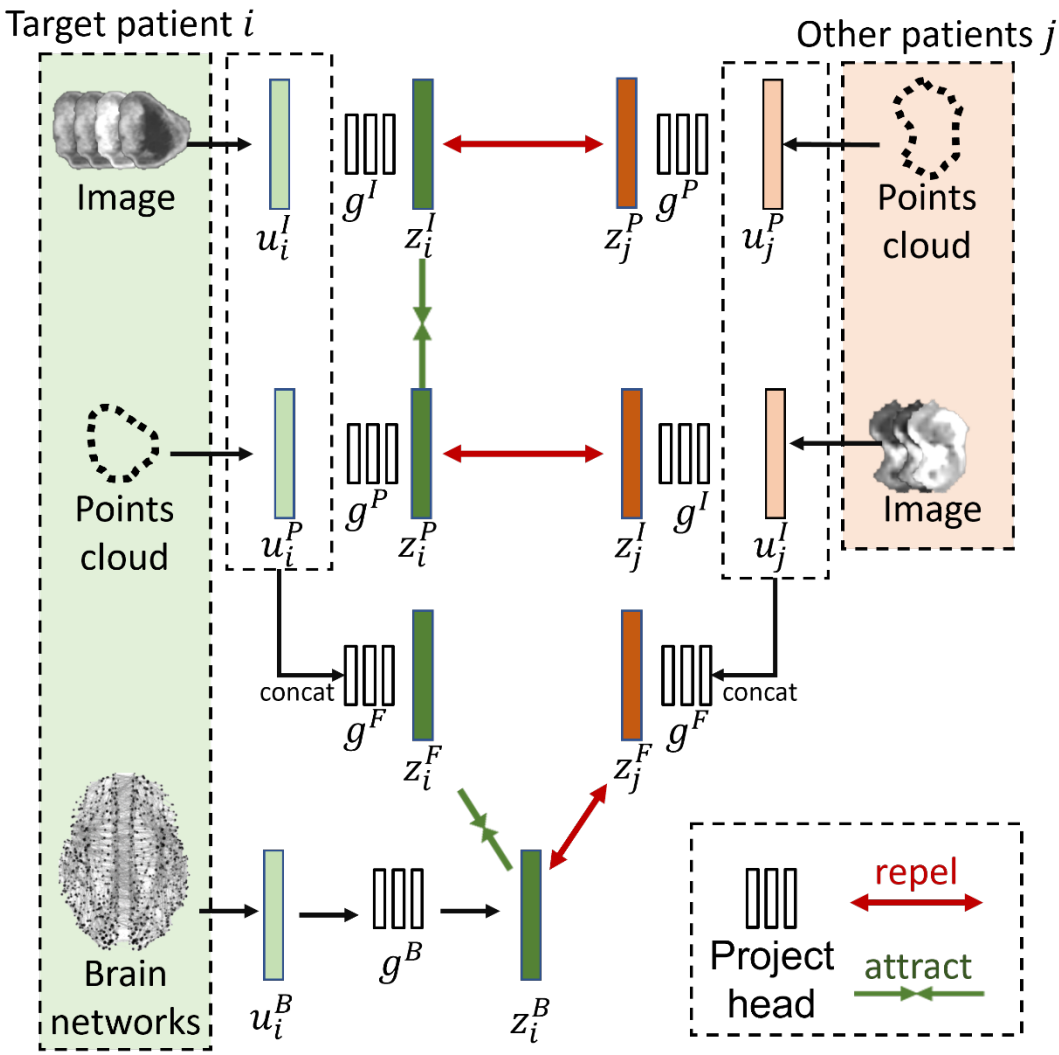


Fig. 5.4. Bi-level multi-modal contrastive learning: Latent features of different modalities (u_i^I, u_i^P), (u_i^F, u_i^B) from the same patient (green) attract each other, while latent features of different modalities (u_i^I, u_j^P), (u_i^F, u_j^B) f from different patients (red) repel each other. The bi-level loss consists of tumour-level and brain-level components trained together.

We design three contrastive losses for tumour image to tumour geometrics (Equation. 4), tumour geometrics to tumour image (Equation. 5) and global brain network to the focal tumour (Equation. 6). Finally, we integrate those three sub-losses with a weighting coefficient λ.

$$l_i^{I2P} = -\log \frac{\exp(S(z_i^I, z_i^P)/\tau)}{\sum_{j\neq i}^{M} \exp(S(z_i^I, z_j^P)/\tau)} \tag{4}$$

$$l_i^{P2I} = -\log \frac{\exp(S(z_i^P, z_i^I)/\tau)}{\sum_{j\neq i}^{M} \exp(S(z_i^P, z_j^I)/\tau)} \tag{5}$$

$$l_i^{B2F} = -\log \frac{\exp(S(z_i^B, z_i^F)/\tau)}{\sum_{j\neq i}^{M} \exp(S(z_i^B, z_j^F)/\tau)} \tag{6}$$

where i is the index of the target patient, and j is the index of other patients in the mini-batch; $S(\cdot)$ is the similar score function; τ is the temperature parameter (setting to 0.1) controlling the strength of penalties on negative examples. The positive pairs are defined as the modality pairs from the same patient, while negative pairs are defined as the modality pairs from different patients. M is the size of the mini-batch. l^{I2P} is the image to point cloud contrastive loss. l^{P2I} is the points cloud to image contrastive loss. l^{B2F} is the brain network to focal tumour contrastive loss. It's necessary to define different losses for different pairs of modalities because contrastive loss is asymmetric for each input modality (Zhang et al., 2020).

$$\mathrm{L}_{multi} = \frac{1}{M}\sum_{i=1}^{M}(\lambda(\frac{l_i^{P2I} + l_i^{I2P}}{2}) + (1-\lambda)l_i^{B2F}) \tag{7}$$

$\lambda \in [0,1]$ is a scalar weight coefficient. M is the minibatch size. The final multi-modal contrastive loss L_{multi} is computed as a weighted combination of three contrastive losses that

maximises the distance between the multi-modal features of the different patients and minimises the multi-modal features of the same patient.

The proposed multi-modal contrastive learning algorithm is shown in Algorithm 1

Algorithm 1: Multi-modal contrastive learning

Input: image: x_i^I, points cloud: x_i^P, brain network: x_i^B
for $i = 1, \cdots 270$ **do**
  Compute features and attention from image and geometric points cloud: $u_i^I = f^I(x_i^I)$;
  $u_i^P, a_{i,k}^P = f^P(x_i^P)$;
  Input edge attention: $x_i^{B'} = x_i^B \cdot a_{i,(m,n)}^E$ via (2).
  Compute node embedding using brain network encoder: $z_{i,m}^N = f^{B'}(x_i^B)$.
  for $m = 1, \cdots 90$ **do**
    Compute node attention $a_{i,m}^N$ via (3).
  end for
  Extract features from brain networks: $u_i^B = f^B(z_i^N \cdot a_{i,m}^N)$.
  Project features to latent space:
  - Image: $z_i^I = g^I(u_i^I)$
  - Points cloud: $z_i^P = g^P(u_i^P)$
  - Focal tumor: $z_i^F = g^F(\langle u_i^I, u_i^P \rangle)$
  - Brain networks $z_i^B = g^B(u_i^B)$

  Compute multi-modal contrastive loss by (7).
end for

5.3.1.4 Population graph for classifying glioma patients

With the focal tumour and brain network features generated from the multi-modal learning, we construct a population graph to characterise the patient cohort (Fig. 5.1C): each node represents the multi-modal features extracted from the patients, while each edge represents the similarity between the multi-modal features among the patients (Fig. 5.5). In the population graph, the node weight of the patient i is defined as $w_i^{node} = u_i$, and the edge weight between patient i and j is defined as:

$$w_{i,j}^{edge} = \begin{cases} r(u_i, u_j), & if\ r(u_i, u_j) \geq \theta \\ 0, & if\ r(u_i, u_j) < \theta \end{cases} \tag{8}$$

where $u \in \{u^F, u^B, \langle u^F, u^B \rangle\}$: u is the feature extracted from the multi-modal contrastive learning, and $r(\cdot)$ is the correlation operator. θ is the threshold of the correlation.

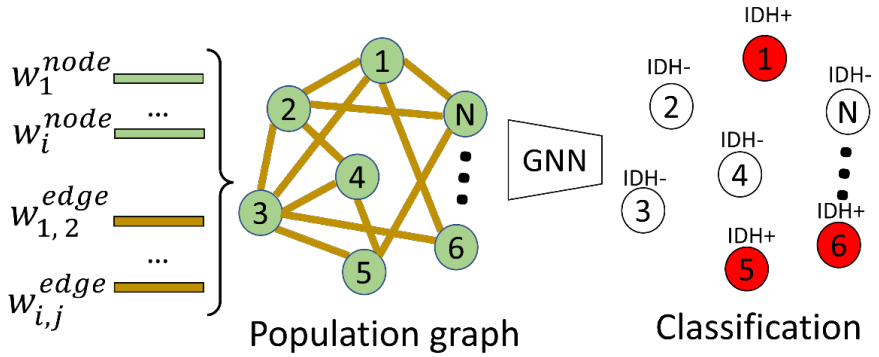


Fig. 5.5. Population graph for patient classification: Each node weight (w^{node}) represents features of one patient, while each edge weight (w^{edge}) represents the similarity among the features of patients. A GNN node classifier is trained for classifying patients.

We design five different combinations of the node weight w^{node} and the edge weight w^{edge} listed in Table 5.2.

Table 5.2 Population graph with different node and edge weight

Node weight	Edge weight
u^F	$r(u^B)$
u^B	$r(u^F)$
$\langle u^F, u^B \rangle$	$r(u^B)$
$\langle u^F, u^B \rangle$	$r(u^F)$
$\langle u^F, u^B \rangle$	$r(\langle u^F, u^B \rangle)$

Specifically, we consider different combinations of focal tumour features (tumour image and geometrics) and global brain network features as edge and node weight, and we construct the population graph based on the hypothesis that the two categories of features may reflect

different patterns of tumour invasion, i.e., localised v.s. widespread invasion. As such, we could integrate two types of features and characterise both the homogeneity and heterogeneity of the cohort.

5.3.2 Experiments

5.3.2.1 Datasets

We collect the anatomical MRI data of 407 glioma patients available from The Cancer Imaging Archive (TCIA) (Clark et al., 2013) and an in-house cohort. The cohort includes 105/407 (25.7%) IDH mutants and 302/407 (74.3%) IDH wild types. The MRI modalities include pre-contrast and post-contrast T1, T2, and T2-FLAIR.

A total of 20 patients of the in-house cohort are used for training the self-supervised models of brain network construction. The remaining 387 patients are split into training and testing sets with a 7:3 ratio. The training set of 270 patients is divided by half to train the bi-level multi-modal contrastive learning for feature extraction and population graph-based classifier for patient classification. The testing set includes 117 patients from the publicly available TCIA website. For baselines, we used the training data of 270 patients to train the models. We then evaluated the trained models with independent testing data from 117 patients.

5.3.2.2 Image pre-processing

The preprocessing of anatomical MRI (T1, T1C, T2, FLAIR) follows the same pipeline in Chapter 4.3.2.

For the in-house cohort with diffusion MRI modalities available, the FA maps are derived from the diffusion MRI using the FMRIB's Diffusion Toolbox. The FA maps are used to train the self-supervised models to extract tract-related features from the anatomical MRI to generate brain networks.

The tumour mask is generated from the following steps: we first generate an initial tumour segmentation (auto-mask) using a pre-trained nnUNet (Isensee et al., 2021), which is then inspected by two clinical experts. The segmentation errors of the initial results are manually corrected. The final resulting mask is then taken as the ground-truth segmentation mask used in our experiments. We follow the standard annotation procedures of the multimodal brain tumour segmentation (BraTS) benchmark reported by (Menze et al., 2014).

5.3.2.3 Implementation details

Brain network generation

The 20 patients yield 46,180 edges and 1,800 nodes for training the self-supervised model. For the node autoencoder, all input node voxels are sampled to the dimension of 4,000, the encoder consists of six layers (dimensions 2048, 1024, 512, 128, 32, 16), and the output of the bottleneck is the attribute feature b^N with a dimension of 16. For the edge encoder, all input edge voxels are sampled (Anatomical: 4000, FA: 1000). Two MLP (MRI: 2048, 1024, 512, 128, 32, 16; FA: 1024, 512, 128, 32, 16) respectively encode the voxel vectors of T1 and FA to attribute vectors b^E and $b^{E'}$ with a dimension of 16. The final brain networks contain 90 nodes and 2,309 edges with a dimension of 16.

Image encoder

The image encoder is a 3DCNN architecture consisting of five 3D convolutional layers (dimensions 64, 128, 128, 256, 256), with four input channels corresponding to the four MRI sequences. Batch normalisation and max pooling are performed for all convolutional layers. Three feed-forward layers (dimensions: 512, 256, 32) are followed to output features with a dimension of 32.

Geometric encoder

A specialised GNN is adopted to extract features from the points cloud. The points are first converted into a graph for each convolution by generating links between points and their nearest neighbours within a predefined radius distance. Secondly, convolution operators NNConv (Fey & Lenssen, 2019) aggregate the points features (Euclidean coordinates of points) and the link features (distance between points) to the centre node.

Finally, the farthest points sampling is adopted to sample the points with the furthest distance from other points. Our geometric encoder consists of convolutional layers (dimensions: 32, 64, 64, 128, 128). After the last layer, global attention pooling is employed to produce attention scores for the points. Finally, a feed-forward network (dimensions: 256, 128, 32) outputs the geometric features with a dimension of 32.

Brain network encoder

The projection head g_a^N for node attention is NNs (dimension: 16, 32, 64, 128) that projects node embeddings to the latent space shared with focal tumour features z^F.

The brain network encoder is a graph attention network with GATConv layers (dimensions: 64, 128, 128, 256, 256, 256) that can handle the high-dimensional node and edge attributes (Veličković et al., 2017). The feed-forward network outputs the brain network features (dimensions: 512, 256, 32). Cosine similarity is used as the similarity score $S(\cdot)$ for generating node attention.

Bi-level multi-modal contrastive loss

The projection heads g^I, g^P and g^B, are three separate NNs (dimensions 32, 64, 128, 128) that project the features to the latent space with the dimension of 128. The projection head g^F is another NN (dimension 64, 64, 128, 128) that projects $\langle u^I, u^P \rangle$ to the latent space with a dimension of 128.

Cosine similarity is selected as the similarity score $S(\cdot)$. τ is set to 0.1 λ is set to 0.8.

Population graph and GNN classifier:

θ of the population graph is set to 0.5. The GATConv is employed as the graph kernel of the GNN to perform node classification in the population graph. The GNN for the population graph consists of layers of GATConv (dimensions: 64, 128, 128, 128) followed by pooling layers and a classification layer.

Training parameters:

For self-supervised learning for generating brain networks, the autoencoder adopts mean squared error loss (MSELoss), the Adam optimiser with a weight decay of 0.0005 and a batch size of 50. We implement the following hyperparameters: 1000 training epochs. We set the initial learning rate as 0.001, and the learning rate is reduced to 90% after every 50 epochs. For edge reconstruction, we adopt the SGD optimiser with a weight decay of 0.0005 and a batch size of 50 with 1000 training epochs. We set the initial learning rate as 0.001, and the learning rate is reduced to 90% after every 50 epochs.

For multi-modal learning, we adopt the SGD optimiser to optimise the network with a weight decay of 0.0005 and a batch size of 20. We implement the following hyperparameters: 1000 training epochs; a mini-batch size of 20. We set the initial learning rate as 0.001, and the learning rate is reduced to 90% after every 50 epochs. Data augmentation is performed by rotating both images and points cloud data with the same angles.

For population graph-based-GNN, we adopt the Adam optimiser (Ruder, 2016) with a weight a batch size of 20. We apply binary cross-entropy loss for patient classification. We implement the following hyperparameters: 200 training epochs; a mini-batch size of 20. We set the initial learning rate as 0.001, and the learning rate is reduced to 90% after every 50 epochs. We used a semi-supervised training approach proposed by (Kipf & Welling, 2016; Parisot et al., 2018) to perform node classification. During training, both the training and

testing data are included in the large graph, but only the labels of training data are available. Once trained, the graph is applied to classify testing data.

To avoid over-fitting, we applied early stopping, drop-out layers, and regularisation during training, which stop training once the model performance stops improving on a hold-out validation dataset for 5 epochs.

5.3.3 Model evaluation

5.3.3.1 Evaluating the performance of the overall framework:

To evaluate the overall performance of our approach for predicting IDH status, we implement four published methods as the benchmark including a ResNet-based sequence network proposed by (Chang et al., 2018), a DenseNet-based network proposed by (Liang et al., 2018), a hybrid model using ResNet with integrated radiomics features proposed by (Choi et al., 2020) and radiomics feature-based approach proposed (Peng et al., 2021). In addition, ResNet34 and DenseNet50 backbones are also applied to perform classification on both tumour-only images and whole-brain images respectively. Finally, we implemented another multi-modal learning framework DCL-NET proposed by (Lin et al., 2022) as the baseline for multi-modal learning. We modified the DCL-NET to suit our task by substituting the three inputs including two views and one points cloud with images, points cloud and Brain networks. In addition, the encoders are substituted accordingly while IDH-mutant and IDH wild-types are regarded as two labels for classification. All baselines are trained with the binary cross-entropy loss.

To evaluate the performance of the population graph compared to other traditional machine learning models. We also implement the MLP and support vector machines (SVM) as the benchmarks to compare the proposed population graph-enhanced GNN.

The performance of models was evaluated using the AUC of the receiver operating characteristic, accuracy (ACC), specificity (SPE) and sensitivity (SEN).

5.3.3.2 Evaluate population graphs:

We conduct experiments in constructing a population graph to choose the best combination of edge and node weights (Table 5.2).

5.3.3.3 Ablation experiments:

We perform ablation experiments to test the importance of different components in the proposed framework. Specifically, we first test the performance of every single encoder of tumour image, tumour points cloud and brain networks, using an MLP and binary cross-entropy loss. Secondly, we test the performance of the pairwise combinations of training two encoders for the classification. Thirdly, we add the contrastive loss L_{contra} to the training of the above two-encoder combinations for multi-task experiments. All of the above experiments test the importance of each modality in the multi-modal input.

Further, we implement a multi-modal framework without contrastive loss and a multi-modal framework without hierarchical attention to evaluate the importance of those two components in multi-modal learning. Finally, we substitute the population-graph-based GNN with an MLP end to test the usefulness of the population graph.

5.3.4 Visualise interpretation

To interpret the results of the proposed multi-modal learning framework, we identify the critical regions contributing to the prediction from tumour images, tumor points cloud and brain networks using different interpretation approaches.

We employed the Grad-CAM (Selvaraju et al., 2016) to visualise the critical regions on the tumour images and visualise the geometric attention of the points cloud. To visualise the concordance between the points cloud and the tumour image, we project the surface points of the Grad-CAM map overlaid on the tumour image to the corresponding points cloud.

To interpret the learning process of the brain network encoder, we employ the GNNExplainer (Ying et al., 2019) to output a probability score that infers the importance of

the edges in the brain network. We retain those edges with probability scores greater than 50%.

5.4 Results

5.4.1 Performance of population graph

The performance of different approaches to constructing a population graph is in Table 5.3. The results show that the population graph achieves the best performance (AUC 0.962) with the concatenated tumour features and brain network features defined as the node and the cosine similarity between brain network features defined as edge. The population graph that uses the similarity between tumour features to define edge ($u^B, r(u^F)$: AUC 0.914, $\langle u^F, u^B \rangle, r(u^F)$: AUC 0.940) generally performs worse than those using the similarity between brain network features to define edge ($u^F, r(u^B)$: AUC 0.939, $\langle u^F, u^B \rangle, r(u^B)$: AUC 0.962). Strikingly, the population graph with concatenated tumour features and brain network features defined as both node and edge performs the worst (AUC 0.888).

Table 5.3 Experiment for selecting the best combination of the population graph

Node weights	Edge weights	AUC	ACC	SEN	SPE
u^F	$r(u^B)$	0.939	0.879	0.894	0.812
u^B	$r(u^F)$	0.914	0.836	0.833	0.843
$\langle u^F, u^B \rangle$	$r(u^B)$	**0.962**	**0.905**	**0.917**	**0.875**
$\langle u^F, u^B \rangle$	$r(u^F)$	0.940	0.862	0.857	**0.875**
$\langle u^F, u^B \rangle$	$r(\langle u^F, u^B \rangle)$	0.888	0.862	0.905	0.750

5.4.2 Performance of the proposed framework

Our results (Table 5.4) show that the best setting of the multi-modal framework (AUC 0.962) outperforms published baselines (Radiomics: AUC 0.743, ResNet-based: AUC 0.858, DenseNet-based: AUC 0.888, ResNet + Radiomics: AUC 0.822, DCL-NET: AUC 0.897) the CNN backbones (DenseNet+Tumor: AUC 0.938, ResNet+Tumor: 0.907, DenseNet+Brain: AUC 0.719, ResNet+brain: 0.711). It is worth mentioning that the CNN-backbone models with whole brain image input had much worse performance than the models with tumour image inputs, which supports the usefulness of our multi-modal learning approach and the proposed attention module in extracting robust features from the whole brain image. The better performance of our approach compared to the published multi-modal framework (DCL-NET) also suggests the usefulness of the hierarchical attention and multi-modal loss designed for the brain networks.

Notably, the performances of 3D-CNN models are higher than the combination of multi-modal contrastive learning with traditional machine learning models (MLP: AUC 0.936, SVM (nonlinear fitcsvm function in MATLAB): AUC 0.932), implying the importance of the population graph for feature integration.

Table 5.4 Comparing with benchmarks

Models	AUC	ACC	SEN	SPE
Published baselines				
Radiomics [41]	0.743	0.724	0.738	0.688
ResNet-based [12]	0.858	0.795	0.798	0.781
DenseNet-based [5]	0.888	0.819	0.833	0.781
ResNet + Radiomics [14]	0.822	0.793	0.810	0.750
DCL-NET [42]	0.897	0.819	0.857	0.719
CNN backbones				
ResNet+Tumor	0.907	0.810	0.809	0.813
ResNet+Brain	0.711	0.647	0.607	0.750
DenseNet+Tumor	0.938	0.853	0.857	0.844
DenseNet+Brain	0.719	0.672	0.655	0.719
Baselines for GNN				
Multi-modal + MLP	0.936	0.862	0.893	0.781
Multi-modal + SVM	0.932	0.871	0.893	0.813
Proposed framework	**0.962**	**0.905**	**0.917**	**0.875**

5.4.3 Ablation experiments

The full results of the ablation experiments are shown in Table 5.5.

For multi-modal input experiments: the experiments of the individual encoder show that the brain encoder (AUC 0.877) outperforms the tumour geometric (AUC 0.858) and tumour image (AUC 0.869) encoders. The multi-task two-encoder experiments indicate that the best combination of data modalities is tumour image and tumour points cloud (AUC 0.874). The two-encoder experiments with the additional contrastive loss show that combining tumour image and tumour geometric encoders (AUC 0.929) consistently performs the best. The contrastive loss significantly improves the two-encoder setup.

For the multi-modal learning stage, removing the graph attention modules significantly decreases the performance of the contrastive training framework (with attention: AUC 0.936, without attention: AUC 0.924). The model without multi-modal contrastive loss also generates a lower performance (with L_{multi} AUC 0.936, without L_{multi} AUC 0.910).

Further, we evaluate the importance of the population graph: replacing population-graph-based GNN with MLP will result in a lower AUC (MLP: AUC 0.935, Population graph-based GNN AUC 0.962). Finally, we tested the model performance with and without a manually corrected tumour mask, and the results showed that our framework slightly relies on the accurate mask. However, the framework with the automatically generated mask still outperforms published models in Table 5.5.

Table 5.5 Ablation experiments

Ablation experiments	AUC	ACC	SEN	SPE
Multi-modal input				
f^I+ MLP	0.877	0.802	0.810	0.781
f^P+ MLP	0.858	0.813	0.809	0.812
f^B+ MLP	0.869	0.810	0.821	0.781
$f^I + f^P$+ MLP	0.874	0.828	0.833	0.812
$f^B + f^P$+ MLP	0.871	0.819	0.833	0.781
$f^I + f^B$+ MLP	0.876	0.836	0.860	0.750
$f^I + f^P$+ MLP+ L_{contr}	0.929	0.853	0.893	0.750
$f^B + f^P$+ MLP+ L_{contr}	0.887	0.836	0.869	0.688
$f^I + f^B$+ MLP+ L_{contr}	0.894	0.845	0.833	0.875
Multi-modal learning				
Multi-modal (no L_{multi}) + MLP	0.910	0.836	0.833	0.844
Multi-modal (no attention) + MLP	0.924	0.853	0.869	0.813
Population graph classification				
Multi-modal (full model) + MLP	0.936	0.862	0.893	0.781
Manual correction of tumor masks				
Proposed framework (auto-mask)	0.919	0.888	0.893	0.875
Fulll framework				
Proposed framework	**0.962**	**0.905**	**0.917**	**0.875**

5.4.4 Interpretative visualisation

The interpretative visualisations in Fig. 5.6 show that the image encoder and the geometric encoder indicate common tumour regions (Fig. 5.6D - F) important for model prediction, which suggests that these regions are specific to IDH mutation. Fig. 5.6D shows that the Grad-CAM focuses on the tumour contrast-enhancing edges with high intensity in both T2 and T2-FLAIR images (Fig. 5.6B, C). Through the visualisation in Fig. 5.7, we find that the brain networks of the IDH wild-type demonstrate a higher density of important disrupted edges compared to the IDH mutant. This finding aligns with our prior knowledge that the IDH wild-type is generally more invasive than the IDH mutant.

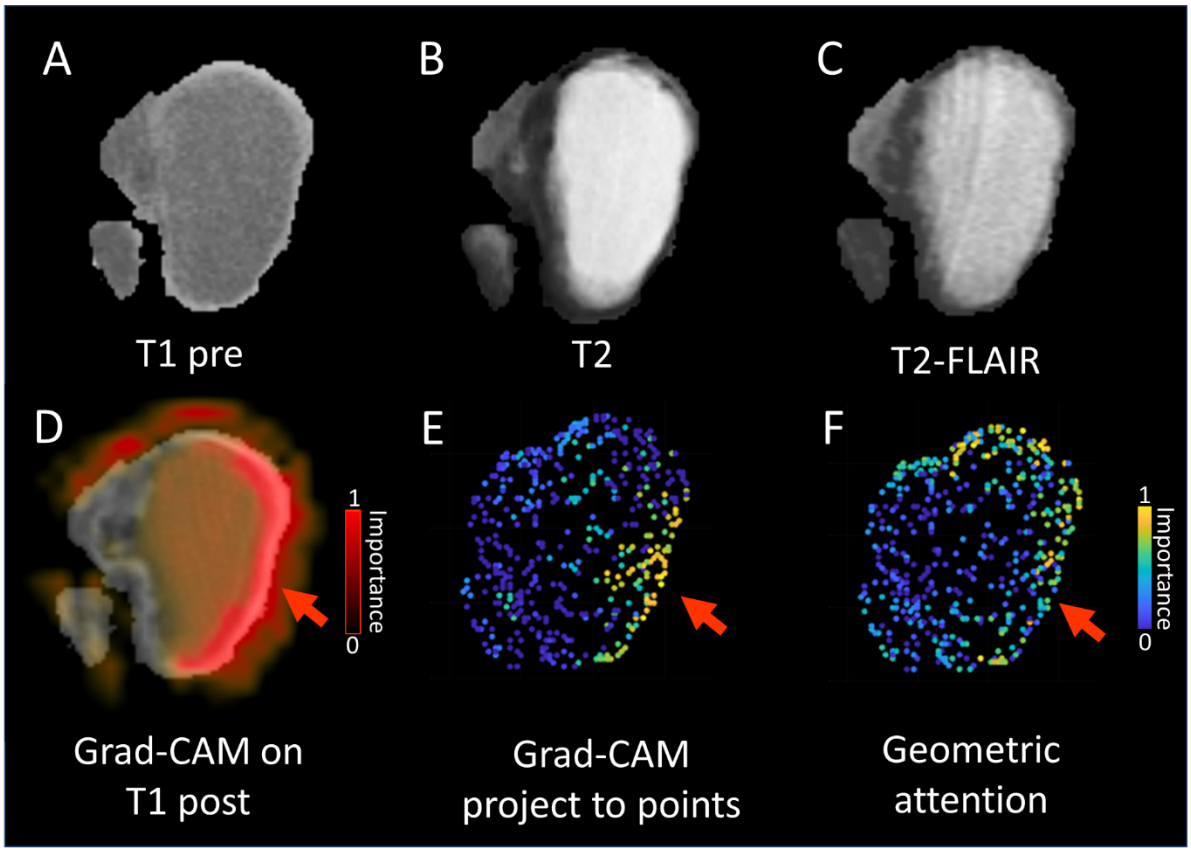


Fig. 5.6 A case example of the interpretation of the image and geometric encoders. A. pre-contrast T1; B. T2; C. T2-FLAIR. D. The Grad-CAM heatmap overlaid on post-contrast T1. E. The Grad-CAM voxels are projected to the points cloud. E. Points attention generated by the geometric encoder.

5.5 Discussion

We propose a multi-modal contrastive learning framework that exploits the multi-modal features extracted from the tumour image, points cloud and global brain networks for predicting glioma genotype. We first develop a novel self-supervised learning approach to construct brain networks from anatomical multi-sequence MRI. Moreover, tumour-related brain network features are extracted by developing hierarchical graph attention for the brain network encoders. Further, we design a bi-level multi-modal contrastive loss that could align tumour-related network features with focal tumour features across the domain gap. Finally,

we construct a population graph that integrates the multi-modal features and predicts patients' genotypes. Our learning framework achieves the highest performance compared to other state-of-the-art methods and benchmark models.

Previous studies show that tumour geometric features demonstrate crucial value in characterising tumours. In our experiments, although a single geometric encoder does not perform the best, combining image and geometric encoders shows high performance, which suggests the benefit of including geometric data to extract relevant features. The interpretative visualisation shown in Fig. 5.6 indicates the agreement between points cloud and image features, which could further validate the effectiveness of multi-modal contrastive learning in aligning multiple data domains. Biologically, this could be interpreted as the association between tumour content and tumour boundaries, indicating tumour aggressiveness and invading patterns.

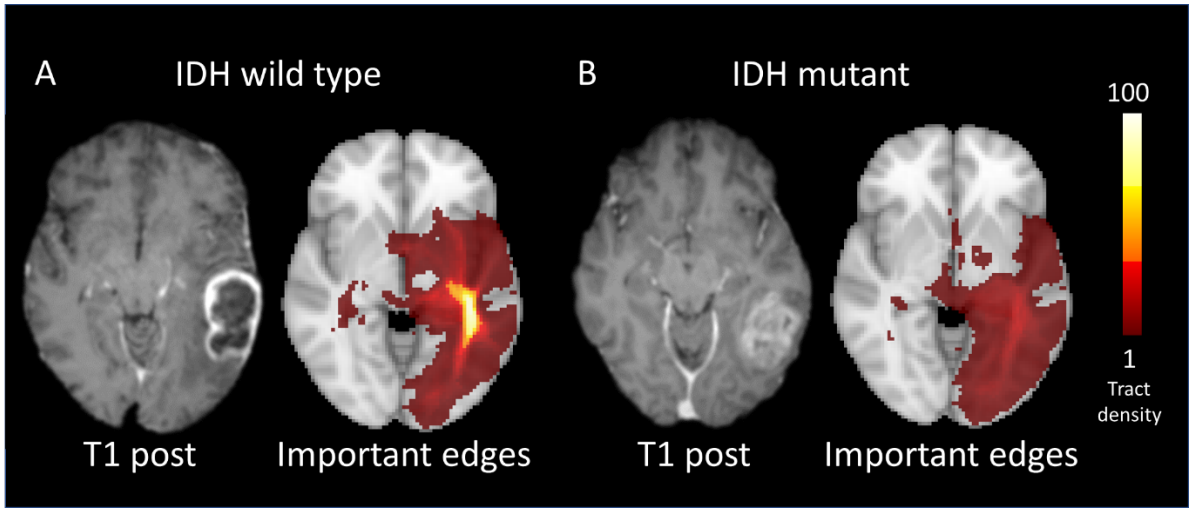


Fig. 5.7. Examples of IDH mutant and wild-type. A. IDH wild-type. B. IDH mutant. Voxel distribution of disrupted tracts with over 50% probability of importance is indicated.

Brain network provides additional value to focal tumour features, as glioma is characterised by diffuse invasion. However, glioma patients frequently demonstrate concomitant pathology beyond the lesion, which challenges extracting tumour-specific features from brain networks. Different from traditional cross-modal attention (Lee et al., 2018), we design a hierarchical attention which helps transfer the geometric attention of

points cloud to crossing edges and minimise the domain gap between focal tumour and brain networks. This neuroscience-inspired attention module demonstrates significance in enhancing the model performance and interpretability, shown by the ablation experiments and visualisation. The hierarchical graph attention demonstrates to indicate tumour invasion across tumour boundaries (Fig. 5.6), which is also associated with the white matter tracts (Fig. 5.7).

Instead of directly applying cross-modal contrastive loss between three modalities in the same latent space, we develop a bi-level contrastive loss, tailored to perform contrastive learning at tumour and brain levels, reflecting the gradient invasion pattern. Our experiments show that our multi-modal contrastive learning outperforms the CNN-based benchmarks, validating the usefulness of properly incorporating tumour geometrics and brain networks in predicting glioma genotype.

The population graph integrates the multi-modal features. The brain network features demonstrate the best features describing patient similarity, and the importance of network features. In contrast, focal tumour features show weaker performance in characterising patient similarity, which might be due to the remarkable tumour heterogeneity and the limited information compared to the global brain, further supporting the value of incorporating comprehensive features in the prediction.

The proposed methods have the potential for automated, rapid diagnosis and prognosis in glioma patients based on pre-treatment MRI, essential for patient risk stratification and treatment planning towards precision medicine. Further, our hierarchical graph attention could help reveal the tumour-related disruption beyond the lesion, which could help enhance more precise planning of surgery and radiotherapy, as Chapter 3 show that identifying disrupted white matter tracts could help reveal invisible tumour invasion on the conventional MRI and indicate recurrence location.

This study has limitations. Firstly, due to the rarity of glioma, our training sample is smaller than other cancers, although our cohort is one of the largest in glioma. Secondly, our cohort is slightly more imbalanced ($\sim 25\%$ IDH mutant) than the reported incidence ($\sim 40\%$) (Liu et al., 2019). We use both AUC and accuracy in evaluating our model performance, which shows comparable results, implying the model's robustness. Thirdly, constructing brain

networks relies on the neuroanatomy atlases, where we use an atlas with 90 brain regions, due to the limitation of computational costs. Adopting the atlases with higher resolution could further increase the framework's performance. Our future work will involve larger datasets and transfer learning to further enhance performance. In addition, a manifold or mesh-based geometric encoder could be utilised to capture features from a more detailed geometric data format.

5.6 Conclusion

We present a novel multi-modal learning framework for predicting the glioma genotype. Our technical contributions include a self-supervised approach for generating brain networks from anatomical MRI; a specialised hierarchical attention module that attends to tumour-related edges and nodes; a bi-level contrastive loss for minimising the domain gap between different modalities; a weighted population graph for feature integration and patient classification. Our framework outperforms CNN-based benchmarks and published state-of-the-art models.

In conclusion, we validated the hypothesis in **Chapter 1.4.2** that multi-modal data might reflect the different views of the same tumour's invasiveness. Multi-modal learning could better characterise tumours to predict the genotypes. In future, we will further develop our model to include clinical variables in the prediction.

Chapter 6. General Discussion

6.1 Summary of main findings

This thesis started with identifying the potentials and methodological limitations of previously published brain tumour studies with network neuroscience approaches in Chapter 1. A robust methodology for constructing structural brain networks using diffusion MRI was then proposed and evaluated in Chapter 2. Based on these methods, the brain network disruption was systematically quantified in Chapter 3, which led to the conclusion that tumour-linked connectomes are prognostically significant. Following this discovery, in Chapter 4, a deep learning model was developed for predicting IDH mutation status to evaluate whether it was feasible to construct structural brain networks with only anatomical prior of white matter tracts and anatomical MRI. Finally, inspired by Chapter 4 and radiomics studies that suggested the significance of tumour geometrics, a multi-modal deep learning framework that learns from tumour images, tumour geometrics, and brain networks was developed for predicting IDH mutation status in Chapter 5.

6.1.1 Review of brain networks and current limitations for brain tumour patients (Chapter 1)

This thesis first reviewed the challenges for the diagnosis and prognosis of the brain tumour, mainly due to the heterogeneity of tumour invasion. Then I reviewed the network neurosciences approach, which has the great potential to characterise the heterogenous brain tumour, which was now considered a systematic disease instead of a focal lesion.

The first finding from the review was that white matter tracts are vulnerable to tumour invasion (Wang et al., 2019; Wang et al., 2022), which suggests the potential of white matter-based structural brain networks to quantify those disruptions for characterising the brain tumour impact. Several studies indicate significant changes in the graph theory properties in brain networks of brain tumour patients (Amoah & Crimi, 2016; Derks et al., 2017; Douw et al., 2019; Huang et al., 2014). This finding established the general hypothesis of this thesis

that white matter-based structural brain networks could better help characterise brain tumours.

Additionally, I identified that current approaches for constructing brain networks are not robust enough since most studies transfer the conventional approach from psychiatric or neurological analysis to brain tumour study, which is prone to severe potential bias caused by brain tumour disruption. In particular, it is challenging to perform the required steps in images of tumour-bearing brains for constructing brain networks, which include tractography (Schult et al., 2019) and non-linear co-registration to the standard brain (Ou et al., 2014). This finding revealed the need for a more robust approach to constructing brain networks in brain tumour patients.

Further, current brain network approaches solely focus on the changes of nodal features that focus on the connectivity of grey matter, which ignores the fact that many brain tumours mainly occur on white matter. Consequently, the nodal feature-based analysis could underestimate the global white matter damage. Although there are other specialised approaches for white matter tract analysis, such as tract-based spatial statistics, they are not as flexible as brain network approaches that can produce both local and global characterisation for individuals (Ćurčić‐Blake et al., 2015). This finding indicates the research gap for characterising brain networks from the aspects of brain network edges.

Finally, I reviewed the machine learning studies of brain networks that are boosted by the current trend of artificial intelligence. Traditional statistical analysis of brain networks only detects the statistical alternation in specific graph theory features or the linear statistical association between graph theory features and clinical variables. In contrast, machine learning models are more capable of detecting complex patterns between multiple variables. However, the machine learning approach relies on the robustness of features from brain networks, which could limit its reproducibility. In contrast, deep learning models are more flexible and not dependent on the robustness of features. Nonetheless, most deep learning models for brain networks are mainly designed for Alzheimer's disease, whereas deep learning models for brain tumours solely focus on images, which leaves a research gap in deep learning for brain networks of brain tumour patients.

6.1.2 A robust approach for constructing brain networks of brain tumour patients (Chapters 2)

In **Chapter 2**, I tested the **first hypothesis** in **Chapter 1.4.2** that a network construction approach that utilises a tractography template combined with white matter skeletons could be more robust than the traditional approach that directly performs tractography in patients. I designed several experiments to compare the proposed method with conventional approaches to constructing brain networks with tractography. Mainly, I evaluated the functional relevance of structural brain networks by measuring the SC-FC coupling for individual patients and the structural-functional correlation for the patient group. Additionally, I compared the pathological relevance of the proposed methods and conventional approaches. Results validated the hypothesis and showed that my methodology provided a more robust approach to constructing brain networks than conventional approaches.

6.1.3 Systematic Analysis for brain network disruptions in brain tumour patients (Chapter 3)

In **Chapter 3**, I described a study that tested the **second hypothesis** in **Chapter 1.4.2**, which hypothesises that the disruptions of brain networks are associated with patients' cognition, performance, and survival time, which could indicate the early invasion of tumour cells. This chapter comprehensively characterises the tumour impact from both nodes and edges in brain networks, filling the research gap that most current studies only quantify the tumour impact from brain network nodes.

Enhanced by the methodology in **Chapter 2**, I constructed brain networks in two independent cohorts of patients and one cohort of age-matching healthy controls. The disruptions of the connectome in patients were defined as the degree of deviation from the distribution of healthy controls. Additionally, the connectome damages in patients were categorised according to the lesion to address the heterogenous disruption in contrast-enhancing, non-enhancing, and normal-appearing brain regions. In general, different analyses found the disruption in the connectome profile of distant regions connecting to tumour

regions to be particularly significant. Mainly, distant disruption was found to be significantly associated with patients' performance and cognitive function. Commonly used topological/graph theory features, including clustering coefficient and characteristic path length, were also significant in the above analysis.

Moreover, distant disruption was the main contributor to the topological changes among all disruptions. Comprehensive analyses were performed to evaluate the prognostic significance of distant disruption and topological features, including log-rank test, univariate/multivariate cox proportional regression and AUC analysis. All results cross-validated the prognostic values of the distant disruption. Furthermore, the preserved connectome profile that excluded disrupted connections was also found significant in survival analysis, suggesting the reorganisation mechanism in patients. Finally, the preliminary analysis suggested that connectome disruption might be associated with tumour recurrence.

This study revealed and quantified the glioblastoma invasion distant from the focal lesion and invisible on the conventional MRI, which had the potential to aid more accurate patient stratification and more precise treatment planning.

6.1.4 A feasible approach for constructing brain networks with anatomical MRI (Chapter 4)

Chapter 4 tested the **third hypothesis** in **Chapter 1.4.2** regarding the feasibility of constructing brain networks from anatomical MRI. Additionally, I tested the hypothesis that models that learn from brain networks could better predict genotypes of gliomas than models that only learn from tumour images. Specifically, I estimated structural brain networks by extracting features from the tractography-template-defined ROIs in anatomical MRI using autoencoders. I then applied graph neural networks to learn from brain networks. The performance of this approach was evaluated by a task that predicts the IDH mutation status in glioma patients. Results showed that our methods outperformed computer vision-based models in this task, which validated the feasibility of constructing structural brain networks without diffusion-weighted MRI.

6.1.5 Multi-modal learning of brain networks, tumour images and geometrics (Chapter 5)

In Chapter 5, I developed a multi-modal deep learning framework trained by multi-modal data from anatomical MRI. Specifically, this model learns from tumour image, tumour geometrics and brain network data simultaneously, based on the **last hypothesis** in **Chapter 1.4.2** that tumour invasion can be reflected in different views of the tumour properties, which should be closely related (e.g. internal: tumour images, boundary: tumour geometric and external: brain networks). The framework was trained to classify the IDH mutation status, which reflects the tumour's aggressiveness. The framework contained three major modules.

The first module is the data generation of tumour images, tumour geometric points cloud, and brain network.

The second module extract features from multi-modal data using a self-supervised multi-modal contrastive learning model. This module had specialised hierarchical attention designed for brain networks to extract the most interrelated edge and node features between brain networks and tumour image/geometrics. Specifically, edge attention was generated from tumour geometrics, which hypothesised that tumour geometrics was associated with invasion on white matter tracts. Additionally, node attention was generated by focusing on nodes closely related to focal tumour features.

The third module is a population graph that treated the complete patient cohort as a large graph where the tumour features of patients were defined as nodes. The population graph was then applied to a graph neural network to perform patient classification with node classification tasks. The results showed that our model outperforms other published models for classifying IDH mutation status in glioma patients.

Finally, the visualisation of model interpretation validated the hypothesis that the model could extract corresponding interrelated features from tumour images, tumour geometrics and brain networks. This study revealed the potential of incorporating neurological prior (brain networks) into deep learning models.

6.2 Methodological Limitations

6.2.1 Brain parcellation atlas

All studies in this thesis utilised a single atlas (AAL atlas) with only 90 nodes for cortical parcellation in the brain. The primary consideration is that a coarse brain network could mitigate the errors introduced in construction steps by the tumour lesion. Specifically, coarse node regions could relatively reduce registration errors compared with finer node regions. However, it was reported that the choice of an atlas could influence the results of graph theory analyses (Andellini et al., 2015; Mårtensson et al., 2018), while novel atlases with higher resolution of nodes are more functionally and clinically relevant (Joliot et al., 2015). In the future, a high-resolution atlas could be applied to brain networks when there is a more advanced development in registration techniques for the tumour-bearing brain MRI.

6.2.2 Tractography template

Another methodological consideration is the usage of the tractography template. All four studies applied a tractography template to construct brain networks instead of the direct application of tractography in brain tumour patients, which was under the assumption that the tumour impact of brain networks was much more significant than the normal variability among subjects. Under the same assumption, the brain networks constructed in this thesis only reflected the integrity of the core of white matter tracts (white matter skeleton) with high specificity. In contrast, the sensitivity for detecting weak damage on the edges of white matter tracts is low (Fagerholm et al., 2015). Although the hypothesis could be held for high-grade glioma patients who usually suffer from substantial disruptions in brain networks, it might create a bias for low-grade glioma patients with small tumour sizes. Hence the methodology in this thesis should be applied with extra caution when solely used for low-grade glioma patients. The method of using tractography templates could be phased out when the tractography technique is advanced enough to generate robust tracking in tumour-affected regions in the future.

6.2.3 Coregistration of images

A common question regarding the pre-processing of tumour study is whether the non-linear co-registration between the tumour-bearing brain and the standard brain is robust, as the mass effect of the tumour usually distorts the brain tissues, which challenges the co-registration algorithm. Although the current co-registration technique is far from perfect, co-registration is necessary for brain network construction.

Specifically, most algorithms (e.g. ANTs and FNIRT) mask out the tumour regions and maximise the accuracy of coregistration outside tumour regions to generate sub-optimum results. Some specialised algorithms, such as Glioma Image Segmentation and Registration (GLISTR), simulate the growth of tumours to model the mass effect of the tumour (Gooya et al., 2012). However, such methods lack generalisation and perform inconsistently. The co-registration errors will lead to incorrect brain networks and questionable results. In this study, I mitigate this problem by manually inspecting every co-registration result to reduce severe mistakes (e.g. testing different coregistration parameters for bad co-registration results). In the future, a better algorithm for co-registration could further enhance the significance and the reliability of the result in Chapter 2&3 and model performance in Chapter 4&5.

6.2.4 MRI harmonisation

Due to the rarity of brain tumours, this thesis utilised data from multiple sources with different MRI scanners and medical centres. In Chapter 3, I followed a radiomics processing pipeline that applies histogram-matching to harmonise MRI data to reduce discrepancies between different sequences and scanners (Bakas et al., 2017). Additionally, in Section 3.4.2, I used a statistical test to evaluate whether the discrepancy between various data sources was minimised to a statistically insignificant range.

Although the results suggested this basic approach is effective for minimising the statistical discrepancies between different MRI sequences, the histogram-matching is under a strong assumption that the intensity distribution of different patients is similar regardless of the heterogeneity of intensity and size in brain tumours. Additionally, the histogram-matching

was initially designed for anatomical MRI (e.g. T1, T2). Hence the validity of it on quantitative maps (e.g., FA) requires further research. In the future, extensive studies could be conducted to design MRI harmonisation techniques that combine large datasets to generate reliable results with more substantial statistical power.

6.3 Future research directions

6.3.1 Longitudinal brain networks

One potential future direction of this thesis is expanding the dataset from cross-sectional to longitudinal data. All experimental chapters in this study only included pre-operative MRI data for constructing brain networks. However, a significant limitation of this approach was that these studies assume the patient's pre-operative status follows a linear trajectory, which underestimated the variation in the effect of surgery and chemoradiotherapy. Although relevant factors were included as confounders in the survival model, the response of brain networks to treatments remained unknown.

Longitudinal analysis has already been widely conducted on Alzheimer's Disease, which has more openly available data thanks to Alzheimer's Disease Neuroimaging Initiative. One of the advantages of longitudinal studies over cross-sectional studies is that longitudinal studies can potentially use state-of-the-art statistical methods to jointly estimate the brain networks over multiple visits by pooling information across visits (Kundu et al., 2019). In contrast, longitudinal brain network studies for brain tumours still have a large research gap. Aerts et al. proposed a pioneer study with pre-operative and post-operative brain network data (Aerts et al., 2020), which showed significant differences between the topological features of brain networks before and after surgery. However, the statistical power was limited due to the smaller sample size.

In the future, a large longitudinal cohort could be studied to better characterise the tumour invasion with longitudinal brain network changes. Particularly, the PRaM-GBM study of my affiliated group, Cambridge Brain Tumour Imaging Laboratory, collects longitudinal

follow-up MRI data from glioblastoma patients and could enhance the development of brain network research towards the future direction of the longitudinal study.

Finally, deep learning models enhanced by longitudinal data for studies of Alzheimer's Disease also showed better performance than models trained by cross-sectional data (Ma et al., 2020; Ortiz et al., 2017), which characterises the heterogenous variation in the progression of the diseases. Under a similar principle, a better survival prediction model could be potentially developed by utilising the longitudinal brain networks of glioblastoma patients.

6.3.2 Multi-modal brain networks

Another crucial future improvement of this thesis is to include functional brain networks and study the interaction between structural and functional brain networks. One limitation of structural brain networks was that they could only detect white matter damage, as diffusion-weighted imaging is mainly sensitive to white matter disruption. In contrast, functional MRIs are usually more sensitive to cortical damage.

Additionally, this thesis was under the assumption that brain tumours destroyed the brain tissues of lesion areas entirely. However, functional MRI study evidence suggested functional connectivity between the tumour and normal-appearing regions (Stoecklein et al., 2020). Functional brain networks are essential for evaluating brain tumour patients' cognition, functionality, and quality of life after the diagnosis and treatments.

Due to the data availability and the impact of Covid-19, I only collected a limited amount of functional MRI data from both in-house cohort and open datasets. The functional data were only applied in Chapter 2 for constructing functional brain networks to evaluate the functional relevance of the structural brain networks of my proposed approach. In the future, multi-model brain networks, including functional and structural brain networks, could be studied in brain tumour patients.

Particularly, the Surgically Induced Neurological Deficits (SIND) study of my affiliated group, Cambridge Brain Tumour Imaging Laboratory, is currently collecting diffusion MRI and functional MRI, which could potentially enhance the development of the study in multi-

modal brain networks. By using the multi-modal brain networks, the functional reserve, white matter invasion and cortical invasion could be better characterised for patient stratification, prognosis, and surgical planning.

6.3.3 Big-data brain networks

Currently, most deep learning models are data-hungry. Hence there are very limited deep-learning studies for brain tumours due to the small amount of open data. There is a boost in deep learning of brain tumours thanks to the publication of the multimodal brain tumour image segmentation benchmark (BRATS) and its corresponding Multimodal Brain Tumor Segmentation Challenge (BRATS) challenges held since 2014 (Menze et al., 2014). Additionally, other studies applied state-of-art models from the computer vision field to perform classification tasks (e.g., predicting IDH, predicting MGMT) using anatomical MRI (T1, T1C, T2, FLAIR). Nonetheless, openly published MRI data was less than 500 before 2022, which is still considered small for most deep-learning models. Moreover, there were even fewer open MRI data (e.g., diffusion MRI, functional MRI) for constructing brain networks in brain tumour patients (Aerts & Marinazzo, 2019; Pernet et al., 2016).

Brain network studies have the opportunity to transform into big-data studies in the future, thanks to the recent trend of open-data publication. For example, the University of Pennsylvania and the University of California San Francisco recently contributed datasets with multimodal MRI, including anatomical and diffusion MRI for 630 (UPenn-GBM) (Bakas et al., 2022) and 500 (UCSF-PDGM) (Calabrese et al., 2021) patients in 2022 respectively, which increase the total open diffusion MRI data of brain tumours to over 1000.

Future studies could utilise the open diffusion MRI data to construct a large cohort of brain networks to generate more reproducible results with more substantial statistical power. Additionally, the availability of those data could further enhance the development of deep learning in brain networks constructed from diffusion MRI to increase the performance of existing brain network models. Specifically, my future plan is to use the robust methodology developed in Chapter 2 to construct a large open brain networks benchmark dataset with existing open data on brain tumours. In this way, more experts from the fields of deep

learning could be attracted by the convenient data to design specialised neural networks for brain networks in brain tumour patients, which hopefully could boost the development of this field, similar to the trends of brain tumour segmentation since 2014.

6.3.4 Interpretable deep learning models for brain networks

Deep learning models developed in Chapter 4&5 were mainly evaluated in terms of prediction performance. Although accurate prediction is essential, it is also clinically important to explain how the model generates that prediction, which is also referred to as model interpretation. Visual interpretation in Chapter 4&5 preliminarily generated qualitative reference suggesting the clinical relevance of the model prediction, which are facilitated by the model interpretation algorithms such as GNNExplaner and Grad-CAM. However, those methods are mainly applied for trained models and do not help improve the model performance or generate quantitive explanations.

An interpretable model instead of a black box could potentially be more acceptable for clinical applications. Hence, the future direction of deep learning models on brain networks of brain tumours could focus more on designing quantitative interpretation modules to generate more interpretable predictions. Additional statistical analysis could also be conducted to validate the robustness and reliability of the quantitative interpretation.

6.3.5 Integrating natural language models

Future work could also explore the application of various deep learning architectures, including large language models (LLMs) like GPT-4, to integrate language-based data modalities (e.g. medical reports) into brain tumour characterisation. LLMs have demonstrated remarkable capabilities in understanding and generating human-like text, and their application in the medical field could help extract valuable information from unstructured data sources such as clinical notes, research articles, and patient records. Incorporating these language-based data modalities into brain tumour characterisation models could enhance our

understanding of tumour behaviour and ultimately contribute to more accurate and personalised treatment strategies. It is worth mentioning that the involvement of large language models such as GPT-4 also invokes the issue of AI ethics and safety. For example, most approved clinical trials or grant with sensitive patient data will not allow the application of GPT-4 which requires the user to send the data to the servers of OpenAI. Additionally, the common problems of hallucination might cause the model to generate high-confident incorrect results which is fatal for a diagnostic system. The LLM could be efficiently applied until those problems are solved.

Additionally, large pretraining methods, such as Contrastive Language-Image Pretraining (CLIP), can also be applied to further improve the performance of the MRI encoders. CLIP is an innovative approach that jointly learns from images and their associated textual descriptions, allowing for better generalisation and transfer learning capabilities. By leveraging the power of CLIP and similar methods, MRI encoders could be enhanced to capture more detailed and nuanced features from medical images, leading to better characterisation of brain tumours and their invasiveness.

In summary, the application of advanced deep learning architectures, such as large language models and pretraining methods could significantly enhance our understanding of brain tumours and contribute to the development of more effective and personalised treatment strategies for patients.

6.3.6 Clinical Translation and Personalised Medicine

Clinical translation of the methodologies and insights gained from this thesis should also be focused in the future. This would involve further validation using larger, independent patient cohorts and close collaboration with clinicians and medical professionals to ensure seamless integration into diagnostic tools, treatment planning, and patient care.

The development of more accurate and personalized treatment strategies, including the use of large language models for generating patient-specific recommendations, could lead to better outcomes for patients and overall improvements in quality of life. By leveraging AI

models and data-driven insights, healthcare providers can tailor treatments to individual patient's needs, taking into account their unique characteristics, such as genetic information, brain network disruptions, and clinical variables.

Furthermore, it is essential to evaluate the cost-effectiveness of implementing AI models in clinical practice. Future studies should assess the economic impact of integrating these models into the clinical workflow, ensuring that the benefits they provide outweigh the costs and resources required for their implementation. By demonstrating the value of AI-driven personalized medicine, this research could help secure the necessary support and resources to advance its adoption in healthcare systems.

In conclusion, future directions should seek to bridge the gap between cutting-edge research and real-world application. By validating and integrating AI models and methodologies into clinical practice, this research could significantly improve patient outcomes, advance treatment strategies, and promote a more personalized approach to brain tumour management.

References

Aerts, H., Fias, W., Caeyenberghs, K., & Marinazzo, D. (2016). Brain networks under attack: robustness properties and the impact of lesions. *Brain*, *139*(12), 3063-3083.

Aerts, H., Schirner, M., Dhollander, T., Jeurissen, B., Achten, E., Van Roost, D., Ritter, P., & Marinazzo, D. (2020). Modeling brain dynamics after tumor resection using The Virtual Brain. *Neuroimage*, *213*, 116738.

Ahmad, A., Sarkar, S., Shah, A., Gore, S., Santosh, V., Saini, J., & Ingalhalikar, M. (2019). Predictive and discriminative localization of IDH genotype in high grade gliomas using deep convolutional neural nets. 2019 IEEE 16th International Symposium on Biomedical Imaging (ISBI 2019),

Alghamdi, A. J. (2023). The Value of Various Post-Processing Modalities of Diffusion Weighted Imaging in the Detection of Multiple Sclerosis. *Brain Sciences*, *13*(4), 622.

Allan, P. G., Briggs, R. G., Conner, A. K., O'Neal, C. M., Bonney, P. A., Maxwell, B. D., Baker, C. M., Burks, J. D., Sali, G., & Glenn, C. A. (2019). Parcellation-based tractographic modeling of the dorsal attention network. *Brain and behavior*, *9*(10), e01365.

Amoah, B., & Crimi, A. (2016). Topological Measures of Connectomics for Low Grades Glioma. International Workshop on Brainlesion: Glioma, Multiple Sclerosis, Stroke and Traumatic Brain Injuries,

Andellini, M., Cannatà, V., Gazzellini, S., Bernardi, B., & Napolitano, A. (2015). Test-retest reliability of graph metrics of resting state MRI functional brain networks: A review. *Journal of neuroscience methods*, *253*, 183-192.

Andersson, J. L., Jenkinson, M., & Smith, S. (2007). Non-linear registration aka Spatial normalisation FMRIB Technial Report TR07JA2. *FMRIB Analysis Group of the University of Oxford*, 1-22.

Aquino, D., Gioppo, A., Finocchiaro, G., Bruzzone, M. G., & Cuccarini, V. (2017). MRI in glioma immunotherapy: evidence, pitfalls, and perspectives. *Journal of immunology research*, *2017*.

Avants, B. B., Tustison, N., & Song, G. (2009). Advanced normalization tools (ANTS). *Insight j*, *2*(365), 1-35.

Bach, M., Laun, F. B., Leemans, A., Tax, C. M., Biessels, G. J., Stieltjes, B., & Maier-Hein, K. H. (2014). Methodological considerations on tract-based spatial statistics (TBSS). *Neuroimage*, *100*, 358-369.

Bakas, S., Akbari, H., Sotiras, A., Bilello, M., Rozycki, M., Kirby, J. S., Freymann, J. B., Farahani, K., & Davatzikos, C. (2017). Advancing The Cancer Genome Atlas glioma MRI collections with expert segmentation labels and radiomic features. *Scientific Data*, *4*(1), 170117. https://doi.org/10.1038/sdata.2017.117

Bakas, S., Sako, C., Akbari, H., Bilello, M., Sotiras, A., Shukla, G., Rudie, J. D., Santamaría, N. F., Kazerooni, A. F., & Pati, S. (2022). The University of Pennsylvania glioblastoma (UPenn-GBM) cohort: Advanced MRI, clinical, genomics, & radiomics. *Scientific data*, *9*(1), 1-12.

Bassett, D. S., & Bullmore, E. T. (2009). Human brain networks in health and disease. *Current opinion in neurology*, *22*(4), 340.

Bassett, D. S., & Sporns, O. (2017). Network neuroscience. *Nature neuroscience*, *20*(3), 353-364.

Behrens, T. E., Berg, H. J., Jbabdi, S., Rushworth, M. F., & Woolrich, M. W. (2007). Probabilistic diffusion tractography with multiple fibre orientations: What can we gain? *neuroimage*, *34*(1), 144-155.

Behrens, T. E., Woolrich, M. W., Jenkinson, M., Johansen-Berg, H., Nunes, R. G., Clare, S., Matthews, P. M., Brady, J. M., & Smith, S. M. (2003). Characterization and propagation of uncertainty in diffusion-

weighted MR imaging. *Magnetic Resonance in Medicine: An Official Journal of the International Society for Magnetic Resonance in Medicine*, *50*(5), 1077-1088.

Boots-Sprenger, S. H., Sijben, A., Rijntjes, J., Tops, B. B., Idema, A. J., Rivera, A. L., Bleeker, F. E., Gijtenbeek, A. M., Diefes, K., & Heathcock, L. (2013). Significance of complete 1p/19q co-deletion, IDH1 mutation and MGMT promoter methylation in gliomas: use with caution. *Modern Pathology*, *26*(7), 922-929.

Bronstein, M. M., Bruna, J., LeCun, Y., Szlam, A., & Vandergheynst, P. (2017). Geometric deep learning: going beyond euclidean data. *IEEE Signal Processing Magazine*, *34*(4), 18-42.

Bullmore, E., & Sporns, O. (2009). Complex brain networks: graph theoretical analysis of structural and functional systems. *Nature reviews neuroscience*, *10*(3), 186-198.

Cabanes, C., Grouazel, A., von Schuckmann, K., Hamon, M., Turpin, V., Coatanoan, C., Paris, F., Guinehut, S., Boone, C., & Ferry, N. (2013). The CORA dataset: validation and diagnostics of in-situ ocean temperature and salinity measurements. *Ocean Science*, *9*(1), 1-18.

Calabrese, E., Villanueva-Meyer, J., Rudie, J., Rauschecker, A., Baid, U., Bakas, S., Mongan, J., Hess, C., & Cha, S. (2021). The University of California San Francisco Preoperative Diffuse Glioma (UCSF-PDGM) MRI Dataset. *arXiv preprint arXiv:2109.00356*.

Çallı, E., Sogancioglu, E., van Ginneken, B., van Leeuwen, K. G., & Murphy, K. (2021). Deep learning for chest X-ray analysis: A survey. *Medical Image Analysis*, *72*, 102125.

Castillo, M. (2006). *Neuroradiology companion: methods, guidelines, and imaging fundamentals*. Lippincott Williams & Wilkins.

Chaddad, A., Kucharczyk, M. J., Daniel, P., Sabri, S., Jean-Claude, B. J., Niazi, T., & Abdulkarim, B. (2019). Radiomics in glioblastoma: current status and challenges facing clinical implementation. *Frontiers in oncology*, *9*, 374.

Chaichana, K., Parker, S., Olivi, A., & Quiñones-Hinojosa, A. (2010). A proposed classification system that projects outcomes based on preoperative variables for adult patients with glioblastoma multiforme. *Journal of neurosurgery*, *112*(5), 997-1004.

Chang, K., Bai, H. X., Zhou, H., Su, C., Bi, W. L., Agbodza, E., Kavouridis, V. K., Senders, J. T., Boaro, A., & Beers, A. (2018). Residual Convolutional Neural Network for the Determination of IDH Status in Low-and High-Grade Gliomas from MR ImagingNeural Network for Determination of IDH Status in Gliomas. *Clinical Cancer Research*, *24*(5), 1073-1081.

Chen, Z., Tie, Y., Olubiyi, O., Rigolo, L., Mehrtash, A., Norton, I., Pasternak, O., Rathi, Y., Golby, A. J., & O'Donnell, L. J. (2015). Reconstruction of the arcuate fasciculus for surgical planning in the setting of peritumoral edema using two-tensor unscented Kalman filter tractography. *NeuroImage: Clinical*, *7*, 815-822.

Choi, Y. S., Bae, S., Chang, J. H., Kang, S.-G., Kim, S. H., Kim, J., Rim, T. H., Choi, S. H., Jain, R., & Lee, S.-K. (2020). Fully automated hybrid approach to predict the IDH mutation status of gliomas via deep learning and radiomics. *Neuro-Oncology*, *23*(2), 304-313. https://doi.org/10.1093/neuonc/noaa177

Clark, K., Vendt, B., Smith, K., Freymann, J., Kirby, J., Koppel, P., Moore, S., Phillips, S., Maffitt, D., & Pringle, M. (2013). The Cancer Imaging Archive (TCIA): maintaining and operating a public information repository. *Journal of digital imaging*, *26*(6), 1045-1057.

Crossley, N. A., Mechelli, A., Scott, J., Carletti, F., Fox, P. T., McGuire, P., & Bullmore, E. T. (2014). The hubs of the human connectome are generally implicated in the anatomy of brain disorders. *Brain*, *137*(8), 2382-2395. https://doi.org/10.1093/brain/awu132

Cuddapah, V. A., Robel, S., Watkins, S., & Sontheimer, H. (2014). A neurocentric perspective on glioma invasion. *Nat Rev Neurosci*, *15*(7), 455-465. https://doi.org/10.1038/nrn3765

Ćurčić-Blake, B., van der Meer, L., Pijnenborg, G. H., David, A. S., & Aleman, A. (2015). Insight and psychosis: Functional and anatomical brain connectivity and self-reflection in S chizophrenia. *Human brain mapping*, *36*(12), 4859-4868.

Dang, L., White, D. W., Gross, S., Bennett, B. D., Bittinger, M. A., Driggers, E. M., Fantin, V. R., Jang, H. G., Jin, S., & Keenan, M. C. (2009). Cancer-associated IDH1 mutations produce 2-hydroxyglutarate. *Nature*, *462*(7274), 739-744.

Daniel, A. G., Park, K. Y., Roland, J. L., Dierker, D., Gross, J., Humphries, J. B., Hacker, C. D., Snyder, A. Z., Shimony, J. S., & Leuthardt, E. C. (2020). Functional connectivity within glioblastoma impacts overall survival. *Neuro-Oncology*.

Derks, J., Dirkson, A. R., de Witt Hamer, P. C., van Geest, Q., Hulst, H. E., Barkhof, F., Pouwels, P. J., Geurts, J. J., Reijneveld, J. C., & Douw, L. (2017). Connectomic profile and clinical phenotype in newly diagnosed glioma patients. *NeuroImage: Clinical*, *14*, 87-96.

Douw, L., Miller, J. J., Steenwijk, M. D., Stufflebeam, S. M., & Gerstner, E. R. (2019). Altered structural hub connectivity and its clinical relevance in glioma. *bioRxiv*, 610618.

Essig, M. (2005). Gadobenate dimeglumine (MultiHance®) in MR imaging of the CNS: studies to assess the benefits of a high relaxivity contrast agent. *Academic Radiology*, *12*(5), S23-S27.

Fagerholm, E. D., Hellyer, P. J., Scott, G., Leech, R., & Sharp, D. J. (2015). Disconnection of network hubs and cognitive impairment after traumatic brain injury. *Brain*, *138*(6), 1696-1709. https://doi.org/10.1093/brain/awv075

Fey, M., & Lenssen, J. E. (2019). Fast graph representation learning with PyTorch Geometric. *arXiv preprint arXiv:1903.02428*.

Fleisher, A. S., Sherzai, A., Taylor, C., Langbaum, J. B., Chen, K., & Buxton, R. B. (2009). Resting-state BOLD networks versus task-associated functional MRI for distinguishing Alzheimer's disease risk groups. *Neuroimage*, *47*(4), 1678-1690.

Gilmer, J., Schoenholz, S. S., Riley, P. F., Vinyals, O., & Dahl, G. E. (2017). Neural message passing for quantum chemistry. International conference on machine learning,

Gooya, A., Pohl, K. M., Bilello, M., Cirillo, L., Biros, G., Melhem, E. R., & Davatzikos, C. (2012). GLISTR: glioma image segmentation and registration. *IEEE transactions on medical imaging*, *31*(10), 1941-1954.

Gorlia, T., van den Bent, M. J., Hegi, M. E., Mirimanoff, R. O., Weller, M., Cairncross, J. G., Eisenhauer, E., Belanger, K., Brandes, A. A., & Allgeier, A. (2008). Nomograms for predicting survival of patients with newly diagnosed glioblastoma: prognostic factor analysis of EORTC and NCIC trial 26981-22981/CE. 3. *The lancet oncology*, *9*(1), 29-38.

Grabner, G., Janke, A. L., Budge, M. M., Smith, D., Pruessner, J., & Collins, D. L. (2006). Symmetric atlasing and model based segmentation: an application to the hippocampus in older adults. International Conference on Medical Image Computing and Computer-Assisted Intervention,

Greicius, M. D., Krasnow, B., Reiss, A. L., & Menon, V. (2003). Functional connectivity in the resting brain: a network analysis of the default mode hypothesis. *Proceedings of the National Academy of Sciences*, *100*(1), 253-258.

Gu, X., Knutsson, H., Nilsson, M., & Eklund, A. (2019). Generating diffusion MRI scalar maps from T1 weighted images using generative adversarial networks. Scandinavian Conference on Image Analysis,

Hagmann, P., Jonasson, L., Maeder, P., Thiran, J.-P., Wedeen, V. J., & Meuli, R. (2006). Understanding diffusion MR imaging techniques: from scalar diffusion-weighted imaging to diffusion tensor imaging and beyond. *Radiographics*, *26*(suppl_1), S205-S223.

Han, Y., Xie, Z., Zang, Y., Zhang, S., Gu, D., Zhou, M., Gevaert, O., Wei, J., Li, C., & Chen, H. (2018). Non-invasive genotype prediction of chromosome 1p/19q co-deletion by development and validation of an MRI-based radiomics signature in lower-grade gliomas. *Journal of neuro-oncology*, *140*(2), 297-306.

Hashemi, R. H., Bradley, W. G., & Lisanti, C. J. (2012). *MRI: the basics: The Basics*. Lippincott Williams & Wilkins.

Hein, P. A., Eskey, C. J., Dunn, J. F., & Hug, E. B. (2004). Diffusion-weighted imaging in the follow-up of treated high-grade gliomas: tumor recurrence versus radiation injury. *American Journal of Neuroradiology*, *25*(2), 201-209.

Huang, L. E. (2019). Friend or foe—IDH1 mutations in glioma 10 years on. *Carcinogenesis*, *40*(11), 1299-1307.

Huang, L. E. (2022). Impact of CDKN2A/B Homozygous Deletion on the Prognosis and Biology of IDH-Mutant Glioma. *Biomedicines*, *10*(2), 246.

Huang, Q., Zhang, R., Hu, X., Ding, S., Qian, J., Lei, T., Cao, X., Tao, L., Qian, Z., & Liu, H. (2014). Disturbed small-world networks and neurocognitive function in frontal lobe low-grade glioma patients. *PLoS One*, *9*(4), e94095.

Hyare, H., Rice, L., Thust, S., Nachev, P., Jha, A., Milic, M., Brandner, S., & Rees, J. (2019). Modelling MR and clinical features in grade II/III astrocytomas to predict IDH mutation status. *European Journal of Radiology*, *114*, 120-127. https://doi.org/10.1016/j.ejrad.2019.03.003

Incekara, F., Satoer, D., Visch-Brink, E., Vincent, A., & Smits, M. (2018). Changes in language white matter tract microarchitecture associated with cognitive deficits in patients with presumed low-grade glioma. *Journal of neurosurgery*, *130*(5), 1538-1546.

Isensee, F., Jaeger, P. F., Kohl, S. A., Petersen, J., & Maier-Hein, K. H. (2021). nnU-Net: a self-configuring method for deep learning-based biomedical image segmentation. *Nature methods*, *18*(2), 203-211.

Jenkinson, M., Bannister, P., Brady, M., & Smith, S. (2002). Improved optimization for the robust and accurate linear registration and motion correction of brain images. *Neuroimage*, *17*(2), 825-841.

Joliot, M., Jobard, G., Naveau, M., Delcroix, N., Petit, L., Zago, L., Crivello, F., Mellet, E., Mazoyer, B., & Tzourio-Mazoyer, N. (2015). AICHA: An atlas of intrinsic connectivity of homotopic areas. *Journal of neuroscience methods*, *254*, 46-59.

Kamnitsas, K., Ferrante, E., Parisot, S., Ledig, C., Nori, A. V., Criminisi, A., Rueckert, D., & Glocker, B. (2016). DeepMedic for brain tumor segmentation. International workshop on Brainlesion: Glioma, multiple sclerosis, stroke and traumatic brain injuries,

Kawahara, J., Brown, C. J., Miller, S. P., Booth, B. G., Chau, V., Grunau, R. E., Zwicker, J. G., & Hamarneh, G. (2017). BrainNetCNN: Convolutional neural networks for brain networks; towards predicting neurodevelopment. *NeuroImage*, *146*, 1038-1049.

Khan, I., Waqas, M., & Shamim, M. S. (2017). Prognostic significance of IDH 1 mutation in patients with glioblastoma multiforme. *JPMA. The Journal of the Pakistan Medical Association*, *67*(5), 816.

Kim, D., Wang, N., Ravikumar, V., Raghuram, D., Li, J., Patel, A., Wendt III, R. E., Rao, G., & Rao, A. (2019). Prediction of 1p/19q codeletion in diffuse glioma patients using pre-operative multiparametric magnetic resonance imaging. *Frontiers in computational neuroscience*, *13*, 52.

Kinno, R., Ohta, S., Muragaki, Y., Maruyama, T., & Sakai, K. L. (2014). Differential reorganization of three syntax-related networks induced by a left frontal glioma. *Brain*, *137*(4), 1193-1212.

Kipf, T. N., & Welling, M. (2016). Semi-supervised classification with graph convolutional networks. *arXiv preprint arXiv:1609.02907*.

Kocher, M., Jockwitz, C., Caspers, S., Schreiber, J., Farrher, E., Stoffels, G., Filss, C., Lohmann, P., Tscherpel, C., & Ruge, M. I. (2020). Role of the default mode resting-state network for cognitive functioning in malignant glioma patients following multimodal treatment. *NeuroImage: Clinical*, *27*, 102287.

Kohanbash, G., Carrera, D. A., Shrivastav, S., Ahn, B. J., Jahan, N., Mazor, T., Chheda, Z. S., Downey, K. M., Watchmaker, P. B., & Beppler, C. (2017). Isocitrate dehydrogenase mutations suppress STAT1 and CD8+ T cell accumulation in gliomas. *The Journal of clinical investigation*, *127*(4), 1425-1437.

Kundu, S., Lukemire, J., Wang, Y., & Guo, Y. (2019). A novel joint brain network analysis using longitudinal Alzheimer's disease data. *Scientific reports*, *9*(1), 1-18.

Lapointe, S., Perry, A., & Butowski, N. A. (2018). Primary brain tumours in adults. *The Lancet*, *392*(10145), 432-446.

Latora, V., & Marchiori, M. (2001). Efficient behavior of small-world networks. *Physical review letters*, *87*(19), 198701.

Lauterbur, P. C. (1973). Image formation by induced local interactions: examples employing nuclear magnetic resonance. *nature*, *242*(5394), 190-191.

Lawn, N. D., Westmoreland, B. F., Kiely, M. J., Lennon, V. A., & Vernino, S. (2003). Clinical, magnetic resonance imaging, and electroencephalographic findings in paraneoplastic limbic encephalitis. Mayo Clinic Proceedings,

Lee, K.-H., Chen, X., Hua, G., Hu, H., & He, X. (2018). Stacked cross attention for image-text matching. Proceedings of the European conference on computer vision (ECCV),

Li, C., Wang, S., Yan, J.-L., Piper, R. J., Liu, H., Torheim, T., Kim, H., Zou, J., Boonzaier, N. R., Sinha, R., Matys, T., Markowetz, F., & Price, S. J. (2019). Intratumoral Heterogeneity of Glioblastoma Infiltration Revealed by Joint Histogram Analysis of Diffusion Tensor Imaging. *Neurosurgery*, *85*(4). https://journals.lww.com/neurosurgery/Fulltext/2019/10000/Intratumoral_Heterogeneity_of_Glioblastoma.11.aspx

Li, C., Wang, S., Yan, J.-L., Torheim, T., Boonzaier, N. R., Sinha, R., Matys, T., Markowetz, F., & Price, S. J. (2019). Characterizing tumor invasiveness of glioblastoma using multiparametric magnetic resonance imaging. *Journal of neurosurgery*, *132*(5), 1465-1472.

Li, X., Zhou, Y., Dvornek, N., Zhang, M., Gao, S., Zhuang, J., Scheinost, D., Staib, L. H., Ventola, P., & Duncan, J. S. (2021). Braingnn: Interpretable brain graph neural network for fmri analysis. *Medical Image Analysis*, *74*, 102233.

Liang, S., Zhang, R., Liang, D., Song, T., Ai, T., Xia, C., Xia, L., & Wang, Y. (2018). Multimodal 3D DenseNet for IDH Genotype Prediction in Gliomas. *Genes*, *9*(8), 382. https://www.mdpi.com/2073-4425/9/8/382

Liao, R., Ning, L., Chen, Z., Rigolo, L., Gong, S., Pasternak, O., Golby, A. J., Rathi, Y., & O'Donnell, L. J. (2017). Performance of unscented Kalman filter tractography in edema: Analysis of the two-tensor model. *NeuroImage: Clinical*, *15*, 819-831.

Lin, G., Zheng, Z., Chen, L., Qin, T., & Song, J. (2022). Multi-Modal 3D Shape Clustering with Dual Contrastive Learning. *Applied Sciences*, *12*(15), 7384.

Ling, T., Zhiyu, Q., Yamin, Y., Hongyi, L., & Li, X. (2017). The characteristics of brain structural network in patients with low grade glioma revealed by diffusion tensor imaging. *Journal of Biomedical*

Photonics & Engineering, *3*(3), 30301.

Liu, L., Zhang, H., Rekik, I., Chen, X., Wang, Q., & Shen, D. (2016). Outcome prediction for patient with high-grade gliomas from brain functional and structural networks. International Conference on Medical Image Computing and Computer-Assisted Intervention,

Liu, Y., Yang, K., Hu, X., Xiao, C., Rao, J., Li, Z., Liu, D., Zou, Y., Chen, J., & Liu, H. (2020). Altered rich-club organization and regional topology are associated with cognitive decline in patients with frontal and temporal gliomas. *Frontiers in human neuroscience*, *14*, 23.

Lo, C.-Y., Wang, P.-N., Chou, K.-H., Wang, J., He, Y., & Lin, C.-P. (2010). Diffusion tensor tractography reveals abnormal topological organization in structural cortical networks in Alzheimer's disease. *Journal of Neuroscience*, *30*(50), 16876-16885.

Louis, D. N., Ohgaki, H., Wiestler, O. D., Cavenee, W. K., Burger, P. C., Jouvet, A., Scheithauer, B. W., & Kleihues, P. (2007). The 2007 WHO classification of tumours of the central nervous system. *Acta neuropathologica*, *114*(2), 97-109.

Louis, D. N., Perry, A., Reifenberger, G., Von Deimling, A., Figarella-Branger, D., Cavenee, W. K., Ohgaki, H., Wiestler, O. D., Kleihues, P., & Ellison, D. W. (2016). The 2016 World Health Organization classification of tumors of the central nervous system: a summary. *Acta neuropathologica*, *131*(6), 803-820.

Louis, D. N., Perry, A., Wesseling, P., Brat, D. J., Cree, I. A., Figarella-Branger, D., Hawkins, C., Ng, H., Pfister, S. M., & Reifenberger, G. (2021). The 2021 WHO classification of tumors of the central nervous system: a summary. *Neuro-oncology*, *23*(8), 1231-1251.

Ma, J., Zhu, X., Yang, D., Chen, J., & Wu, G. (2020). Attention-guided deep graph neural network for longitudinal alzheimer's disease analysis. International Conference on Medical Image Computing and Computer-Assisted Intervention,

Mandal, A. S., Romero-Garcia, R., Hart, M. G., & Suckling, J. (2020). Genetic, cellular, and connectomic characterization of the brain regions commonly plagued by glioma. *Brain*, *143*(11), 3294-3307.

Mansfield, P., & Maudsley, A. A. (1977). Medical imaging by NMR. *The British journal of radiology*, *50*(591), 188-194.

Mårtensson, G., Pereira, J. B., Mecocci, P., Vellas, B., Tsolaki, M., Kłoszewska, I., Soininen, H., Lovestone, S., Simmons, A., & Volpe, G. (2018). Stability of graph theoretical measures in structural brain networks in Alzheimer's disease. *Scientific reports*, *8*(1), 1-15.

Menze, B. H., Jakab, A., Bauer, S., Kalpathy-Cramer, J., Farahani, K., Kirby, J., Burren, Y., Porz, N., Slotboom, J., & Wiest, R. (2014). The multimodal brain tumor image segmentation benchmark (BRATS). *IEEE transactions on medical imaging*, *34*(10), 1993-2024.

Miller, A. D., Miller, C. R., & Rossmeisl, J. H. (2019). Canine primary intracranial cancer: a clinicopathologic and comparative review of glioma, meningioma, and choroid plexus tumors. *Frontiers in oncology*, *9*, 1151.

Monje, M., Borniger, J. C., D'Silva, N. J., Deneen, B., Dirks, P. B., Fattahi, F., Frenette, P. S., Garzia, L., Gutmann, D. H., Hanahan, D., Hervey-Jumper, S. L., Hondermarck, H., Hurov, J. B., Kepecs, A., Knox, S. M., Lloyd, A. C., Magnon, C., Saloman, J. L., Segal, R. A., . . . Winkler, F. (2020). Roadmap for the Emerging Field of Cancer Neuroscience. *Cell*, *181*(2), 219-222. https://doi.org/10.1016/j.cell.2020.03.034

Mori, S., & Van Zijl, P. C. (2002). Fiber tracking: principles and strategies–a technical review. *NMR in Biomedicine: An International Journal Devoted to the Development and Application of Magnetic Resonance In Vivo*, *15*(7-8), 468-480.

Mori, S., & Zhang, J. (2006). Principles of diffusion tensor imaging and its applications to basic neuroscience research. *Neuron*, *51*(5), 527-539.

Muller, J., Alizadeh, M., Mohamed, F. B., Riley, J., Pearce, J. J., Trieu, B., Liang, T.-W., Romo, V., Sharan, A., & Wu, C. (2018). Clinically applicable delineation of the pallidal sensorimotor region in patients with advanced Parkinson's disease: study of probabilistic and deterministic tractography. *Journal of Neurosurgery*, *131*(5), 1520-1531.

Na, S., Li, L., Crosson, B., Dotson, V., MacDonald, T. J., Mao, H., & King, T. Z. (2018). White matter network topology relates to cognitive flexibility and cumulative neurological risk in adult survivors of pediatric brain tumors. *NeuroImage: Clinical*, *20*, 485-497.

Norton, I., Essayed, W. I., Zhang, F., Pujol, S., Yarmarkovich, A., Golby, A. J., Kindlmann, G., Wassermann, D., Estepar, R. S. J., & Rathi, Y. (2017). SlicerDMRI: open source diffusion MRI software for brain cancer research. *Cancer research*, *77*(21), e101-e103.

Nyúl, L. G., Udupa, J. K., & Zhang, X. (2000). New variants of a method of MRI scale standardization. *IEEE transactions on medical imaging*, *19*(2), 143-150.

Okuda, T., Korogi, Y., Shigematsu, Y., Sugahara, T., Hirai, T., Ikushima, I., Liang, L., & Takahashi, M. (1999). Brain lesions: when should fluid-attenuated inversion-recovery sequences be used in MR evaluation? *Radiology*, *212*(3), 793-798.

Ortiz, A., Munilla, J., Martínez-Murcia, F. J., Górriz, J. M., Ramírez, J., & Initiative, A. s. D. N. (2017). Learning longitudinal MRI patterns by SICE and deep learning: Assessing the Alzheimer's disease progression. Annual conference on medical image understanding and analysis,

Osborn, A. G., Salzman, K. L., Jhaveri, M. D., & Barkovich, A. J. (2015). *Diagnostic imaging: brain*. Elsevier Health Sciences.

Ou, Y., Akbari, H., Bilello, M., Da, X., & Davatzikos, C. (2014). Comparative evaluation of registration algorithms in different brain databases with varying difficulty: results and insights. *IEEE transactions on medical imaging*, *33*(10), 2039-2065.

Parisot, S., Ktena, S. I., Ferrante, E., Lee, M., Guerrero, R., Glocker, B., & Rueckert, D. (2018). Disease prediction using graph convolutional networks: application to autism spectrum disorder and Alzheimer's disease. *Medical image analysis*, *48*, 117-130.

Park, H.-J., & Friston, K. (2013). Structural and functional brain networks: from connections to cognition. *Science*, *342*(6158), 1238411.

Parker, N. R., Khong, P., Parkinson, J. F., Howell, V. M., & Wheeler, H. R. (2015). Molecular heterogeneity in glioblastoma: potential clinical implications. *Frontiers in oncology*, *5*, 55.

Peng, H., Huo, J., Li, B., Cui, Y., Zhang, H., Zhang, L., & Ma, L. (2021). Predicting isocitrate dehydrogenase (IDH) mutation status in gliomas using multiparameter MRI radiomics features. *Journal of Magnetic Resonance Imaging*, *53*(5), 1399-1407.

Pernet, C. R., Gorgolewski, K. J., Job, D., Rodriguez, D., Whittle, I., & Wardlaw, J. (2016). A structural and functional magnetic resonance imaging dataset of brain tumour patients. *Scientific data*, *3*(1), 1-6.

Prasanna, P., Mitra, J., Beig, N., Nayate, A., Patel, J., Ghose, S., Thawani, R., Partovi, S., Madabhushi, A., & Tiwari, P. (2019). Mass effect deformation heterogeneity (MEDH) on gadolinium-contrast T1-weighted MRI is associated with decreased survival in patients with right cerebral hemisphere glioblastoma: a feasibility study. *Scientific reports*, *9*(1), 1-13.

Price, S., Burnet, N., Donovan, T., Green, H., Pena, A., Antoun, N., Pickard, J., Carpenter, T., & Gillard, J. (2003). Diffusion tensor Imaging of brain tumours at 3 T: A potential tool for assessing white

matter tract invasion? *Clinical Radiology*, *58*(6), 455-462. https://doi.org/10.1016/S0009-9260(03)00115-6

Price, S. J., Allinson, K., Liu, H., Boonzaier, N. R., Yan, J.-L., Lupson, V. C., & Larkin, T. J. (2017). Less Invasive Phenotype Found in Isocitrate Dehydrogenase–mutated Glioblastomas than in Isocitrate Dehydrogenase Wild-Type Glioblastomas: A Diffusion-Tensor Imaging Study. *Radiology*, *283*(1), 215-221. https://doi.org/10.1148/radiol.2016152679

Price, S. J., Pena, A., Burnet, N. G., Jena, R., Green, H. A., Carpenter, T. A., Pickard, J. D., & Gillard, J. H. (2004). Tissue signature characterisation of diffusion tensor abnormalities in cerebral gliomas. *Eur Radiol*, *14*(10), 1909-1917. https://doi.org/10.1007/s00330-004-2381-6

Qi, C. R., Yi, L., Su, H., & Guibas, L. J. (2017). Pointnet++: Deep hierarchical feature learning on point sets in a metric space. *Advances in neural information processing systems*, *30*.

Raj, A., LoCastro, E., Kuceyeski, A., Tosun, D., Relkin, N., Weiner, M., & Initiative, A. s. D. N. (2015). Network diffusion model of progression predicts longitudinal patterns of atrophy and metabolism in Alzheimer's disease. *Cell reports*, *10*(3), 359-369.

Ricard, D., Idbaih, A., Ducray, F., Lahutte, M., Hoang-Xuan, K., & Delattre, J.-Y. (2012). Primary brain tumours in adults. *The Lancet*, *379*(9830), 1984-1996.

Roberts, J. A., Perry, A., Roberts, G., Mitchell, P. B., & Breakspear, M. (2017). Consistency-based thresholding of the human connectome. *Neuroimage*, *145*, 118-129.

Rossi, M., Sciortino, T., Riva, M., Gay, L., Pessina, F., & Bello, L. (2018). Preoperative surgical planning of glioma: limitations and reliability of fMRI and DTI tractography. *Journal of Neurosurgical Sciences*, *63*(2), 127-134.

Rubinov, M., & Sporns, O. (2010). Complex network measures of brain connectivity: uses and interpretations. *Neuroimage*, *52*(3), 1059-1069.

Ruder, S. (2016). An overview of gradient descent optimization algorithms. *arXiv preprint arXiv:1609.04747*.

Salvalaggio, A., De Filippo De Grazia, M., Zorzi, M., Thiebaut de Schotten, M., & Corbetta, M. (2020). Post-stroke deficit prediction from lesion and indirect structural and functional disconnection. *Brain*, *143*(7), 2173-2188. https://doi.org/10.1093/brain/awaa156

Schmainda, K. M. (2012). Diffusion-weighted MRI as a biomarker for treatment response in glioma. *CNS oncology*, *1*(2), 169-180.

Schult, T., Hauser, T.-K., Klose, U., Hurth, H., & Ehricke, H.-H. (2019). Fiber visualization for preoperative glioma assessment: Tractography versus local connectivity mapping. *PloS one*, *14*(12), e0226153.

Schwarz, C. G., Reid, R. I., Gunter, J. L., Senjem, M. L., Przybelski, S. A., Zuk, S. M., Whitwell, J. L., Vemuri, P., Josephs, K. A., & Kantarci, K. (2014). Improved DTI registration allows voxel-based analysis that outperforms tract-based spatial statistics. *Neuroimage*, *94*, 65-78.

Selvaraju, R. R., Das, A., Vedantam, R., Cogswell, M., Parikh, D., & Batra, D. (2016). Grad-CAM: Why did you say that? *arXiv preprint arXiv:1611.07450*.

Shen, D., Wu, G., & Suk, H.-I. (2017). Deep Learning in Medical Image Analysis. *Annual Review of Biomedical Engineering*, *19*(1), 221-248. https://doi.org/10.1146/annurev-bioeng-071516-044442

Shu, N., Liu, Y., Li, K., Duan, Y., Wang, J., Yu, C., Dong, H., Ye, J., & He, Y. (2011). Diffusion Tensor Tractography Reveals Disrupted Topological Efficiency in White Matter Structural Networks in Multiple Sclerosis. *Cerebral Cortex*, *21*(11), 2565-2577. https://doi.org/10.1093/cercor/bhr039

Sinha, R., Dijkshoorn, A. B., Li, C., Manly, T., & Price, S. J. (2020). Glioblastoma surgery related emotion

recognition deficits are associated with right cerebral hemisphere tract changes. *Brain communications*, *2*(2), fcaa169.

Smith, S. M. (2002). Fast robust automated brain extraction. *Human Brain Mapping*, *17*(3), 143-155. https://doi.org/https://doi.org/10.1002/hbm.10062

Smith, S. M., & Brady, J. M. (1997). SUSAN—A New Approach to Low Level Image Processing. *International Journal of Computer Vision*, *23*(1), 45-78. https://doi.org/10.1023/A:1007963824710

Smith, S. M., Jenkinson, M., Johansen-Berg, H., Rueckert, D., Nichols, T. E., Mackay, C. E., Watkins, K. E., Ciccarelli, O., Cader, M. Z., & Matthews, P. M. (2006). Tract-based spatial statistics: voxelwise analysis of multi-subject diffusion data. *Neuroimage*, *31*(4), 1487-1505.

SongTao, Q., Lei, Y., Si, G., YanQing, D., HuiXia, H., XueLin, Z., LanXiao, W., & Fei, Y. (2012). IDH mutations predict longer survival and response to temozolomide in secondary glioblastoma. *Cancer science*, *103*(2), 269-273.

Sporns, O., & Betzel, R. F. (2016). Modular brain networks. *Annual review of psychology*, *67*, 613.

Sporns, O., Tononi, G., & Kötter, R. (2005). The human connectome: a structural description of the human brain. *PLoS Comput Biol*, *1*(4), e42.

Sporns, O., & Zwi, J. D. (2004). The small world of the cerebral cortex. *Neuroinformatics*, *2*(2), 145-162.

Squarcina, L., Bertoldo, A., Ham, T. E., Heckemann, R., & Sharp, D. J. (2012). A robust method for investigating thalamic white matter tracts after traumatic brain injury. *Neuroimage*, *63*(2), 779-788.

Stoecklein, V. M., Stoecklein, S., Galiè, F., Ren, J., Schmutzer, M., Unterrainer, M., Albert, N. L., Kreth, F.-W., Thon, N., Liebig, T., Ertl-Wagner, B., Tonn, J.-C., & Liu, H. (2020). Resting-state fMRI detects alterations in whole brain connectivity related to tumor biology in glioma patients. *Neuro-Oncology*, *22*(9), 1388-1398. https://doi.org/10.1093/neuonc/noaa044

Sun, Y., Chen, Y., Collinson, S. L., Bezerianos, A., & Sim, K. (2015). Reduced Hemispheric Asymmetry of Brain Anatomical Networks Is Linked to Schizophrenia: A Connectome Study. *Cerebral Cortex*, *27*(1), 602-615. https://doi.org/10.1093/cercor/bhv255

Tournier, J.-D., Smith, R., Raffelt, D., Tabbara, R., Dhollander, T., Pietsch, M., Christiaens, D., Jeurissen, B., Yeh, C.-H., & Connelly, A. (2019). MRtrix3: A fast, flexible and open software framework for medical image processing and visualisation. *Neuroimage*, *202*, 116137.

Tournier, J. D., Calamante, F., & Connelly, A. (2012). MRtrix: diffusion tractography in crossing fiber regions. *International journal of imaging systems and technology*, *22*(1), 53-66.

Trudeau, R. J. (2013). *Introduction to graph theory*. Courier Corporation.

Turcan, S., Rohle, D., Goenka, A., Walsh, L. A., Fang, F., Yilmaz, E., Campos, C., Fabius, A. W., Lu, C., & Ward, P. S. (2012). IDH1 mutation is sufficient to establish the glioma hypermethylator phenotype. *Nature*, *483*(7390), 479-483.

Tzourio-Mazoyer, N., Landeau, B., Papathanassiou, D., Crivello, F., Etard, O., Delcroix, N., Mazoyer, B., & Joliot, M. (2002). Automated anatomical labeling of activations in SPM using a macroscopic anatomical parcellation of the MNI MRI single-subject brain. *Neuroimage*, *15*(1), 273-289.

van Dijken, B. R. J., Yan, J. L., Boonzaier, N. R., Li, C., van Laar, P. J., van der Hoorn, A., & Price, S. J. (2017). Subventricular Zone Involvement Characterized by Diffusion Tensor Imaging in Glioblastoma. *World Neurosurg*, *105*, 697-701. https://doi.org/10.1016/j.wneu.2017.06.075

Veličković, P., Cucurull, G., Casanova, A., Romero, A., Lio, P., & Bengio, Y. (2017). Graph attention networks. *arXiv preprint arXiv:1710.10903*.

Venkataramani, V., Tanev, D. I., Strahle, C., Studier-Fischer, A., Fankhauser, L., Kessler, T., Korber, C., Kardorff, M., Ratliff, M., Xie, R., Horstmann, H., Messer, M., Paik, S. P., Knabbe, J., Sahm, F., Kurz, F. T., Acikgoz, A. A., Herrmannsdorfer, F., Agarwal, A., . . . Kuner, T. (2019). Glutamatergic synaptic input to glioma cells drives brain tumour progression. *Nature*, *573*(7775), 532-538. https://doi.org/10.1038/s41586-019-1564-x

Vorona, G. A., & Berman, J. I. (2015). Review of diffusion tensor imaging and its application in children. *Pediatric radiology*, *45*(3), 375-381.

Wang, J., Wang, X., Xia, M., Liao, X., Evans, A., & He, Y. (2015). GRETNA: a graph theoretical network analysis toolbox for imaging connectomics. *Frontiers in human neuroscience*, *9*, 386.

Wang, J., Xu, S.-L., Duan, J.-J., Yi, L., Guo, Y.-F., Shi, Y., Li, L., Yang, Z.-Y., Liao, X.-M., & Cai, J. (2019). Invasion of white matter tracts by glioma stem cells is regulated by a NOTCH1–SOX2 positive-feedback loop. *Nature neuroscience*, *22*(1), 91-105.

Wang, J., Yi, L., Kang, Q.-m., Zhou, J., Chen, T.-q., Hugnot, J.-p., & Yu, S.-c. (2022). Glioma invasion along white matter tracts: A dilemma for neurosurgeons. *Cancer Letters*, *526*, 103-111.

Wang, R., Benner, T., Sorensen, A. G., & Wedeen, V. J. (2007). Diffusion toolkit: a software package for diffusion imaging data processing and tractography. Proc Intl Soc Mag Reson Med,

Warrington, S., Bryant, K. L., Khrapitchev, A. A., Sallet, J., Charquero-Ballester, M., Douaud, G., Jbabdi, S., Mars, R. B., & Sotiropoulos, S. N. (2020). XTRACT-Standardised protocols for automated tractography in the human and macaque brain. *Neuroimage*, 116923.

Watts, D. J., & Strogatz, S. H. (1998). Collective dynamics of 'small-world'networks. *Nature*, *393*(6684), 440-442.

Wei, Y., Li, C., & Price, S. J. (2021). Quantifying structural connectivity in brain tumor patients. International Conference on Medical Image Computing and Computer-Assisted Intervention,

West, D. B. (2001). *Introduction to graph theory* (Vol. 2). Prentice hall Upper Saddle River.

Xiong, Z., Yang, Q., & Li, X. (2020). Effect of intra-and inter-tumoral heterogeneity on molecular characteristics of primary IDH-wild type glioblastoma revealed by single-cell analysis. *CNS neuroscience & therapeutics*, *26*(9), 981-989.

Xu, H., Ding, S., Hu, X., Yang, K., Xiao, C., Zou, Y., Chen, Y., Tao, L., Liu, H., & Qian, Z. (2013). Reduced efficiency of functional brain network underlying intellectual decline in patients with low-grade glioma. *Neuroscience Letters*, *543*, 27-31.

Yen, K., Bittinger, M., Su, S., & Fantin, V. (2010). Cancer-associated IDH mutations: biomarker and therapeutic opportunities. *Oncogene*, *29*(49), 6409-6417.

Yendiki, A., Koldewyn, K., Kakunoori, S., Kanwisher, N., & Fischl, B. (2014). Spurious group differences due to head motion in a diffusion MRI study. *Neuroimage*, *88*, 79-90.

Yeo, B. T., Krienen, F. M., Sepulcre, J., Sabuncu, M. R., Lashkari, D., Hollinshead, M., Roffman, J. L., Smoller, J. W., Zöllei, L., & Polimeni, J. R. (2011). The organization of the human cerebral cortex estimated by intrinsic functional connectivity. *Journal of neurophysiology*.

Ying, Z., Bourgeois, D., You, J., Zitnik, M., & Leskovec, J. (2019). Gnnexplainer: Generating explanations for graph neural networks. *Advances in neural information processing systems*, *32*.

Yu, K., Lin, C. J., Hatcher, A., Lozzi, B., Kong, K., Huang-Hobbs, E., Cheng, Y. T., Beechar, V. B., Zhu, W., Zhang, Y., Chen, F., Mills, G. B., Mohila, C. A., Creighton, C. J., Noebels, J. L., Scott, K. L., & Deneen, B. (2020). PIK3CA variants selectively initiate brain hyperactivity during gliomagenesis. *Nature*, *578*(7793), 166-171. https://doi.org/10.1038/s41586-020-1952-2

Yu, Z., Tao, L., Qian, Z., Wu, J., Liu, H., Yu, Y., Song, J., Wang, S., & Sun, J. (2016). Altered brain anatomical

networks and disturbed connection density in brain tumor patients revealed by diffusion tensor tractography. *International journal of computer assisted radiology and surgery*, *11*(11), 2007-2019.

Zalesky, A., Fornito, A., & Bullmore, E. T. (2010). Network-based statistic: identifying differences in brain networks. *Neuroimage*, *53*(4), 1197-1207.

Zhang, F., Noh, T., Juvekar, P., Frisken, S. F., Rigolo, L., Norton, I., Kapur, T., Pujol, S., Wells III, W., & Yarmarkovich, A. (2020). SlicerDMRI: Diffusion MRI and tractography research software for brain cancer surgery planning and visualization. *JCO clinical cancer informatics*, *4*, 299-309.

Zhang, Y., Jiang, H., Miura, Y., Manning, C. D., & Langlotz, C. P. (2020). Contrastive learning of medical visual representations from paired images and text. *arXiv preprint arXiv:2010.00747*.